Observation of a Small ν_μ/ν_e Ratio of Atmospheric Neutrinos in Super-Kamiokande by the Method of Particle Identification

Syunsuke Kasuga

January 1998

Doctor Thesis, University of Tokyo

Acknowledgements

I would like to express my sincere appreciation to my advisor, Prof.Y.Totsuka, for introducing me this experiment and encouraging me throughout this work.

I gratefully acknowledge the helpful advice of Prof.T.Kajita, M.Shiozawa, Dr.Y.Itow and Dr.M.Miura. They are experts in the atmospheric neutrino analysis. Their suggestions and advices were very useful for me.

I owe thanks to my fellow graduate students Y.Hayato, K.Ishihara, K.Okumura, H.Ishino, M.Eto, J.Kameda and Y.Kanaya. They gave me useful discussions and assisted with my analysis. Without their supports, I could not accomplish my thesis.

I would like to thank Y.Kitaguchi, K.Fujita, F.Tsushima, E.Ichihara, N.Sakurai and M.Ota. They gave me useful discussions about experimental details.

I with to express my deeply appreciation to T.Hayakawa and Y.Koshio. They live in Kamioka and supported me on various occasions.

I would like to thank Prof.Y.Suzuki, Prof.M.Nakahata, Dr.Y.Fukuda, Dr.K.Inoue, Dr.Y.Takeuchi and Dr.K.Kaneyuki for their advice.

I must thank all the other Super-Kamiokande collaborators for their work, help and warm hospitality. Especially, Dr.M.Takita, Dr.S.Hatakeyama, Dr.M.Koga, T.Yamaguchi, H.Okazawa and M.Nemoto gave me many advices.

I must also thank the staff of the KEK. I learned a lot about the experimental technique there. Prof.K.Nishikawa and Dr.A.Sakai gave me many useful suggestions and discussions. I would like to express my appreciation to Dr.Y.Oyama for his advice and support. His excellent guidance and suggestions were very useful for me.

I would like to thank C.Mauger for reading and fixing this manuscript. I thank the cooperation of Kamioka Mining and Smelting Company and financial support of the Japan Society for the Promotion of Science.

Contents

List of Figures

List of Tables

Chapter 1

Introduction

1.1 Atmospheric neutrinos

Atmospheric neutrinos are the decay products of mesons (π's, K's, and muons) created in interactions of primary cosmic rays (protons and nuclei) high in the atmosphere. Fig. 1.1 shows the predicted flux of atmospheric neutrinos. As shown in this figure,

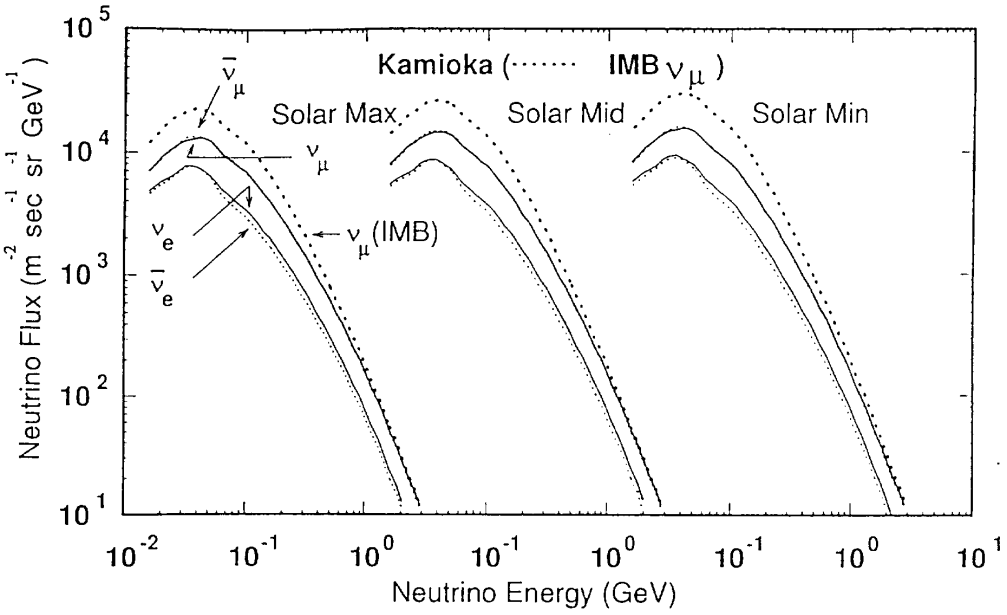

Figure 1.1: Calculated atmospheric neutrino fluxes at Kamioka for solar modulation of max, mid and min by Honda[1]. The estimated $\nu_\mu(\bar{\nu}_\mu)$, $\nu_{\rm e}(\bar{\nu}_e)$ flux at Kamioka site are shown by solid (ν_μ, $\nu_{\rm e}$) and dashed ($\bar{\nu}_\mu$, $\bar{\nu}_e$) lines. The dotted line is for $\nu_\mu$flux at IMB site.

the atmospheric neutrino flux depends on the experimental site and solar modulation, because the geomagnetic latitude and 11-year-period solar activity affect the flux of primary cosmic rays.

When the primary cosmic rays propagate in the atmosphere, they create pions and kaons by interactions with air nuclei. Relevant decay modes of these mesons are shown in Table 1.1. In these decay modes, the following decay chain is dominant.

$\pi^{\pm}$	$\rightarrow$	$\mu^{\pm}\nu_{\mu}(\overline{\nu_{\mu}})$	(100%)
$\mu^{\pm}$	$\rightarrow$	$e^{\pm}\nu_{e}(\overline{\nu_{e}})\nu_{\mu}(\overline{\nu_{\mu}})$	(100%)
$K^{\pm}$	$\rightarrow$	$\mu^{\pm}\nu_{\mu}(\overline{\nu_{\mu}})$	(63.5%)
	$\rightarrow$	$\pi^{\pm}\pi^{0}$	(21.2%)
	$\rightarrow$	$\pi^{\pm}\pi^{+}\pi^{-}$	(5.6%)
	$\rightarrow$	$\pi^{0}\mu^{\pm}\nu_{\mu}(\overline{\nu_{\mu}})$	(3.2%)
	$\rightarrow$	$\pi^{0}e^{\pm}\nu_{e}(\overline{\nu_{e}})$	(4.8%)
	$\rightarrow$	$\pi^{\pm}\pi^{0}\pi^{0}$	(1.73%)
K_{S}^{0}	$\rightarrow$	$\pi^{+}\pi^{-}$	(68.6%)
K_{L}^{0}	$\rightarrow$	$\pi^{+}\pi^{-}\pi^{0}$	(12.37%)
	$\rightarrow$	$\pi^{\pm}\mu^{\mp}\nu_{\mu}(\overline{\nu_{\mu}})$	(27%)
	$\rightarrow$	$\pi^{\pm}e^{\mp}\nu_{e}(\overline{\nu_{e}})$.	(38.6%)

Table 1.1: decay mode

$$\pi^{\pm} \rightarrow \mu^{\pm} + \nu_{\mu}(\overline{\nu_{\mu}})$$
$$\downarrow$$
$$\mu^{\pm} \rightarrow e^{\pm} + \nu_{e}(\overline{\nu_{e}}) + \nu_{\mu}(\overline{\nu_{\mu}}).$$

The uncertainty in the calculation of atmospheric neutrino flux is mainly due to the uncertainties in the flux of the primary cosmic rays and hadronic interactions and is estimated to be $\sim$20%.

In the low energy range ($E_{\nu} < 1GeV$), even muons (mean lifetime = 2.2μsec) decay in the atmosphere, thus one expects the ratio of the number of ν_{μ}'s to ν_{e}'s to be approximately 2:1. At E_{ν}=1GeV, the ν_{μ}/ν_{e} ratio is estimated to be 2.1 by several independent calculations. But at higher energies, muons tend to survive and hit the earth before they decay. This reduces the flux of ν_{e} and raises the ν_{μ}/ν_{e} ratio. The uncertainty in the ν_{μ}/ν_{e} ratio is estimated to be only $\sim$5%, because the uncertainty in

the absolute flux is cancelled out by taking the ratio.

1.2 Atmospheric neutrino anomaly

In the 1980's, massive underground experiments, which could detect atmospheric neutrinos, started at several experimental sites. Originally, these experiments aimed at detecting nucleon decay. Atmospheric neutrinos were only studied to estimate the backgrounds for nucleon decay searches.

In 1988, however, Kamiokande observed an anomalous atmospheric neutrino flavor ratio through a detailed study of these atmospheric neutrinos. Kamiokande measured the number of single-ring electron-like (e-like) and muon-like (μ-like) events, and took the ratio of these two numbers, μ-like / e-like. Since the μ-like (e-like) events are dominated by charged current ν_μ (ν_e) interactions, the ratio μ-like / e-like, approximates the atmospheric $(\nu_\mu+\bar{\nu}_\mu)/(\nu_\mathrm{e}+\bar{\nu}_e)$ flux ratio. The measured μ-like / e-like ($\equiv \mu/\mathrm{e}$) ratio was found to be only 60% of the expected value.

We usually use the $(\nu_\mu + \bar{\nu_\mu})/(\nu_e + \bar{\nu}_e)$ ratio to show the atmospheric neutrino results because the ratio of muon to electron neutrinos has a much smaller uncertainty ($\sim 5\%$) than the uncertainty of the absolute atmospheric neutrino flux ($\sim$ 20%). A ratio of ratios, R, is defined as:

$$R = \frac{(\mu/e)_{Measured}}{(\mu/e)_{Expected}}$$

Results of atmospheric neutrino measurements are shown in Fig. 1.2. The R value smaller than 1, reported in Kamiokande, is confirmed by IMB and Soudan 2 experiments. Results of Fréjus and NUSEX experiments are consistent with Monte Carlo predictions, but they have larger statistical uncertainty.

In the following sections, I will describe the details of these experiments.

1.2.1 Kamiokande

Kamiokande was an imaging water Cherenkov detector located 1000m underground in the Kamioka mine. 3000tons of pure water was stored in a cylindrical steel tank. The water was viewed by 948 20-inch photomultiplier tubes (PMT), covering 20% of the tank inner surface. In Kamiokande-II and also Kamiokande-III, the inner detector was surrounded by a 4π anticounter layer which contained 1.2-2.0m thick water and viewed by 123 20-inch PMTs. The operation of Kamiokande started in July 1983 to search for nucleon decay. Kamiokande-II tried to detect low energy, astrophysical neutrinos such

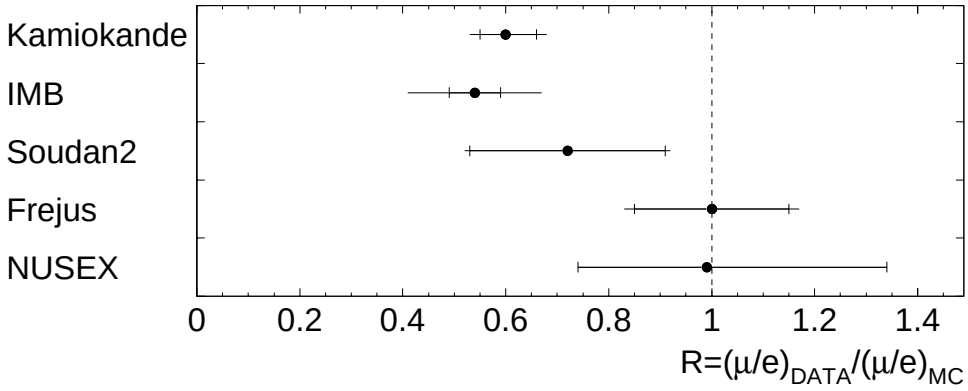

Figure 1.2: Present atmospheric neutrino experimental status. Inner error bars show statistical error and outer error bars show $\sqrt{(syst.)^2 + (stat.)^2}$.

as solar neutrinos[2]. Successful observation of the neutrino burst from the supernova SN1987A[3] was especially well known.

In Kamiokande, atmospheric neutrinos were detected by their interactions in water. The relevant interaction processes were:

- Charged-current quasi-elastic reaction $\nu_l N \to l N'$
- Charged-current single-pion production $\nu_l N \to l N' + \pi$
- Charged-current multiple-pion production $\nu_l N \to l N' + m\pi$
- Neutral-current quasi-elastic reaction $\nu_l N \to \nu_l N'$
- Neutral-current single-pion production $\nu_l N \to \nu_l N' + \pi$
- Neutral-current multiple-pion production $\nu_l N \to \nu_l N' + m\pi$

Here l means e or μ and N means nucleon. Kamiokande observed electrons and muons produced by these reactions.

Table 1.2 is the result on the sub-GeV [1] atmospheric neutrinos observed in Kamiokande which are compared with the Monte Carlo prediction [2]. Though the number of single ring e-like events is in good agreement with the expected number, a deficit of μ-like events relative to the Monte Carlo prediction is apparent.

[1] $0.1 < p_e < 1.33$GeV/c for the e-like events and $0.2 < p_\mu < 1.5$GeV/c for the μ-like events.

[2] Monte Carlo prediction is based on 43 kton-years equivalent simulated data which passed through the same analysis chain.

	Data	Monte Carlo
single ring	482	584.3
μ-like	234	356.8
e-like	248	227.6
multi ring	208	233.8
total ev.	690	818.1
$\frac{(\mu/e)_{data}}{(\mu/e)_{M.C.}}$		$0.60^{+0.06}_{-0.05}$

Table 1.2: Summary of the sub-GeV atmospheric neutrino data from Kamiokande-I,II,III. The detector exposure is 7.7 kton-years.

The observed $(\mu/\mathrm{e})_{data}$ / $(\mu/\mathrm{e})_{MC}$ was,

$$R = 0.60 \pm^{0.06}_{0.05} (stat.) \pm 0.05(syst.).$$

To verify the Kamiokande result, we constructed a 1000 ton water Cherenkov detector and injected electrons and muons produced by a 12GeV proton synchrotron at KEK in Japan[4]. By this beam test, we determined the vertex resolution, energy resolution, and especially the performance of the particle identification algorithms. The misidentification probabilities for e-like and μ-like events were estimated to be less than $\sim$3% in the momentum range of 250-1000MeV/c except for particles injected at 1.8m from the detector wall, which is outside of the fiducial volume. Thus, we confirmed that the atmospheric neutrino anomaly was not caused by an experimental flaw.

1.2.2 IMB-3

The IMB-3 (Irvine-Michigan-Brookhaven) detector was located in the Morton Salt Mine near Cleveland, Ohio, USA. The detector was an 8 kton water Cherenkov detector which had 2048 8-inch PMTs with wavelength-shifter plates. The wavelength shifter plate was installed to increase the light collection efficiency. The fiducial volume was 3.3 kton and was 2m inside of the PMT surfaces.

Data were taken from May 1986 to March 1991 and the total exposure was 7.7 kton-years. Single-ring contained events were used for atmospheric neutrino analysis. The data with momentum, p <1500MeV/c and visible energy, E_{vis} > 100MeV consisted of 325 e-like events and 182 μ-like events[5]. From Monte Carlo studies, the particle identification capability was estimated to be 92% and 87% for ν_μ-induced and ν_e-induced

events, respectively. In 1992, R was reported as:

$$R = 0.54 \pm 0.05(stat.) \pm 0.12(syst.).$$

1.2.3 Soudan 2

The Soudan 2 experiment was located in an iron mine in northern Minnesota, USA. The main detector was an iron tracking calorimeter with a total mass of 963 tons, divided into 224 modules. Each module consisted of 7560 drift tubes in a hexagonal honeycomb structure. The calorimeter was surrounded by a 1700 m^2 active shield of aluminum proportional tubes to reject background.

The analysis of atmospheric neutrinos was reported in 1997[6] with data from April 1989 to December 1993. The total exposure was 1.52 kton-years. Contained events with energy more than 200MeV were used for the atmospheric neutrino analysis. A contained event was defined as an event in which no primary particle in the event left the fiducial volume of the detector. The fiducial volume was defined by a 20 cm depth cut on all sides of the detector. The lepton flavor of each event was determined by scanners. Using Monte Carlo simulation to study misidentification capabilities, 87% of events assigned as tracks (μ-like) had muon flavor while 96% of events assigned as showers (e-like) had electron flavor.

They detected 47 track events and 60 shower events, so the R measured in the Soudan 2 experiment was:

$$R = 0.72 \pm 0.19(stat.)^{+0.05}_{-0.07}(syst.).$$

Soudan 2 is still running and the exposure will reach to 5 kton-years in 1999.

1.2.4 Fréjus

The Fréjus experiment was located in the middle of the Fréjus highway tunnel connecting France and Italy. The detector was 912 ton iron calorimeter and measured 6m×6m×12.3m. It consisted of 912 flash chamber planes and 113 Geiger tube planes which provided the trigger. A flash chamber plane was made of a sandwich structure with 3mm thick iron plates and 5mm thick planes of plastic flash tubes.

Data were taken from February 1984 to September 1988. The fiducial volume was defined such that the interaction vertex had to be located more than 50cm away from the detector surface. Since this cut reduced the fiducial mass to 554 tons, the total exposure was 1.56 kton-years[7].

Events were classified as contained or non-contained. Non-contained events with one track were rejected as cosmic-ray muons. They found 142 contained events and 46 non-contained events. These events were also classified as charged current $\nu_\mu(\mathrm{CC}\mu)$, charged current $\nu_e(\mathrm{CC}e)$, or neutral current(NC) interactions by visual inspection. The identification efficiency for CCμ and CCe interactions were investigated by simulated events and the efficiency was estimated to be 95% and 85% for muon and electron neutrino events respectively.

The R from the Fréjus analysis of contained and non-contained events, reported in 1989, is

$$R = 1.06^{+0.19}_{-0.16}(stat.) \pm 0.15(syst.).$$

In 1995, the data was reanalyzed with an enlarged fiducial volume (700 ton). The new R is,

$$R = 1.00 \pm 0.15(stat.) \pm 0.08(syst.).$$

1.2.5 NUSEX

The NUSEX detector was a 150 ton, 3.5m cubical iron tracking calorimeter located in the Mont Blanc tunnel. The tracking calorimeter was made by 134 horizontal iron plates of 1 cm thickness, interleaved with plastic streamer tubes.

Events with the lepton energy above 200MeV were used in the analysis. The performance of particle type identification was tested directly by an accelerator and was found to be good. Data were taken from June 1982 to June 1988, corresponding to 0.74 kton-years of total mass exposure. During run time, 32 μ-like and 18 e-like events were detected. The R, reported in 1989[8], is

$$R = 0.96^{+0.32}_{-0.28}(stat.)$$

1.3 Possible explanations for the atmospheric neutrino anomaly

In the previous section I presented the status of atmospheric neutrino experiments. The discrepancy of the $(\nu_\mu + \bar{\nu_\mu})/(\nu_e + \bar{\nu_e})$ ratio between the calculations and the results cannot be explained within the framework of the standard model of particle physics if the anomaly is not caused by the experimental reasons.

In this section, I will describe three possible explanations of the atmospheric neutrino anomaly.

1.3.1 Neutron background

It was suggested that the small $(\nu_\mu + \bar{\nu_\mu})/(\nu_e + \bar{\nu_e})$ ratio could be explained by isolated neutron interactions in the detector. Neutrons are generated in deep-inelastic scattering of cosmic-ray muons in the rock around the detector and some of these neutrons go into the detector and produce π^0's. A γ from π^0 decay could be identified as an e-like event if one of the two γ's is not identified.

In Kamiokande, the neutron contribution to the atmospheric neutrino measurement was studied[9]. For the sub-GeV region (E_{vis} <1.33GeV), the vertex-position distribution of 2-ring π^0-like events was examined and there was no excess near the detector wall. Therefore the possible contamination of neutrons in the sub-GeV e-like sample was estimated to be less than 1.2% at the 90% C.L. For the multi-GeV region (E_{vis} >1.33GeV), the background contamination was estimated using the vertex distribution of the e-like events and the possible contamination was estimated to be less than 14% at the 90% C.L.

In summary, it was verified that the neutron background cannot explain the atmospheric neutrino anomaly, especially for the sub-GeV region.

1.3.2 Proton decay

Another explanation proposed to explain the atmospheric neutrino anomaly is proton decay. This model says that the flux anomaly is caused by an excess of e-like events which are produced by the proton decay mode, $p \to e^+\nu\nu$. Since a proton decays into three particles, the energy spectrum for e^+ is broad and its energy is less than ~500MeV. Therefore, if an excess of electrons is found only in the energy region less than 500MeV, it could be explained by proton decay. The possibility of proton decay will be discussed in Sec. 7.3.

1.3.3 Neutrino oscillations

Neutrinos are treated as massless in the standard model. However, there is no compelling reason why neutrinos are massless and why neutrino families should not mix like quarks. If neutrinos are indeed massive, it is very likely that some mixing occurs among them.

Neutrino oscillations are generally predicted to occur for non zero neutrino mass and mixing.

Here, we give a brief explanation of the neutrino oscillations for a simple two neutrino system. The observed neutrinos, ν_e and ν_μ, are flavor eigenstates. They are not necessarily identical to mass eigenstates, ν_1 and ν_2. These two eigenstates are combined by the unitary matrix, U, and described as:

$$\begin{pmatrix} \nu_e \\ \nu_\mu \end{pmatrix} = U \begin{pmatrix} \nu_1 \\ \nu_2 \end{pmatrix} = \begin{pmatrix} \cos\theta & \sin\theta \\ -\sin\theta & \cos\theta \end{pmatrix} \begin{pmatrix} \nu_1 \\ \nu_2 \end{pmatrix} \tag{1.1}$$

where θ is the mixing angle with $0 \leq \theta \leq \frac{\pi}{4}$. Time evolution of mass eigenstates can be written as:

$$\begin{pmatrix} \nu_1(t) \\ \nu_2(t) \end{pmatrix} = \begin{pmatrix} \exp(-iE_1t) & 0 \\ 0 & \exp(-iE_2t) \end{pmatrix} \begin{pmatrix} \nu_1(0) \\ \nu_2(0) \end{pmatrix}, \tag{1.2}$$

where $\nu_1(0)$ and $\nu_2(0)$ are the mass eigenstates at $T = 0$ and and $\nu_1(t)$ and $\nu_2(t)$ are the mass eigenstates at $T = t$.

Eq.1.2 is rewritten using Eq.1.1 as:

$$\begin{pmatrix} \nu_e(t) \\ \nu_\mu(t) \end{pmatrix} = U \begin{pmatrix} \exp(-iE_1t) & 0 \\ 0 & \exp(-iE_2t) \end{pmatrix} U^\dagger \begin{pmatrix} \nu_1(0) \\ \nu_2(0) \end{pmatrix}, \tag{1.3}$$

Then, the probability that a neutrino born as a ν_e at the source remains as a ν_e is given by:

$$\begin{aligned} P(\nu_e \to \nu_e) &= \left| \begin{pmatrix} 1 & 0 \end{pmatrix} U \begin{pmatrix} \exp(-iE_1t) & 0 \\ 0 & \exp(-iE_2t) \end{pmatrix} U^\dagger \begin{pmatrix} 1 \\ 0 \end{pmatrix} \right|^2 \\ &= 1 - \frac{1}{2}\sin^2 2\theta(1 - \cos(E_2 - E_1)t) \end{aligned} \tag{1.4}$$

Finally, the survival probability can be rewritten as:

$$P(\nu_e \to \nu_e) = 1 - \sin^2 2\theta \sin^2\left(\frac{1.27\triangle m^2 L}{p_\nu}\right), \tag{1.5}$$

where $\triangle m^2 = m_2^2 - m_1^2(\mathrm{eV}^2)$, and $L(\mathrm{km})$, $p_\nu(\mathrm{GeV/c})$ are the path length and momentum of the neutrino, respectively.

Atmospheric neutrinos can be used to study neutrino oscillations by interpretting the source of the anomaly as muon neutrino oscillations into either electron or tau neutrinos. Since neutrino oscillations depend on the path length of the neutrinos, L, the zenith angle distribution of R also provides useful information about neutrino oscillations. The

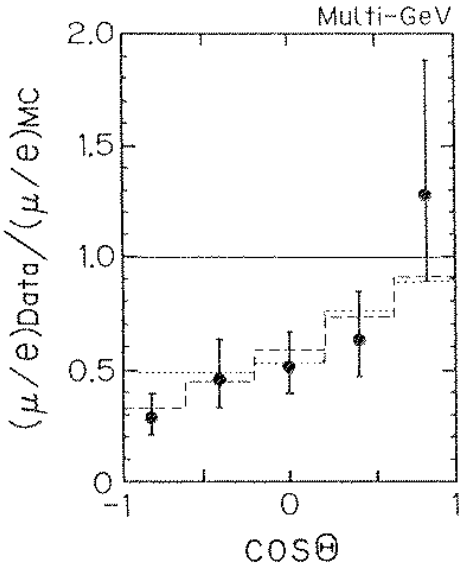

Figure 1.3: Zenith angle distribution of R for the multi-GeV contained events in Kamiokande. The plots with error bars show the data. Histograms show the Monte Carlo prediction with neutrino oscillations. For $\nu_\mu \leftrightarrow \nu_e$ oscillation the best-fit oscillation parameter sets $(\sin^2 2\theta, \triangle m^2(\mathrm{eV}^2))$ is $(1.0,\ 1.8 \times 10^{-2})$ (dashed line) For $\nu_\mu \leftrightarrow \nu_\tau$ oscillation the best-fit parameter sets is $(1.0, 1.6 \times 10^{-2})$ (dotted line).

zenith angle distribution of R for multi-GeV events observed in Kamiokande, as shown in Fig. 1.3, is very suggestive of neutrino oscillations.

Neutrino oscillations searches have been done by many experiments. They have used solar, atmospheric, accelerator or reactor neutrinos. Fig. 1.4 shows the present experimental status of neutrino oscillation experiments. Solar neutrino and reactor experiments are sensitive to $\nu_e \leftrightarrow \nu_X$ oscillations. Solar neutrino experiments indicate three solutions for neutrino oscillations, small angle, large angle, and justso solutions. Typical $(\sin^2 2\theta,\ \triangle m^2(\mathrm{eV}^2))$ of these solutions are $(9.1 \times 10^{-3}, 6.3 \times 10^{-6})$, $(0.7, 2.8 \times 10^{-5})$, and $(0.8, 7.1 \times 10^{-11})$, respectively[10]. Reactor experiments give exclusion regions. Atmospheric neutrino data in Kamiokande indicate neutrino oscillations and the other atmospheric neutrino experiments and accelerator experiments give exclusion regions. Gösgen[11], Bugey[12], and CHOOZ[13] are reactor experiments and CDHSW[14] is an accelerator experiment. Upward-going muons produced by atmospheric neutrinos are also sensitive to the neutrino oscillations and give an exclusion region for $\nu_\mu \leftrightarrow \nu_\tau$ oscillations[15].

1.4 Motivation of this thesis

As mentioned in previous sections, the atmospheric neutrino anomaly was reported by several experiments, and in order to explain the anomaly, several models were suggested.

We constructed 50 kton water Cherenkov detector, Super-Kamiokande, which enables us to carry a high-statistics atmospheric neutrino measurement for the first time.

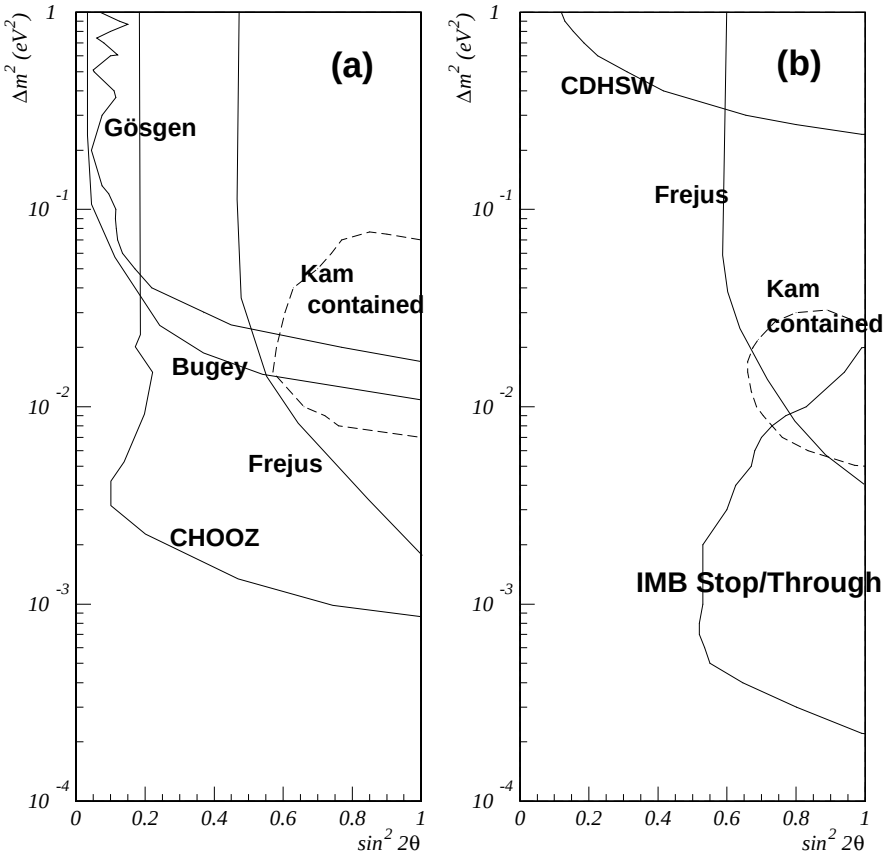

Figure 1.4: Constraints to $\triangle m^2$ and $\sin^2 2\theta$ for (a)$\nu_\mu \leftrightarrow \nu_e$ and (b)$\nu_\mu \leftrightarrow \nu_\tau$ oscillations. The solid lines show excluded region with 90% C.L. and the dashed lines show allowed region with 90% C.L.

The fiducial volume of Super-Kamiokande is more than 20 times as large as that of Kamiokande. In this thesis, the atmospheric neutrino measurement in the sub-GeV energy range in Super-Kamiokande with 20 kton-years exposure is presented and the ν_μ/ν_e ratio and the zenith angle distribution will be discussed.

Chapter 2

Super-Kamiokande detector

The Super-Kamiokande detector is a ring imaging water Cherenkov detector located about 200m south-west of the Kamiokande detector in the Kamioka mine of Gifu Prefecture, Japan. It is reached by a 2km long access tunnel and lies 1000m under the ground. The 1000m thickness of the rock is equivalent to 2700m water and it reduces the cosmic-ray muon rate at the Super-Kamiokande site to 2.2Hz. In the mine, the clean natural water flows and is used as the primary water for the detector. The water temperature is stable at 9-10°C all year long.

In this chapter, the principle of a water Cherenkov detector is explained in Sec. 2.1 and details of the experimental setup are presented in Sec. 2.2-2.5.

2.1 Water Cherenkov detector

A ring-imaging water Cherenkov detector detects Cherenkov photons emitted in water by charged particles. Based on information of the pulse arrival-time and amplitude from each PMT, it is possible to reconstruct the vertex position, direction, momentum and particle type of the parent charged particle.

A charged particle emits Cherenkov photons [1] if the velocity of the charged particle, β, exceeds the speed of light in the medium ;

$$n\beta \geq 1, \tag{2.1}$$

where n is the index of refraction of the medium (n=1.33$\sim$1.36 in water, depending on the wavelength of a photon). They are emitted on a cone with a half opening angle, θ,

[1] This emission was first discovered by Cherenkov in 1934.

with respect to the particle direction:

$$\cos\theta = \frac{1}{n\beta}. \tag{2.2}$$

For $\beta = 1$, $\theta = 42^\circ$ (in water). The number of photons emitted per unit path length per unit frequency is given by

$$\frac{d^2N}{dxd\nu} = \frac{2\pi\alpha}{c}(1 - \frac{1}{n^2\beta^2}), \tag{2.3}$$

where α is the fine structure constant, x is the path length of the charged particle, and ν is the frequency of the emitted photon. The number of Cherenkov photons emitted in the wavelength range of 300-600nm, which is the sensitive region of the PMTs, is about 340 per cm in water. The total number of the Cherenkov photons is proportional to the total energy deposited by a charged particle, because the track length of a charged particle is almost proportional to its energy. Cherenkov photons are detected by photomultiplier tubes (PMT) which surround the inner water mass. If a charged particle stops inside the detector, Cherenkov photons image a characteristic ring pattern on the the detector wall.

Advantages of the ring-imaging water Cherenkov detector are: (1) particle direction is determined, (2) the detector is very simple and can have a large fiducial volume.

2.2 Water tank

Fig. 2.1 shows a view of Super-Kamiokande. The cavity is coated with 40-50cm thick reinforced concrete on the side wall and the floor and the stainless cylindrical water tank is situated inside of the cavity. The tank is 42m in height, 39m in diameter and 50000m^3 in volume. Above the tank, there is a space of a hemispherical shape where four electronics huts and one central hut are arranged.

The average geo-magnetic field at the Super-Kamiokande site is 450mG. PMTs do not work properly in a magnetic field of more than 100mG. To compensate for the geo-magnetic field, 26 sets of Helmholz coils are arranged in the tank. The geo-magnetic field inside the tank is reduced to about 50mG.

The Super-Kamiokande detector has two PMT layers, an inner detector(ID) and an outer detector(OD). The inner detector is completely surrounded by the outer detector. These two layers are optically separated by a pair of opaque sheets as shown in Fig. 2.2. The dead region between two sheets is 55cm in thickness. The details of the inner and outer detectors are described in the following subsections.

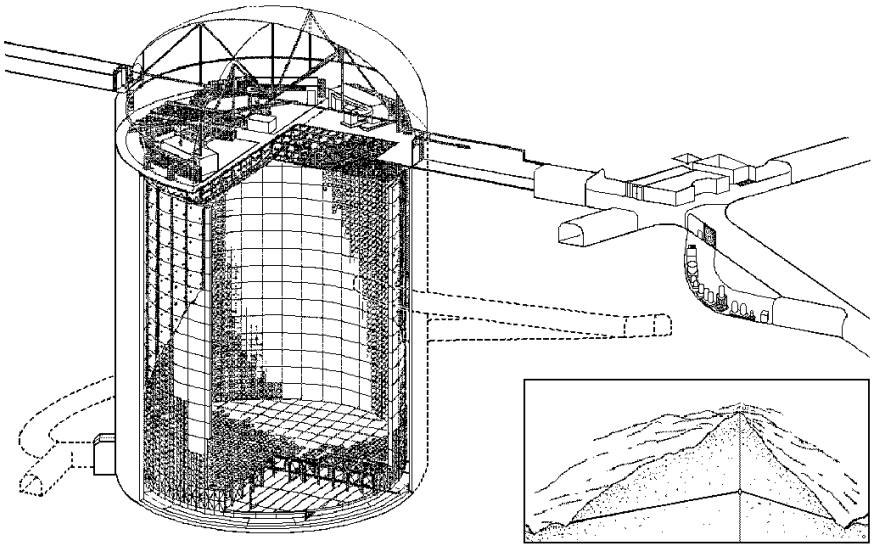

Figure 2.1: A schematic view of the Super-Kamiokande detector.

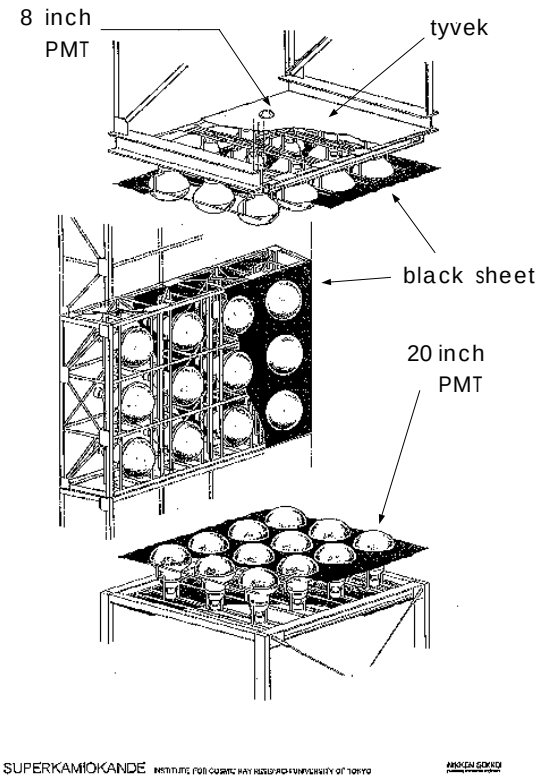

Figure 2.2: The structure of the frame for ID and OD PMTs.

Inner Detector

A water Cherenkov detector should have a large photosensitive area in order to collect as many Cherenkov photons as possible. For this purpose, custom 20-inch PMTs are used for the inner detector. On the inner surface of the inner detector, 11146 20-inch PMTs are placed uniformly and 40% photocathode coverage twice that of Kamiokande is achieved. The size of the inner detector inside the PMT surface is 33.8m in diameter, 36.2m in height and 32000m^3 in volume. The areas between the PMTs are covered with black PET (polyethylene terephthalate) sheets as shown in Fig. 2.2.

Outer detector

The outer detector is used as a veto-counter which identifies background particles from the outside of the detector such as cosmic-ray muons. The outer detector also shields the inner detector from gamma rays and neutrons from the rock. The outer detector surrounds the inner detector completely and the thickness of the outer detector is 2.05m on the side wall and 2.2m on the top and bottom walls. The outer detector is instrumented with 1885 HAMAMATSU R1408 8-inch PMTs. Each 8-inch PMT is attached by a 60cm square acrylic plate containing a wavelength shifter plate to increase the light collection efficiency. The surface of the outer detector is covered with a reflective sheet, called Tyvek, to enhance the light collection.

2.3 20-inch PMT

Originally the 20-inch PMT was developed by HAMAMATSU Photonics Company for the Kamiokande experiment. This PMT has demonstrated excellent performance in the Kamiokande experiment. For Super-Kamiokande, several improvements in the dynodes shape and the bleeder chain enable us to obtain even better timing and energy resolutions. Properties of the PMT are listed in Table 2.1 and a view of 20-inch PMT is shown in Fig. 2.3. A clear single-photoelectron peak can be seen in the pulse height distribution(see Fig. 2.4). In summary, the performance of the 20-inch PMT is good enough to be used in Super-Kamiokande. More details of the 20-inch PMT are presented in [16].

Photo-cathode area	50cm in diameter
Shape	Hemispherical
Window material	Pyrex glass(4∼5mm)
Photo-cathode material	Bialkali
Dinodes	11 stage, Venetian blind
Pressure tolerance	6kg/cm^2 water proof
Quantum efficiency	22% at λ =390nm
Gain	10^7 at ∼2000 Volt
Dark current	200nA at gain=10^7
Dark pulse rate	3kHz at gain=10^7
Cathode non-uniformity	less than 10%
Anode non-uniformity	less than 40%
Transit time	100nsec typical, at gain=10^7
Transit time spread	σ ∼2.5nsec

Table 2.1: The properties of the 20-inch ϕ PMT

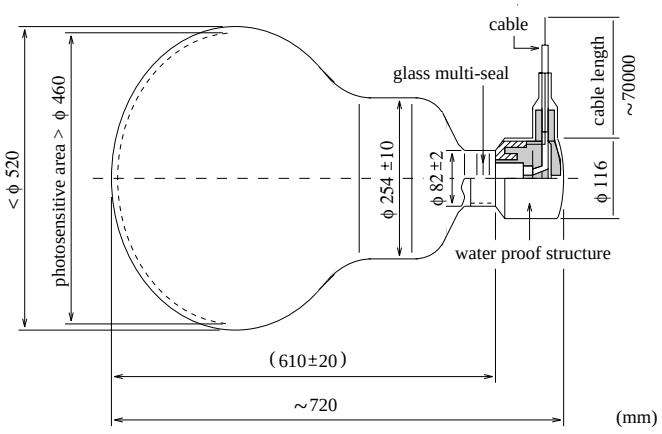

Figure 2.3: A schematic view of PMT.

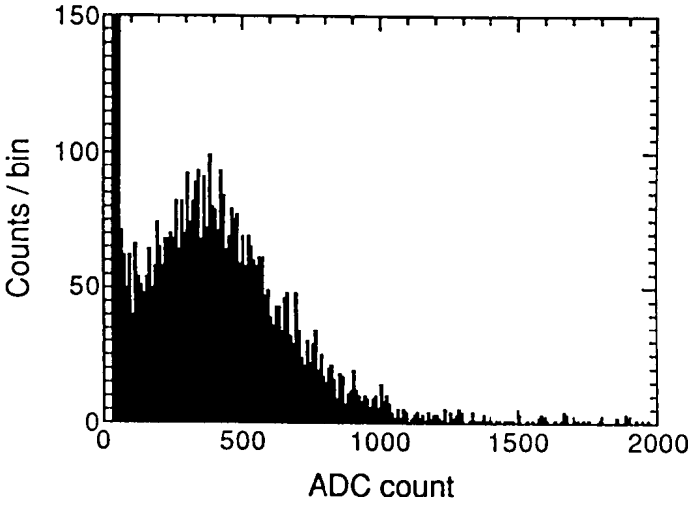

Figure 2.4: A typical 1p.e. distribution.

2.4 Water purification

To receive enough Cherenkov photons, we must keep the light attenuation length in the water a reasonable length and remove radioactive elements in the water to reduce low-energy backgrounds. For these purposes, water in the tank is circulated and purified continuously. The water purification system consists of the following 7 components:

1. 1μm Filter to remove dust.
2. Heat exchanger to cool the water temperature to about 13°C.
3. Ion exchanger to remove ions.
4. UV sterilizer to kill bacteria.
5. Vacuum degasifier to remove remaining gas such as oxygen and radon.
6. Cartridge polisher to remove ions.
7. Ultra filter to remove small particles($\sim$ 10nm).

The flow diagram is shown in Fig. 2.5. This system purifies the detector water with a flow rate of about 50m^3/hour. Ultra filters separate the input water into particle free water and a small amount of (15%) water containing particles which is sent to a buffer tank. Then it is purified by the reverse osmosis and is returned back to the (2)heat exchanger.

After the water purification, the concentration of radon, which is 10^4Bq/m^3 in the mine water, is reduced to $\sim$5mBq/m^3 and the light attenuation length is about 100m at a wavelength of 420nm. (The attenuation length measurement is presented in Sec. 3.4.)

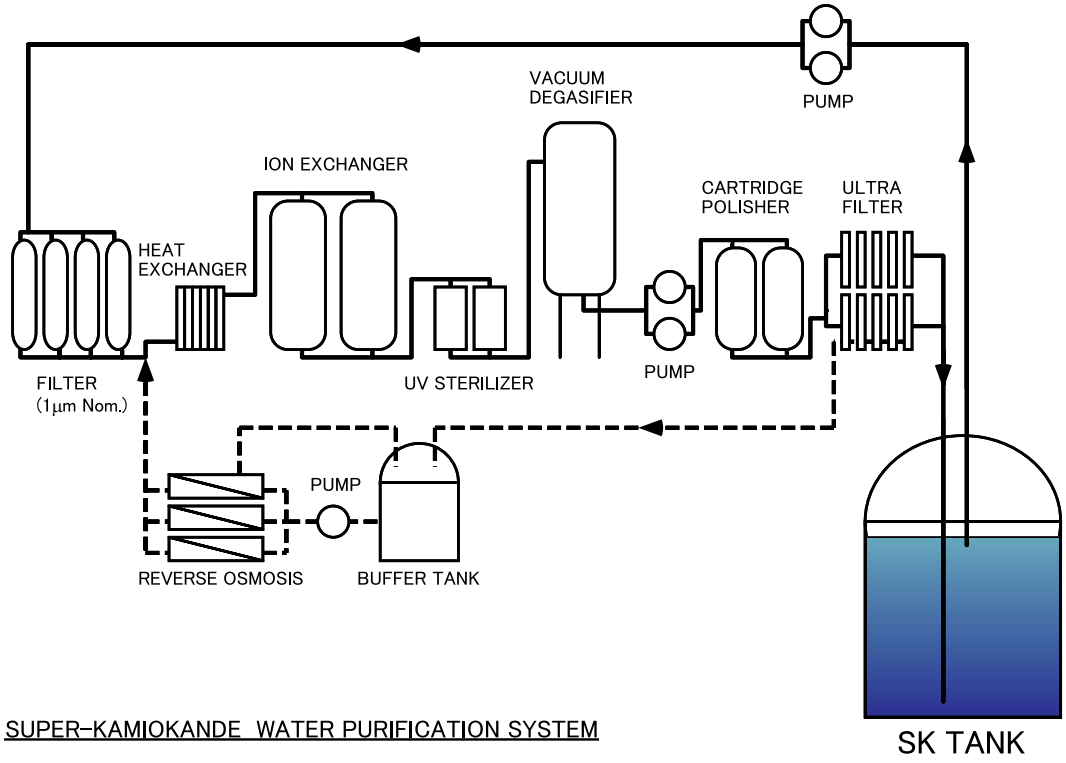

Figure 2.5: A flow diagram of the water purification system.

2.5 Data acquisition system

Electronics for the inner detector

A block diagram of the electronics for the inner detector is shown in Fig. 2.6. Signal cables from the inner PMTs are fed into the TKO (Tristan-KEK-Online) system. The TKO system consists of GONG (GO and NoGo trigger distribution module), ATM (Analog Timing Module) and SCH (Super Controller Header, bus-interface module). Most of signal processing is done by the ATM module, which can measure the charge and timing of each input PMT signal. The details of the ATM are described in [17]. In the Super-Kamiokande experiment, 960 ATM cards are used in 48 TKO crates. Each TKO crate accommodates one SCH and one GONG.

At first, the inner PMT signals are digitized in the ATM, which provides a 1.2 μs full range with 0.3 ns resolution in time and a 550 pC full range with 0.2 pC resolution (0.1 p.e.) in charge for each PMT. The ATM has 12 input channels and each channel has switching two TACs (Time to Analog Converter) and two QACs (Charge to Analog Converter) to provide deadtime free recording. If a signal exceeds the threshold, a HITSUM pulse is issued on the front panel and is used to generate the global trigger.

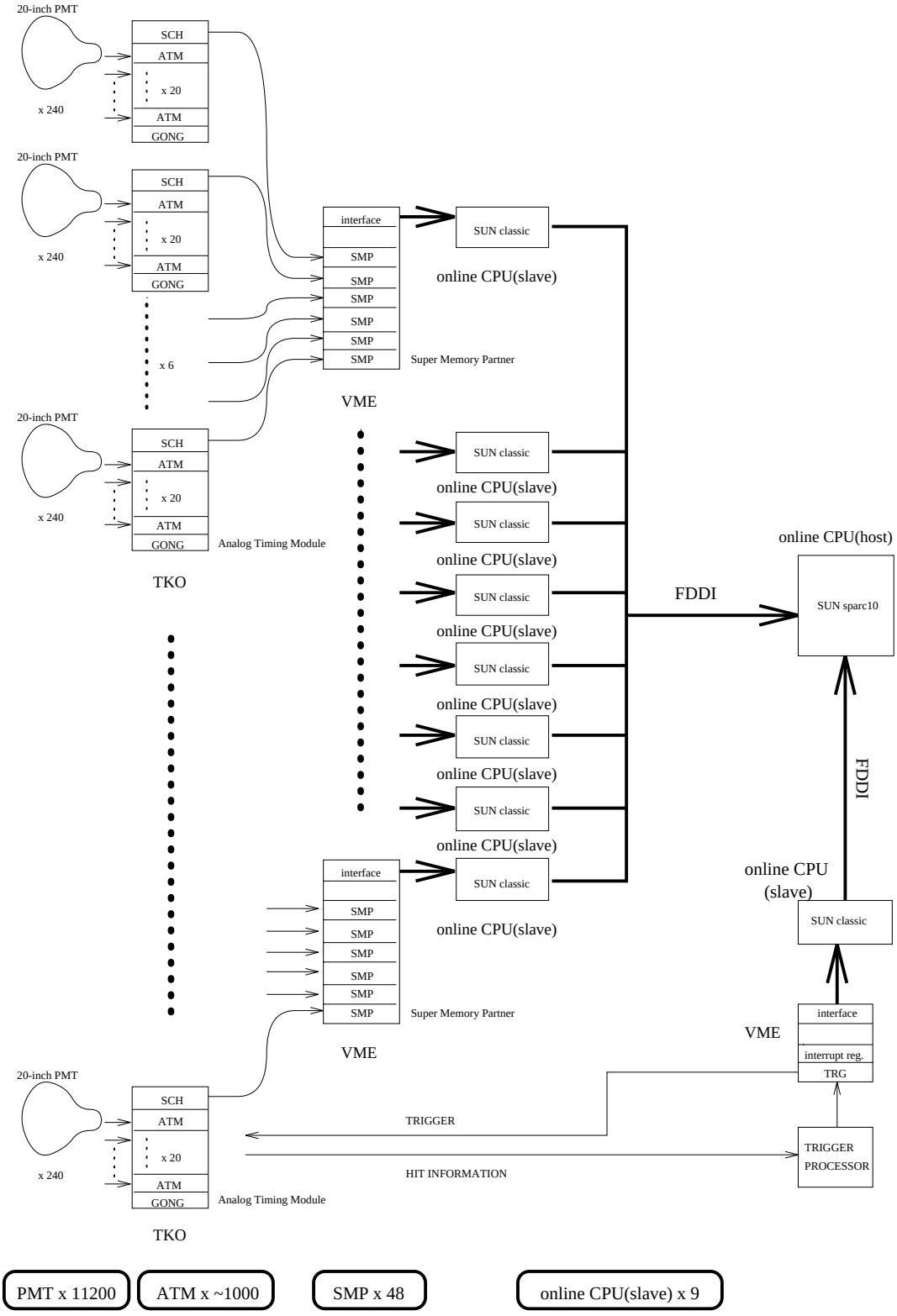

Figure 2.6: Inner detector data acquisition system.

The pulse height of the HITSUM signal indicates the total number of hit PMTs within a 200nsec window.

The data in the ATM memory are read out every 16 global triggers and stored in the data buffer modules called SMP (Super Memory Partner) through the SCH. The SMP has two 1Mbyte memories and each memory is read out in turn by the front-end work station(Sun-Classic). In total 8 front-end work stations are arranged in four electronics hut. The global trigger is controlled by a work station (Sun SPARKstation 10) in the central hut.

Electronics for the outer detector

The electronics used in the outer detector are completely different from those used in the inner detector. Signals from 8-inch PMTs are connected to a charge to time converter(QTC) module which generates a rectangular pulse with a width proportional to the input charge. The pulses, which carry the time and charge information, are digitized by a LeCroy 1877 multi-hit TDC (Time to Digital Converter). The TDC has 96 input channels and the minimum time unit of the TDC is 0.5nsec. This TDC can record multi-hits within a 16μsec window. The timing of the trigger in this 16μsec window is set to -10 to +6μsec relative to the global trigger timing. The TDC is a FASTBUS module and its crate is controlled by a FASTBUS Smart Crate Controller (FSCC). The FSCC sends the digitized PMT data from TDCs to the dual ported memory(DPM) modules. Finally these data are read out by the OD data taking work station through a VME bus.

Trigger system

There are two kinds of triggers for the inner detector, LE(low energy) trigger and HE(high energy) trigger. The difference between these triggers is only a discriminator threshold for the HITSUM signal. The discriminator threshold is 29 hits equivalent for the LE trigger and 31 hits equivalent for the HE trigger. At the time of this writing, the threshold of the global trigger is identical with the LE trigger, which corresponds to an electron energy of about 5.7 MeV. For events with the visible energy above 30MeV, the trigger efficiency is 100%. Once the global trigger is generated, the TRG module distributes the trigger signal to all ATMs through the GONG modules. The trigger rate for the LE trigger is 10-12Hz and for the HE trigger is 5-6Hz. It is stable all the year.

For PMTs in the outer detector, the OD-trigger is generated by using the hitsum signal of the outer PMTs. The discriminator threshold is set to be equivalent to 19 hits

within a 200nsec window. OD-trigger is used to identify cosmic-ray muons. The trigger rate of the OD-trigger is $\sim$3Hz.

Online and Offline system

Each front-end work station reads out the data from electronics independently, converts the raw data to a simple online format and sorts the data in order of the event number. All the information from the inner and outer detectors is collected and merged into an event by the "event builder" program running on the host computer. The data is sent to the offline computing system every subrun, which has 10-minute of data and is about 100Mbyte in size. On the offline computers the data format is converted to the offline format(ZBS, Zebra Bank System) and stored in the magnetic tape library.

Chapter 3

Calibration

In order to get precise information of an event, it is necessary to calibrate the gain and timing response of each PMT and to measure the water transparency.

In this chapter the method of relative gain calibration, absolute gain calibration, timing calibration, and water transparency measurement is presented. The relative gain calibration adjusts the gain of all the PMTs. The absolute gain calibration is to find a relation between a measured photoelectron numbers and the energy of an event. The timing calibration is to find a relation between the measured TDC counts and the arrival time of the input signal.

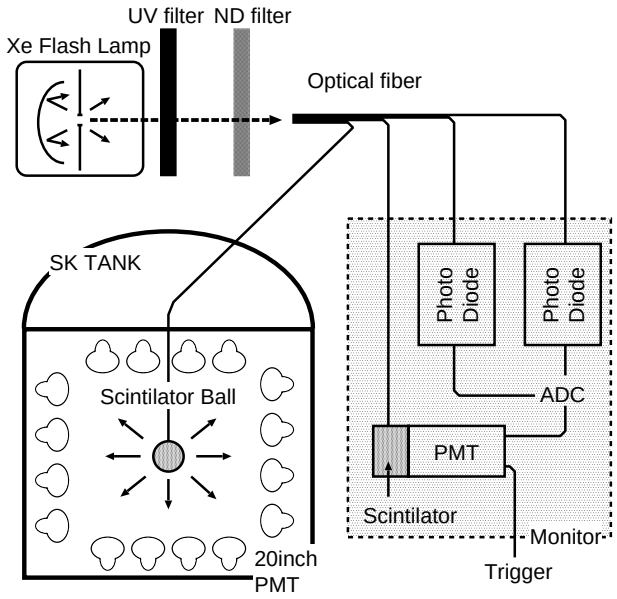

Figure 3.1: The relative gain calibration system.

3.1 Relative gain calibration

We use a Xe lamp and scintillator ball system in order to calibrate the relative gain of the PMTs. Fig. 3.1 shows the setup of the relative gain calibration system. Light from the Xe flash lamp, which is used as the light source, passes through a UV filter and ND filter to match the wavelength with the Cherenkov light and to adjust the light intensity, respectively. Then the light reaches the scintillator ball via an optical fiber. To emit isotropic light, the scintillator ball is made of acrylic resin in which 50ppm BBOT and 500ppm MgO powder are uniformly mixed. The BBOT is used as a wavelength shifter and the MgO is used as a light diffuser. Typical wave length of the light is 440 nm.

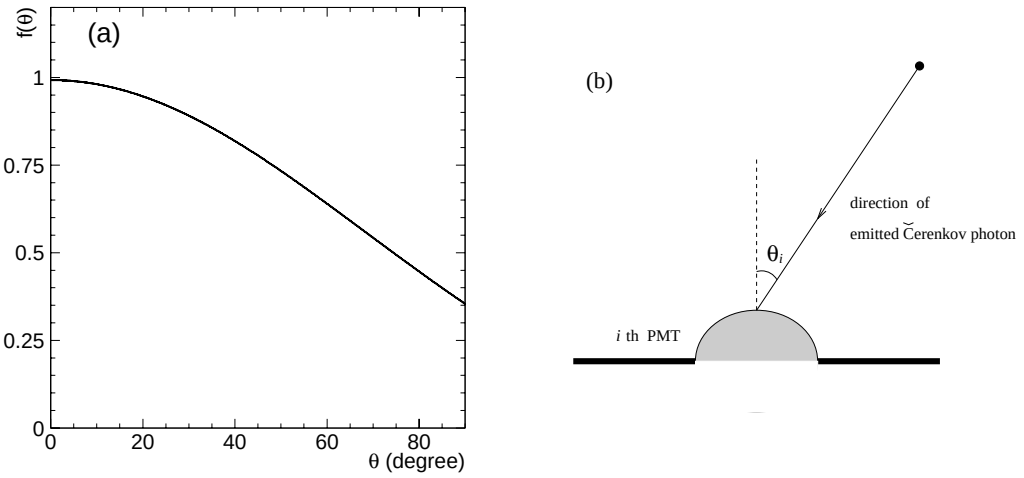

Figure 3.2: (a)Relative PMT photo sensitive area as a function of angle, θ and (b)the definition of θ.

The relative gain of the i-th PMT is expressed by the following equation,

$$G_i = \frac{Q_i}{f(\theta)} \times r_i^2 \times \exp(\frac{r_i}{L}) \ / \ Q_0, \tag{3.1}$$

where $f(\theta)$ is the relative photosensitive area of the PMT viewed from an angle θ as shown in Fig. 3.2, Q_i is the charge in units of pC detected by the i-th PMT, r_i is the distance between the scintillator ball and i-th PMT, L is the light attenuation length in the detector and Q_0 is the normalization factor to adjust the average G_i equal to 1. We set the high-voltage (HV) value of each PMT so that all PMTs have a common gain. We took the data for the relative gain calibration 9 times by changing the position of the scintillator ball from 1 m to 35 m in height from the bottom PMT surface in order to minimize the r_i and $f(\theta)$ dependence to each PMT.

After the relative gain correction, we took the data with the same system again to check the relative calibration. And the gain spread is estimated to be 7% as shown in

Fig. 3.3. Since the number of hit PMTs is typically ∼1300 for atmospheric neutrino events, ambiguity from the relative gain spread is estimated to be only ∼0.2%.

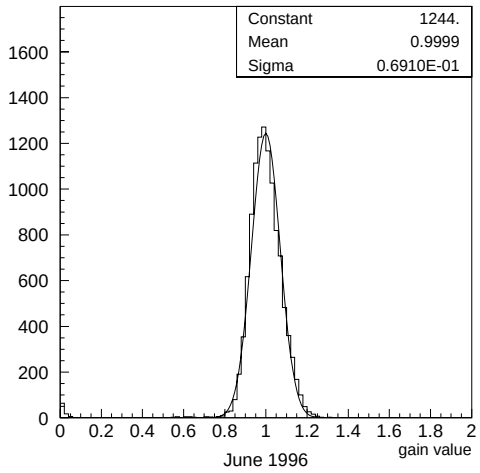

Figure 3.3: The relative gain distribution after the HV adjustment. Solid line shows the fitting result.

3.2 Single photoelectron distribution

The absolute gain of the PMT is calibrated by measuring the charge of single photoelectron(p.e.). In order to take the single p.e. data, we use low energy gamma-rays emitted from thermal neutron capture in nickel, Ni(n,γ)Ni*, because the number of p.e. in a PMT is at most one. Neutrons are produced by spontaneous fission of ^{252}Cf. Fig. 3.4 shows a schematic view of the Ni-Cf source. The ^{252}Cf source and Ni+water mixture are put into a cylindrical polyethylene case. Energies of emitted gamma-rays are listed in Table 3.1.

Reaction	Energy of the γ-ray (MeV)	Natural abundance of the initial element (%)	Cross section (barn)
^{58}Ni(n,γ)^{59}Ni*	9.0	67.88	4.4
^{60}Ni(n,γ)^{61}Ni*	7.8	26.23	2.6
^{62}Ni(n,γ)^{63}Ni*	6.8	3.66	15

Table 3.1: Properties of Ni(n,γ)Ni* reactions. There exist many more lines with small branching ratios.

The single p.e. distribution for a typical PMT is shown in Fig. 3.5. The horizontal

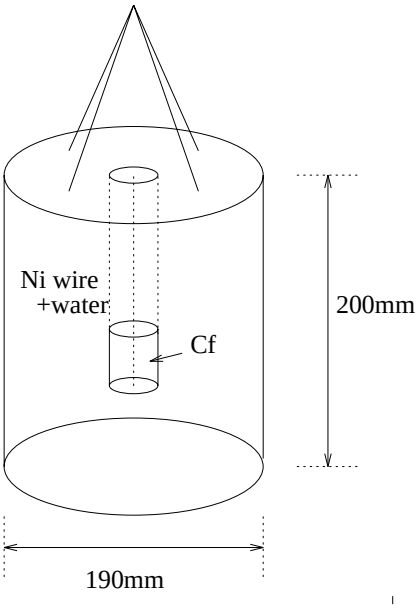

Figure 3.4: Schematic view of the Ni-Cf gamma-ray source.

axis shows detected charge in units of pico coulomb(pC). Since the mean value of this charge distribution above a threshold, which corresponds to about 0.25p.e., is 2.055pC, the relation between pC and p.e. is

$$1p.e. = 2.055pC.$$

We tabulate the mean values for all PMTs and refer to this table everytime we translate the charge to the number of p.e.

The shape of the single p.e. distribution is also used in the Monte Carlo simulation.

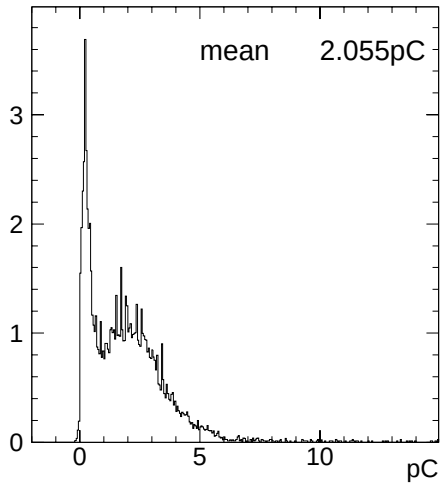

Figure 3.5: Single photoelectron distribution.

3.3 Timing Calibration

Timing response differs for each PMT because of the following two factors:

1. transit-time difference of the PMT.

2. timing response of the discriminator.

Transit-time difference depends mainly on high voltage applied to the PMT. And the discriminator has an effect that larger pulses tend to cross the threshold earlier than smaller ones (slewing effect).

To minimize the systematic error in the timing calibration, the pulse width of calibration light should be narrow. Therefore we used a dye laser pumped by a pulsed N_2 laser to measure the timing response of each PMT. The pulse width and wavelength of the dye laser is $\sim$4 ns (full width) and 384 nm, respectively.

The laser light goes through several optical filters which control light intensity and reaches a diffusing ball via an optical fiber. The diffusing ball is suspended at the center of the tank and reemits laser light isotropically. Fig. 3.6 shows timing response of a typical PMT as a function of the observed photoelectrons, Q. This Q-dependence of the timing is called TQ map[1]. We obtained TQmaps for all the PMTs. The TQmap corrects for the relative time difference of the PMT. The timing resolution can be estimated from the TQmap by fitting the T distribution with a Gaussian distribution, which is shown in Fig. 3.7. It is used in the Monte Carlo simulation.

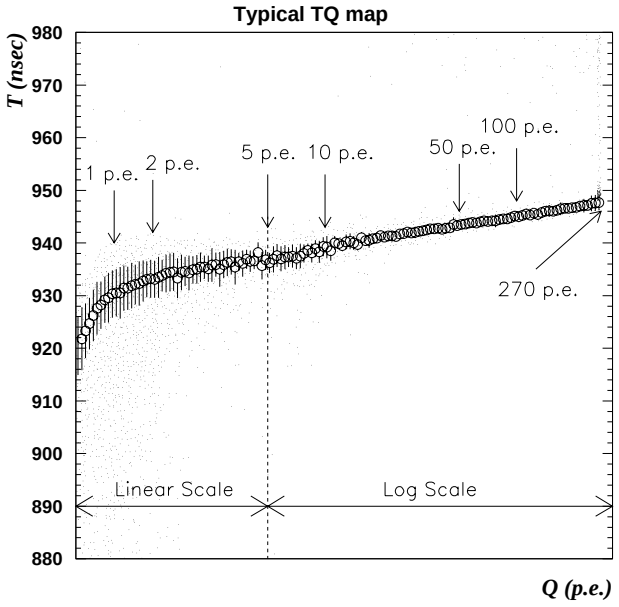

Figure 3.6: A TQ map of a typical PMT. Circles and error bars show peak values and resolutions (1σ level).

[1] T(timing)-Q(charge) map

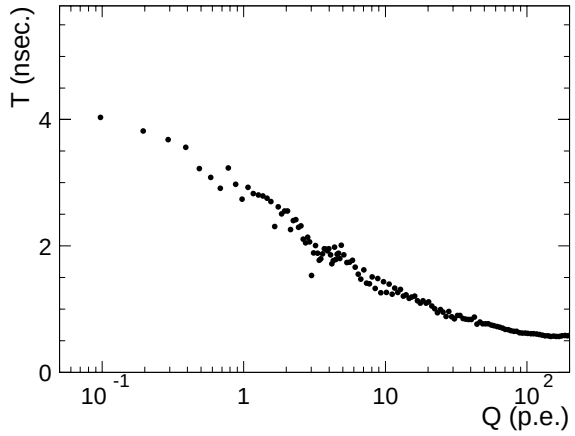

Figure 3.7: Timing resolution of a PMT as function of Q (p.e.).

3.4 Water transparency

We measure the light attenuation length in water by means of two independent methods. One method uses a dye laser and CCD camera. By changing the dye of the laser, we can measure the wavelength dependence of the attenuation length. Another method uses cosmic-ray muons. This method cannot measure the wavelength dependence, but it does not need to stop normal data taking and is able to check the stability of water transparency continuously.

The following subsections present the methods and results of the water transparency measurement by two independent ways.

Laser and CCD camera method

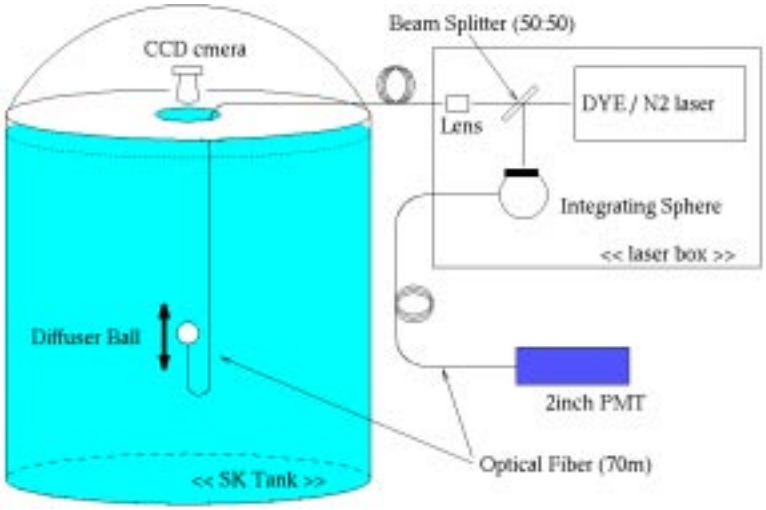

Figure 3.8: Set up of the dye-laser + CCD camera system.

The setup of the dye laser plus CCD camera system is shown in Fig. 3.8. The light source is a dye laser pumped by a pulsed N_2 laser. The emitted light is divided into two optical fibers, one is connected to a 2-inch PMT to monitor the intensity of the light (I_{laser}) and the other is connected to the diffuser ball. The diffuser ball emits light in the water isotropically and the CCD camera takes an image of the diffuser ball and measures the intensity of the light which is attenuated in the water (I_{CCD}). The depth of the diffuser ball (l_d) is changed from 5m to 30m and at each point I_{laser} and I_{CCD} are measured four times. The attenuation length, $L(\lambda)$, is calculated by the following equation.

$$\frac{I_{CCD}}{I_{laser}} = const. \times \exp\left(-\frac{l_d}{L(\lambda)}\right), \tag{3.2}$$

where λ is the wave length of the light. Fig. 3.9 shows an example of the $\frac{I_{CCD}}{I_{laser}}$ plot as a function of l_d when the wave length is set to 420nm. The data is fitted with a least square method and the attenuation length at 420nm is determined to be 92.2 m $\pm$ 5.2 m. (It has been improved and is 101 $\pm$ 6m as of November, 1997.) The results at various wave lengths are summarized in Fig. 3.10. In this figure, the solid lines show the estimation of Rayleigh scattering, mie scattering and absorption of light, which are considered in our Monte Carlo simulation. Now, the study of the light attenuation and scattering by using this system is continuing to understand more details of water characteristics and to tune the Monte Carlo simulation.

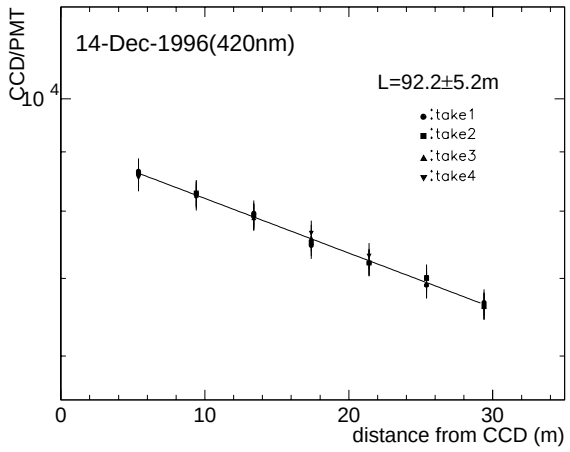

Figure 3.9: The light attenuation length at 420nm.

Cosmic-ray muon method

The light attenuation length is also measured by cosmic-ray muons which enter from the top wall and exit to the bottom wall. The number of p.e. detected by each PMT, Q, is

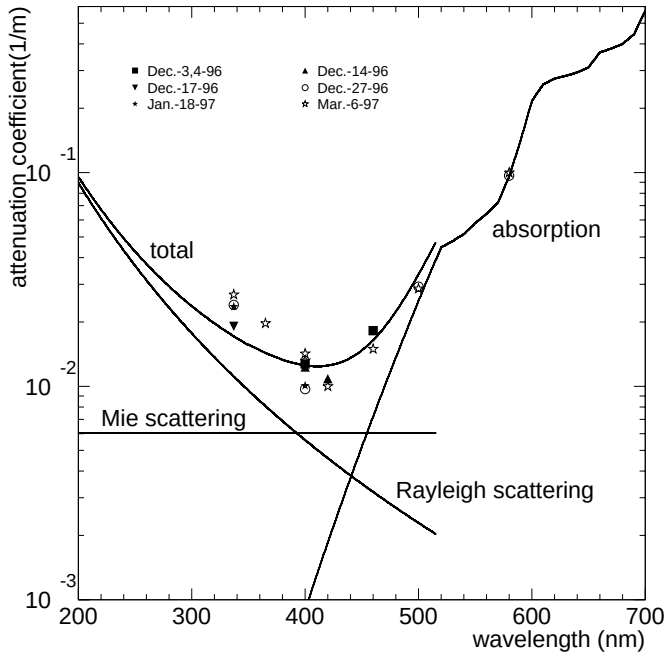

Figure 3.10: The $L(\lambda)^{-1}$ plot as a function of the wave length. Solid lines show the attenuation length used in Monte Carlo simulation.

expressed by the following equation:

$$Q = const. \times \frac{f(\theta)}{l} \times \exp(-\frac{l}{L}), \tag{3.3}$$

where l is the flight length of the Cherenkov photon, and L is the attenuation length of the Cherenkov light. Eq.3.4 can be rewritten as

$$\log\left(\frac{Ql}{f(\theta)}\right) = -\frac{1}{L}l + \log(const.) \tag{3.4}$$

Fig. 3.11 shows $\log\left(\frac{Ql}{f(\theta)}\right)$ plot against l in a typical run. The attenuation length is obtained from the fitted slope. The attenuation length, L, in run 3106(Nov.15, 1996) is 105.4$\pm$0.5m (error of the fitting). Since the absolute value of L depends strongly on the method and parameter of the fitting, we use the attenuation length measured by this method only for monitoring possible time variation of the attenuation length, which causes a small difference between MC and data. The attenuation length is calculated every run. The time variation of the attenuation length is shown in Fig. 3.12. In this figure, to reduce the statistical fluctuation, each plot shows the average attenuation length of 30 runs. From 200days to 300days, the attenuation length increased. It is due to installation of the ultra-filter in the water purification system. We tabulate these time variations and use this table to correct for particle momenta.

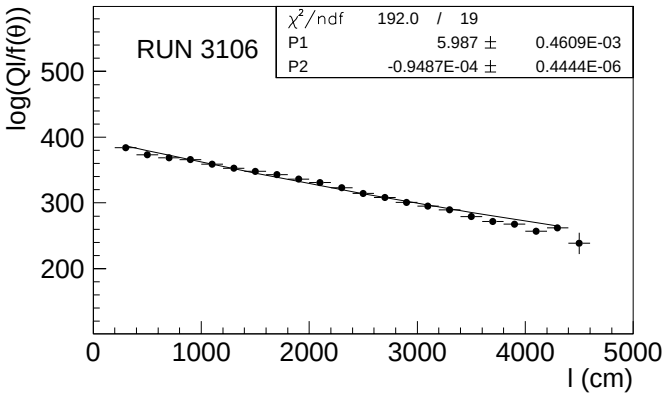

Figure 3.11: The $\log\left(\frac{Ql}{f(\theta)}\right)$ plot as a function of l. The solid line shows the result of fitting.

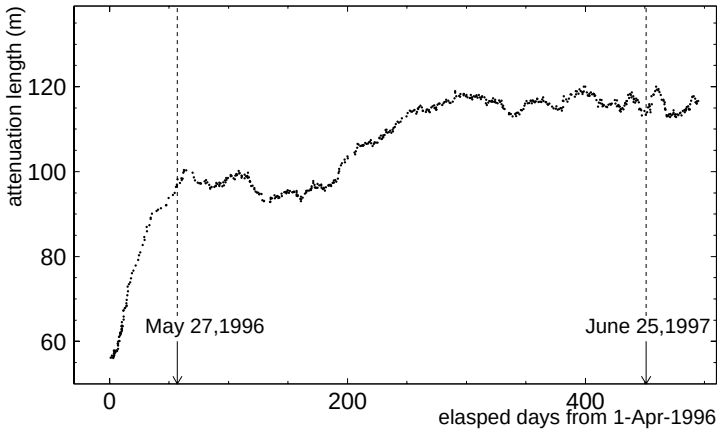

Figure 3.12: Time variation of light attenuation length in water measured by cosmic-ray muons.

Chapter 4

Simulations

4.1 Atmospheric neutrino flux

Atmospheric neutrinos are produced by interactions of cosmic-rays and decays of their secondary particles in the atmosphere. To calculate the flux of atmospheric neutrinos, we must know the primary cosmic-ray flux, models for particle interactions and the atmospheric structure. Additionally the effect of geomagnetic field must be considered for low energy cosmic-rays because of the rigidity (=momentum/charge) cutoff.

The observed primary cosmic ray fluxes are shown in Fig. 4.1. They consist of $\sim$95% protons, $\sim$4.5% helium nuclei, and $\sim$0.3% CNO nuclei for the energy above $\sim$2GeV/nucleon. Primary cosmic rays have a power spectrum of $E^{-2.7}$ above 5GeV. The spectrum of low energy cosmic rays is affected by the solar activity as shown in Fig. 4.1, because the solar wind drives the low energy cosmic rays away and the strength of the solar wind varies with solar activity. The uncertainty in the absolute primary cosmic ray flux is estimated to be $\sim$15%.

The primary and secondary cosmic rays are affected by the geomagnetic field. If the rigidity of a cosmic ray is lower than the rigidity cutoff, the cosmic ray cannot enter the atmosphere. The value of the rigidity cutoff depends on the experimental site and arrival direction of cosmic rays.

The atmospheric neutrino flux has been calculated by a number of theorists. We adopt Honda's latest calculation[1], because he took into account the effect of the geomagnetic field at the Super-Kamiokande site and covers the neutrino energies from 30MeV to 1TeV. Fig. 4.2 shows the energy spectra for $\nu_\mu + \bar{\nu_\mu}$ and $\nu_e + \bar{\nu}_e$ at the Super-Kamiokande site, compared with other calculations. In Fig. 4.3, the flux ratios are shown for various calculations. It is important that, although the absolute atmospheric neutrino fluxes

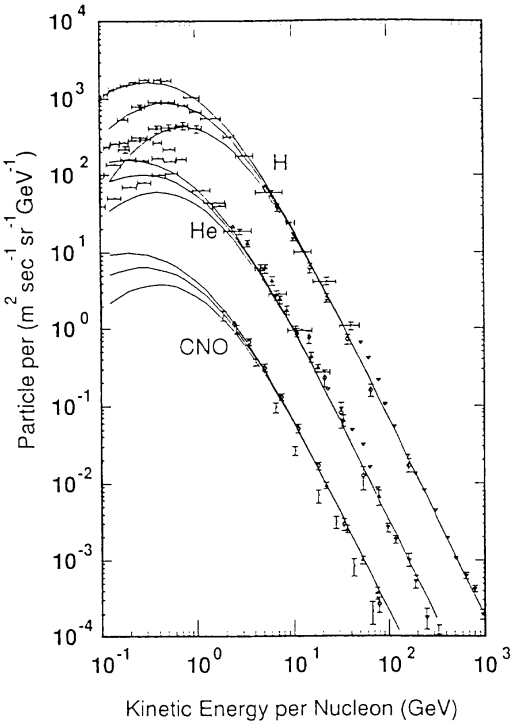

Figure 4.1: Observed fluxes of cosmic-ray hydrogen, helium and CNO nuclei as a function of kinetic energy per nucleon. The three lines are the fluxes adoopted for calculation at solar max, mid, and min. [1]

differ among calculations, the ratio, $(\nu_\mu + \bar{\nu_\mu})$ / $(\nu_e + \bar{\nu_e})$, is very similar. The uncertainty in the absolute neutrino flux is estimated to be $\sim$20%, while the uncertainty in the above ratio is less than 5% because the ambiguity in the absolute flux is cancelled out by taking the ratio.

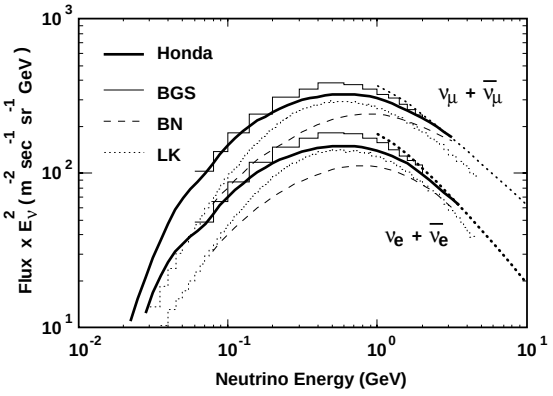

Figure 4.2: The atmospheric neutrino fluxes multiplied by E_ν^2 at the Super-Kamiokande site, compared with Barr,Gaisser and Stanev[18], Bugaev and Naumov[19], and Lee and Koh[20]. The solid lines show the HONDA flux at solar mid. The dotted lines are the calculation without the rigidity cutoff at high energies where the geomagnetic effect becomes negligible.

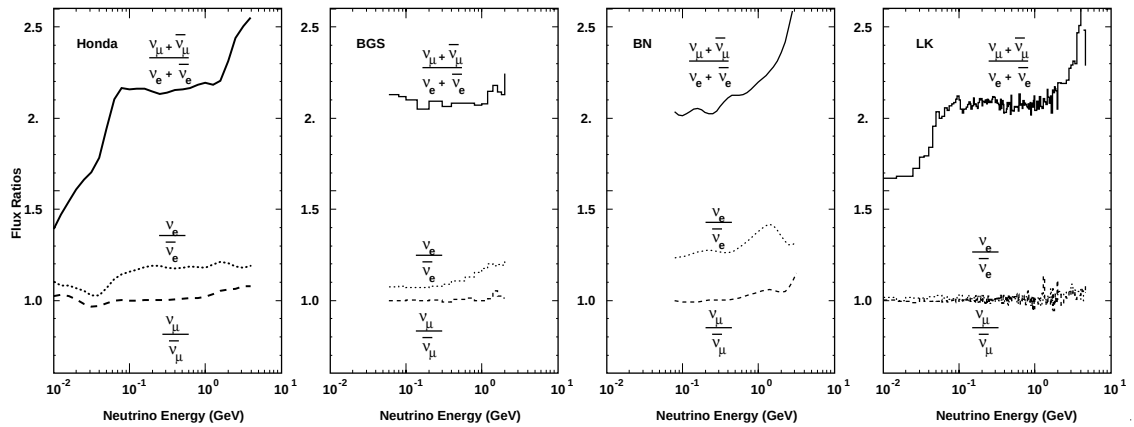

Figure 4.3: The flux ratio,$(\nu_\mu + \bar{\nu}_\mu)/(\nu_e + \bar{\nu}_e)$, at the Super-Kamiokande site calculated by Honda, BGS, BN, and LK.

4.2 Neutrino interactions

Atmospheric neutrinos interact with nucleons and orbital electrons in water via charged current(CC) and neutral current(NC) interactions. However, neutrino interaction with an electron can be safely neglected in the ∼1GeV energy region. Therefore in our Monte Carlo the following 8 interactions are taken into account[21]:

1. CC quasi-elastic scattering $\nu N \to lN'$
2. NC elastic scattering $\nu N \to \nu N'$
3. CC single-pion production $\nu N \to lN'\pi$
4. NC single-pion production $\nu N \to \nu N'\pi$
5. CC multi-pion production $\nu N \to lN'm\pi (m \geq 1)$
6. NC multi-pion production $\nu N \to \nu N'm\pi (m \geq 1)$
7. CC coherent pion production $\nu^{16}O \to l\pi^{16}O$
8. NC coherent pion production $\nu^{16}O \to \nu\pi^{16}O$

Where N is a nucleon and l is a charged lepton. The details of these interactions are described in the following subsections.

4.2.1 Quasi-elastic interactions

For the CC quasi-elastic interaction, the energy and momentum of a lepton in the final state are determined from the q^2 ($q = p_\nu - p_l$: 4-momentum transfer)- dependence of the cross section. This cross section is calculated by the standard $V-A$ theory, with $M_A = 1.01$ GeV/c^2 and $M_V = 0.84$ GeV/c^2[22]. Fig. 4.4 and Fig. 4.5 show the calculated total cross sections of $\nu_\mu n \to \mu^- p$ and $\bar{\nu_\mu} p \to \mu^+ n$, respectively together with experimental data. From these comparisons systematic uncertainties for the Monte Carlo simulation are estimated later.

Since the target is H_2O, we take into account the Fermi motion of nucleons in a nucleus and Pauli blocking for the ν-^{16}O scattering. The Fermi momentum distribution in ^{16}O is estimated from the e-^{12}C scattering experiment [23]. The Fermi gas model is adopted to consider the Pauli blocking. Momentum of a recoil nucleon must be larger than the Fermi surface momentum (250MeV/c).

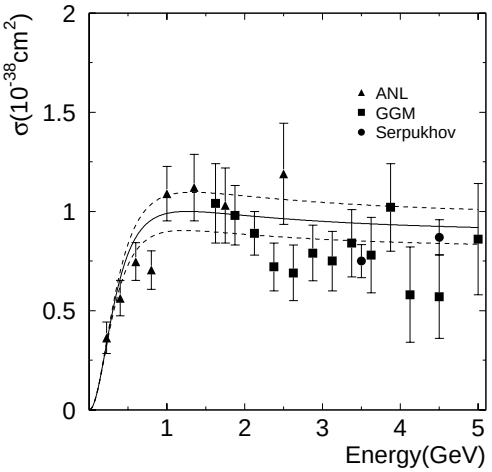

Figure 4.4: Calculated cross section of $\nu_\mu n \to \mu^- p$ compared with the experimental data, ANL[24], GGM[25], and Serpukhov[26]. Upper and lower dashed lines show the calculated cross sections with $M_A = 1.11$ and 0.91, respectively.

For the NC elastic interaction, we use the following relations according to Ref.[28],[29].

$$\begin{aligned}
\sigma(\nu p \to \nu p) &= 0.153 \times \sigma(\nu n \to e^- p) \\
\sigma(\bar{\nu} p \to \bar{\nu} p) &= 0.218 \times \sigma(\bar{\nu} p \to e^+ n) \\
\sigma(\nu n \to \nu n) &= 1.5 \times \sigma(\nu p \to \nu p) \\
\sigma(\bar{\nu} n \to \bar{\nu} n) &= 1.0 \times \sigma(\bar{\nu} p \to \bar{\nu} p)
\end{aligned}$$

NC elastic interactions are visible only if the recoil proton emits Cherenkov light or the recoil nucleon interacts in water and produces pions.

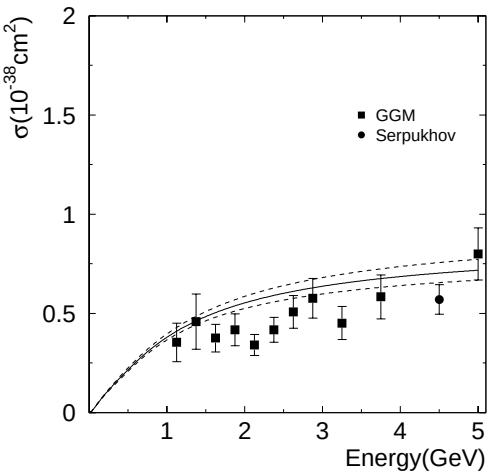

Figure 4.5: Calculated cross section of $\bar{\nu_\mu} p \to \mu^+ n$ compared with the experimental data, GGM[27] and Serpukov. Upper and lower dashed lines show the calculated cross sections with $M_A = 1.11$ and 0.91, respectively.

4.2.2 Single pion production

We use Rein-Sehgal's method to simulate the single pion production[30] for the hadronic invariant mass less than 1.4GeV. In this method, the neutrino interaction is separated into two parts as follows:

$$\begin{aligned} \nu + N &\to l + N^* \\ N^* &\to \pi + N \end{aligned}$$

N^* represents baryon resonances. In this simulation 18 resonances below 2GeV are used and interferences among resonances are also taken into account. We calculate the amplitude of each resonance production and multiply the decay probability of each resonance with the restriction of invariant mass less than 1.4GeV. Fig. 4.6-4.8 show the calculated total cross sections compared with experimental data. Agreements are excellent. Fig. 4.9 shows the total cross section for CC and NC single pion production.

The angular distribution of pions from $\Delta(1232)$ resonance is also calculated by using this model. The $\Delta(1232)$ resonance is dominant in single pion production, especially for the low energy region. The angular distribution of pions is assumed to be isotropic for other resonances, because the experimental data do not exhibit any significant deviation from isotropy.

4.2.3 Multi-pion production

In high energy neutrino-nucleon interactions, the cross section and kinematics are determined under the assumption of Bjorken scaling. The total cross section of multi-pion

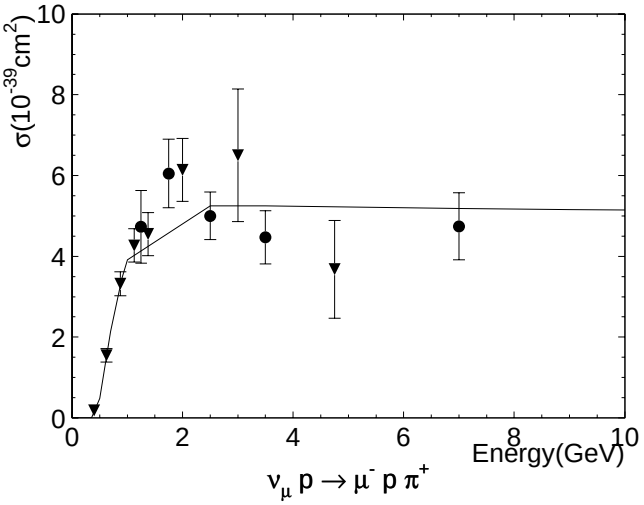

Figure 4.6: Cross section of $\nu_\mu p \rightarrow \mu^- p \pi^+$ compared with the experimental data.

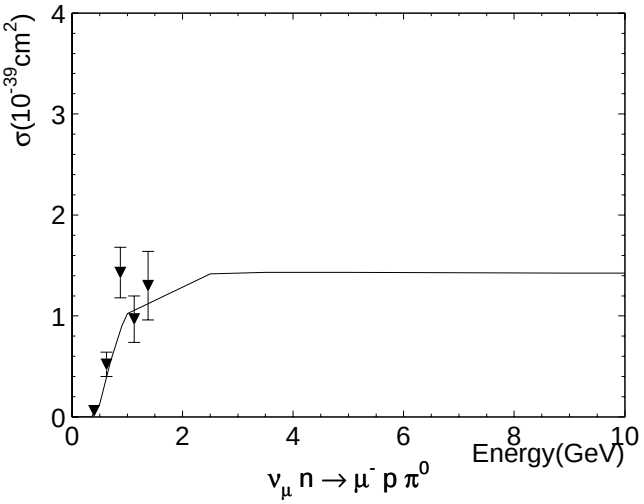

Figure 4.7: Cross section of $\nu_\mu n \rightarrow \mu^- p \pi^0$ compared with the experimental data.

production is calculated by integrating $\frac{d^2\sigma}{dxdy}$ with an invariant mass above 1.4GeV/c.

The mean multiplicity of charged pions, $\langle n_\pi \rangle$, is estimated from the Fermilab 15-foot hydrogen bubble chamber experiment[31], based on the reaction, $\bar{\nu_\mu} p \rightarrow \mu^+ +$hadrons, as:

$$\langle n_\pi \rangle = 0.09 + 1.83 \ln W^2, \tag{4.1}$$

where W is the invariant mass. The forward-backward multiplicity asymmetry is taken into account using the BEBC data[32], and we set $\langle n_\pi^F \rangle$ / $\langle n_\pi^B \rangle$ = (0.35+0.41lnW^2) / (0.5+0.09lnW^2).

For the NC cross section, we use the following relations;
$E_\nu \leq 3$GeV,

$$\frac{\sigma(\nu N \rightarrow \nu X)}{\sigma(\nu N \rightarrow \mu^- X)} = 0.26$$

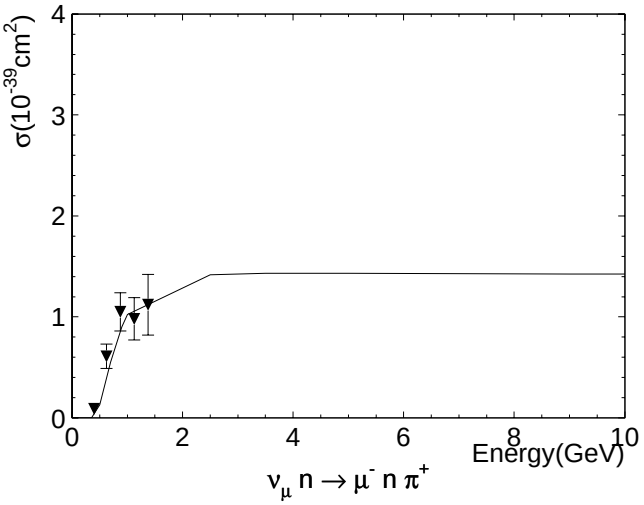

Figure 4.8: Cross section of $\nu_\mu n \to \mu^- n\pi^+$ compared with the experimental data.

$$\frac{\sigma(\bar{\nu}N \to \bar{\nu}X)}{\sigma(\bar{\nu}N \to \mu^+X)} = 0.39$$

$3\text{GeV} < E_\nu < 6\text{GeV}$,

$$\frac{\sigma(\nu N \to \nu X)}{\sigma(\nu N \to \mu^- X)} = 0.26 + 0.04 \times ((E_\nu - 3.)/3.)$$
$$\frac{\sigma(\bar{\nu}N \to \bar{\nu}X)}{\sigma(n\bar{u}N \to \mu^+X)} = 0.39 - 0.02 \times ((E_\nu - 3.)/3.)$$

$6\text{GeV} < E_\nu$,

$$\frac{\sigma(\nu N \to \nu X)}{\sigma(\nu N \to \mu^- X)} = 0.30$$
$$\frac{\sigma(\bar{\nu}N \to \bar{\nu}X)}{\sigma(n\bar{u}N \to \mu^+X)} = 0.37$$

from the Gargamelle experiment[33]($E_\nu \leq 3\text{GeV}$) and Ref.[34]($3\text{GeV} < E_\nu$), which measured the ratio of various inclusive total cross sections of NC to CC interactions. Fig. 4.10 shows the calculated cross sections for CC and NC interactions.

4.2.4 Coherent pion production

Pions are also produced by a coherent interaction off the oxygen nucleus. It produces single pions with very little momentum transfer. Therefore the angular distribution has a sharp peak in the forward direction.

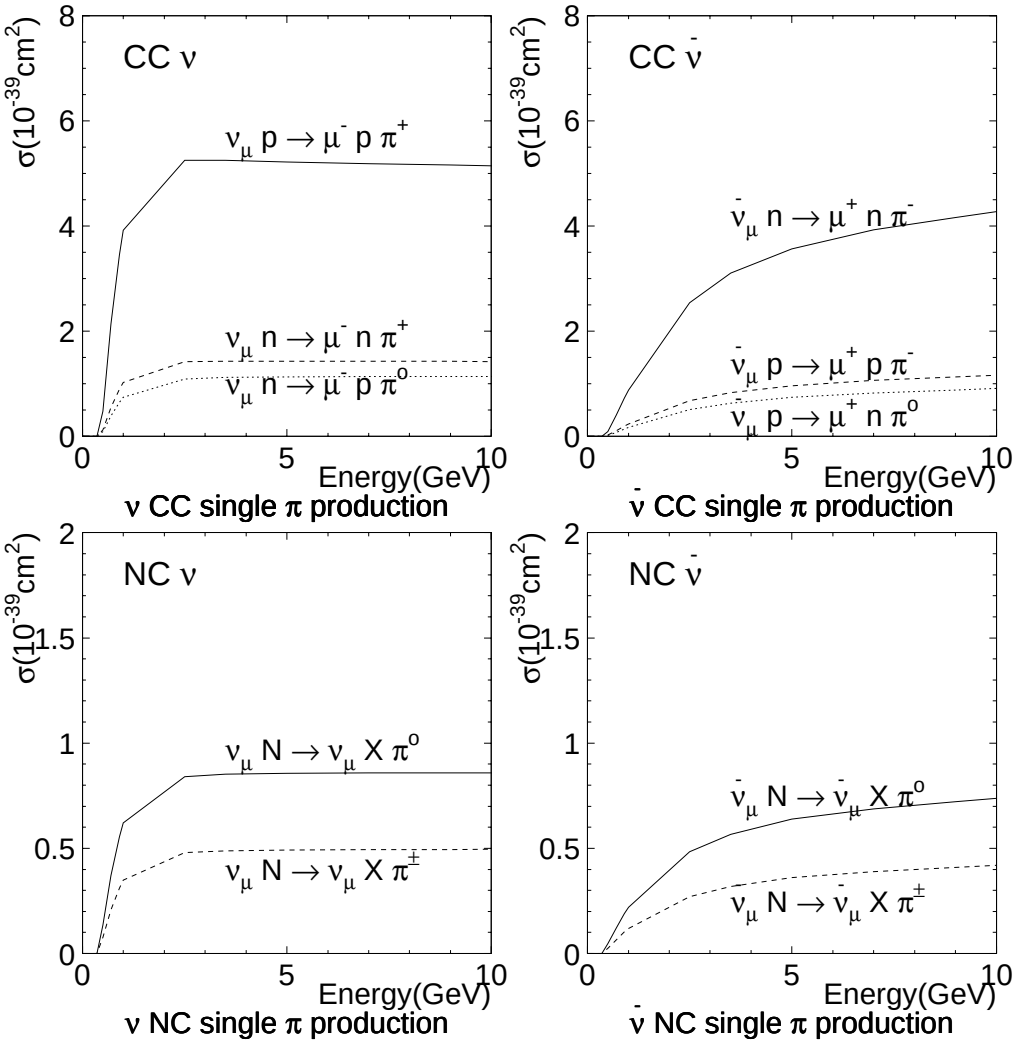

Figure 4.9: Cross sections of single pion productions for CC and NC interactions.

Calculated cross-sections for CC and NC coherent pion production is shown in Fig. 4.11, which is based on the Rein and Sehgal calculation [35].

4.3 Meson nuclear effects

Pions, produced in a nucleus by a neutrino interaction, sometimes undergo secondary interactions before leaving the nucleus. In our Monte Carlo simulation program, the following pion interactions in ^{16}O are considered: inelastic scattering, charge exchange, and absorption. We use a cascade model in simulating these pion nuclear effect. The actual procedure is as follows. The nucleon density distribution is assumed to be given

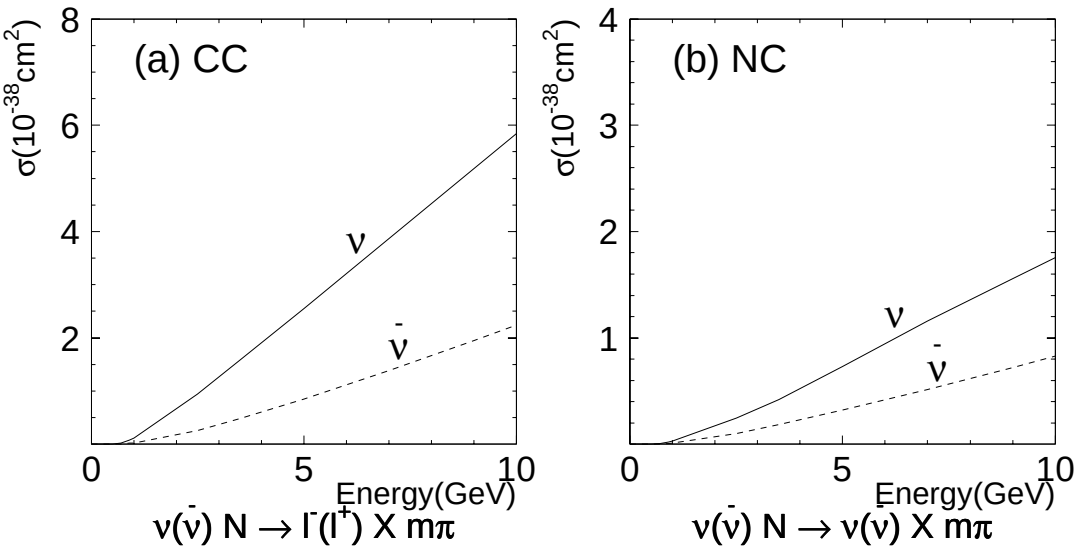

Figure 4.10: Cross sections of multi-pion productions for (a)CC and (b)NC interactions. Solid lines show the cross sections for the ν and dashed lines show the cross sections for the $\bar{\nu}$.

by the Woods-Saxon function,

$$\rho_p(\mathbf{r}) = \frac{Z}{A}\bar{\rho}\{1 + \exp(\frac{|\mathbf{r}| - c}{a})\}^{-1}, \tag{4.2}$$

where A is the atomic number, $\bar{\rho}$ is the average density of nuclei and a, c are the density parameter of nucleus. The mean free path is calculated for an incident pion, also taking into account the Fermi motion of the nucleon in ^{16}O[36] and the Pauli blocking effect. The interaction point of the pion is then determined. The type of interaction is determined next. If the inelastic scattering or the charge exchange occurred, the direction and momentum of the pion are determined by using the result of phase shift analysis obtained from the $\pi - N$ scattering experiments[37]. The Pauli blocking effect is taken into account here by requiring that the nucleon momentum after the interaction must be larger than the Fermi surface momentum, $P_F(\mathbf{r})$.

$$P_F(\mathbf{r}) = (\frac{3}{2}\pi^2\rho_p(\mathbf{r}))^{\frac{1}{3}}. \tag{4.3}$$

These pion interactions are tested in $\pi^{12}C$[38] and $\pi^{16}O$[39] scatterings. Fig. 4.12 shows the simulated cross sections compared with the experimental data. Agreement is quite reasonable.

The pion interaction simulation is also tested in a photo-pion production process. To simulate the photo-pion production, we use the measured value for the cross section of

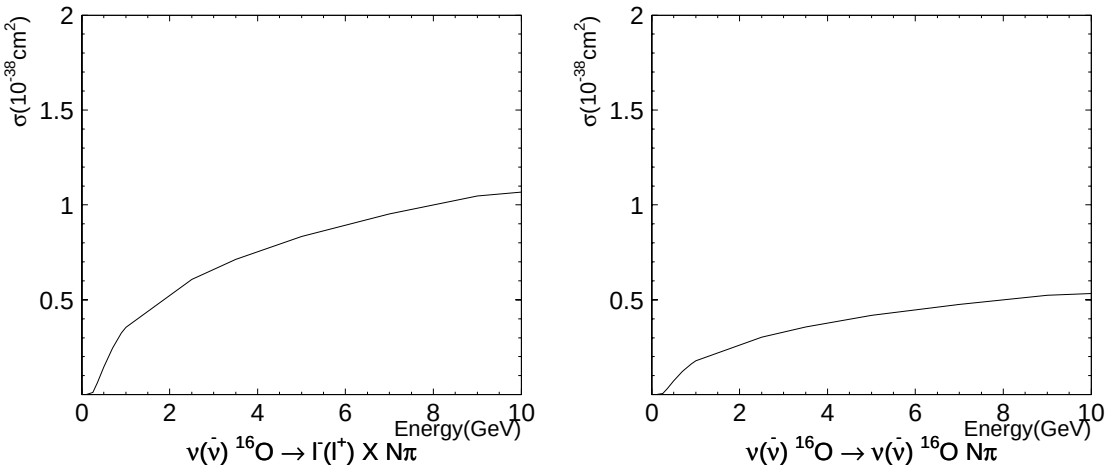

Figure 4.11: Cross-sections for CC and NC coherent pion production.

primary interaction ($\gamma + n \to \pi^- + p$)[46]. The results of each simulation compared with the $\gamma^{12}C \to \pi X$ data[47] as shown in Fig. 4.13. The agreement between the calculation and the expetimental data is good around the peak. Altough the agreement is not good in lower momentum region, the experimental data has large uncertainty. The systematic uncertainties for the Monte Carlo simulation are estimated by using these comparisons.

4.4 Detector simulation

Particle tracking

Produced secondary particles are traced by the GEANT program [40], which has been developed at CERN and commonly used in high-energy experiments. And particularly for hadronic interactions in water, we selected the CALOR program, which had been developed at CERN and was based on the nuclear cascade model[41]. This program reproduces pion interactions well even at the low energy region ($E_\pi \sim 1GeV$). However, in a few hundred MeV region, the agreement between the CALOR and experimental data is not good enough for our experiment[42]. Therefore the total cross section of the nuclear interaction in water below 500MeV/c is estimated from the results of π-^{12}C scattering[43] and π-p scattering[44] experiments. And to determine fraction of each nuclear interaction mode, we use the result of π-Al experiment[45].

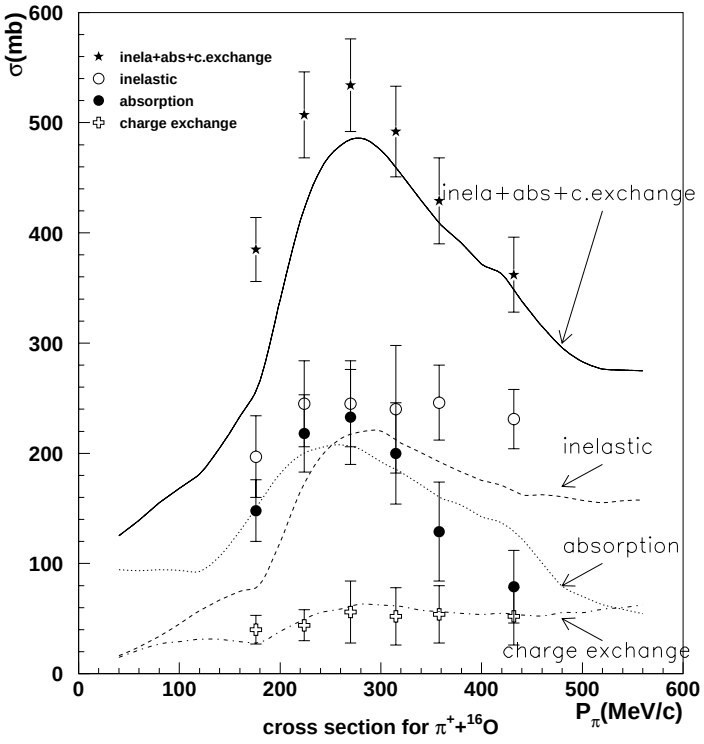

Figure 4.12: Calculated cross sections of the pion in a nucleus compared with the experimental data.

Cherenkov photon generation and PMT response

The number of emitted Cherenkov photons, the direction, and the wavelength of Cherenkov photons are calculated by Eq.2.2 and Eq.2.3. Each Cherenkov photon is traced until it hits a PMT or it is absorbed.

We consider the Rayleigh scattering, Mie scattering, and absorption of Cherenkov photons in water. Rayleigh scattering is the scattering with water molecules and the cross section is proportional to λ^{-4} (λ : wavelength). The Mie scattering treats scattering with a particle in the water and no wavelength dependence is assumed in our simulation. Fig. 3.10 shows the amount of these scatterings as a function of wavelength. Rayleigh scattering is dominant in the short wavelength region and absorption is dominant in the long wavelength region. In this figure, the total value and the wavelength dependence of the scattering and the absorption agree with the data measured by the laser system (Sec. 3.4).

When a photon hits a black sheet at the detector wall, its reflection or absorption is simulated by using the measured data. When a photon hits a PMT, the quantum efficiency of the PMT is considered as shown in Fig. 4.14. The response of the PMT is simulated by using measured timing and charge resolutions. And random noises are also added in each event in order to simulate real circumstances.

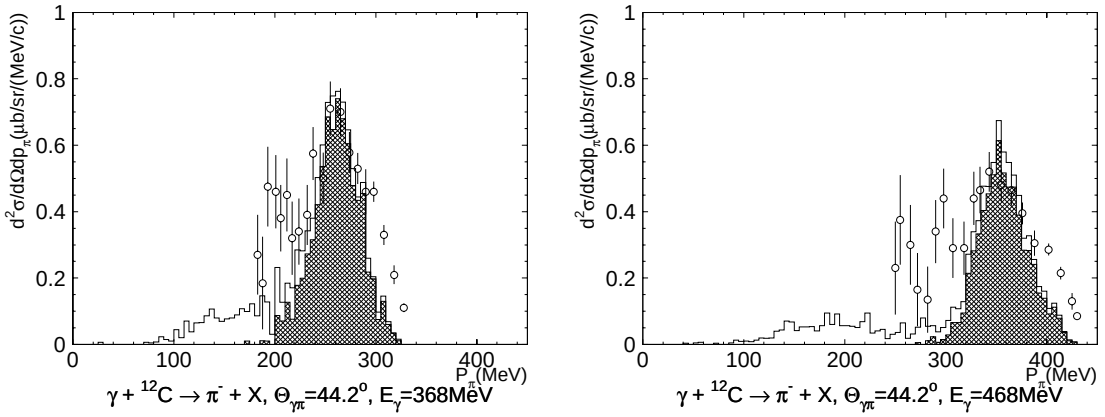

Figure 4.13: Differential cross section for the pion photo-production, $^{12}C(\gamma, \pi)$. Plots show the experimental data and histograms show the calculated cross sections. Hatched histograms show the rate of pions which go out of a nucleus without scattering in the nucleus.

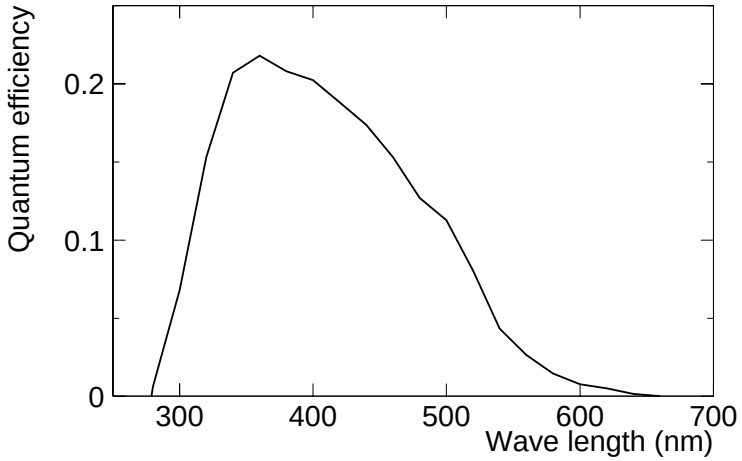

Figure 4.14: The quantum efficiency as a function of wavelength(nm).

4.5 Summary of Monte Carlo simulation

Number of events predicted by the Super-Kamiokande Monte Carlo for each interaction mode are given in Table 4.1. They correspond to 10 year observation. About 86% of sub-GeV events is from CC interactions, (quasi-) elastic interaction amounts to 57%, but for single-ring events, it increases to 75%. Since the (quasi-) elastic events are dominant in the sub-GeV sample and cross sections and kinematics of (quasi-) elastic interaction are much better known than pion productions, the sub-GeV single-ring sample is best suited for the atmospheric neutrino study.

	total	ν_e CC	ν_μ CC	NC
(quasi-) elastic	13810	5204	8480	126
single $\pi^\pm$	3633	1250	2133	250
single π^0	1623	203	440	980
multi π	3988	856	1649	1483
coherent π	1031	202	406	423
total	24085	7715	13108	3262

Table 4.1: Summary of the Monte Carlo simulation in sub-GeV energy region.

Chapter 5

Event selection

Super-Kamiokande started the observation on April 1, 1996. As shown in Fig. 3.12, the water attenuation length had been changed significantly for the first two months and became stable at the end of May 1996. Therefore we used the data sets from May 27, 1996 to June 25, 1997 in this analysis, which corresponded to 325.8 days of detector livetime. During this period about 300 million events were recorded.

Fig. 5.1 shows an outline of the event selection. The three software reduction algorithms reject background events so that the reduced data sets are manageable for scanning. After reduction all candidate events are hand-scanned doubly by physicists to reject remaining background events and check the data quality. The final scan is done to check the quality of the double scan. The final data set is fixed here and the total live time is calculated. For the Monte Carlo events, we apply the identical event selection processes.

In this chapter, the method of event selection is presented.

5.1 First reduction

About 1 million events are triggered and recorded every day. The data size is about 12Gbyte/day. The purpose of the first reduction is to reduce events quickly and make the output data easy to handle. Therefore simple criteria are adopted for the first reduction, which are:

1. The total number of photoelectrons(p.e.) with a 300nsec time window, PE_{300}, must be larger than 200p.e., which corresponds to 23MeV. This constraint rejects low energy backgrounds caused by radon or low-energy gamma-rays from the wall.

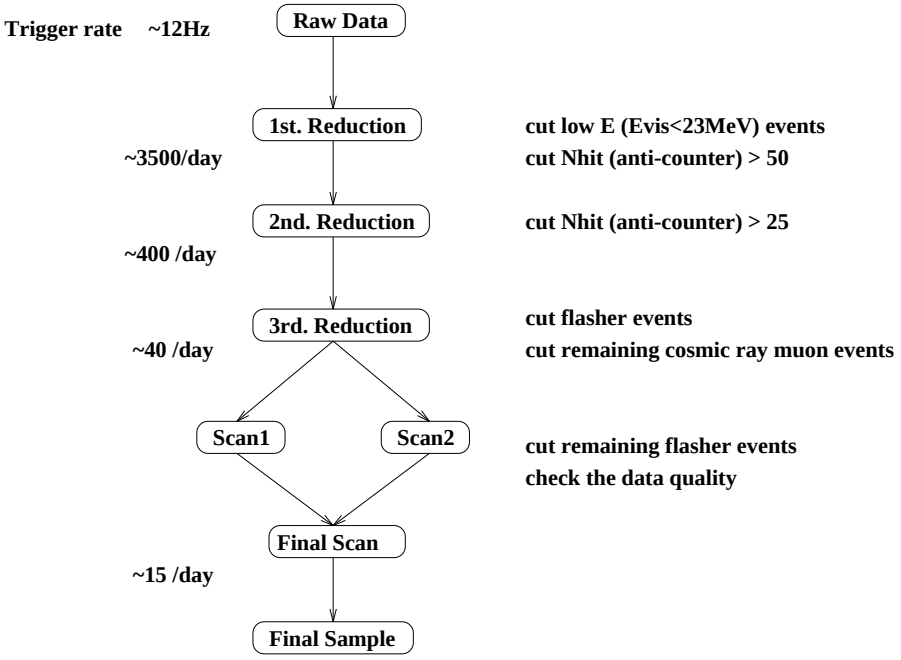

Figure 5.1: Algorithm of event selection for FC sample. The left numbers show event rates for one day.

2. The number of outer detector(OD) hits within an 800nsec time window must be less than 50. This constraint rejects cosmic-ray muon events(Fig. 5.2).

If an event does not satisfy both criteria, it is rejected. After the first reduction, the event rate is about 3500 events/day.

5.2 Second reduction

The data set which has survived the first reduction is applied to the second reduction. The criteria of the second reduction are:

1. PE_{MAX}(maximum number of p.e. in a PMT)/PE_{300} is less than 0.5. This cut rejects low-energy events with one large accidental hit.

2. OD-hits within an 800nsec time window must be less than 25, or OD-trigger is off.

Fig. 5.2 shows the PE_{MAX}/PE_{300} distribution. Referring to the right figure, which shows the Monte Carlo atmospheric neutrino events with vertex larger than 1.5m from the detector wall, we can see that almost all of PE_{MAX}/PE_{300} for the atmospheric neutrino events is less than 0.3. Thus the criterion, PE_{MAX}/PE_{300} <0.5, is safe for the fully-contained events. The second criterion is essentially the same as the first reduction. But

a tighter constraint is applied. The OD-hits distribution with an 800nsec time window is shown in Fig. 5.2. Since the OD-hits of the random trigger events are less than 20 hits, the second criterion is safe for the fully-contained events.

The event rate after the second reduction is about 400 events/day.

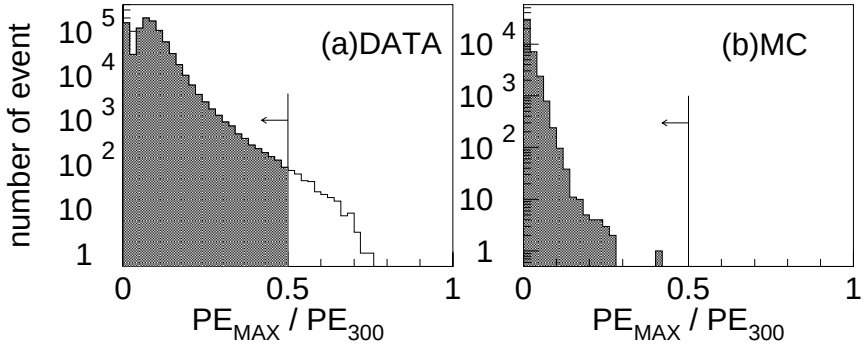

Figure 5.2: PE_{MAX}/PE_{300} distributions for (a)DATA after the first reduction and (b)atmospheric neutrino MC events with vertex more than 1.5m from the detector wall.

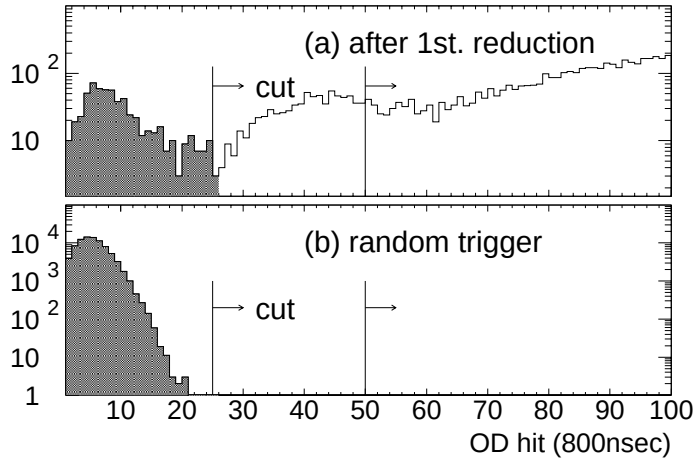

Figure 5.3: The OD-hits distribution for (a)DATA and (b)random trigger events.

5.3 Third reduction

By the previous two reductions, most of the backgrounds have been removed. Therefore it is possible to apply a more intelligent reduction algorithm. The third reduction consists of 6 parts, which are: a through-going muon cut, a stopping muon cut, a low-energy event

cut, a "flashing"PMT cut, a "cable-hole" muon cut, and an accidental event cut. The details of these cuts are presented below.

Through-going muon cut

A through-going muon event has two clusters in the OD-layer at the entrance and exit points. Inner PMTs at the entrance and exit points receive a large number of Cherenkov photons. If an event satisfies the following three criteria, it is identified as a through-going muon event and rejected.

1. The maximum number of p.e. in a PMT is more than 230 p.e.
2. The inner detector(ID)-hits are more than 1000.
3. The number of OD-cluster hits on the entrance or exit point of a particle, OD-hit$_{ent/exit}$, is more than 9, where the number of OD-cluster hits is defined as the number of OD-hits within an 800nsec time window within a radius of 8m from the entrance or exit point.

The entrance and exit points of a through-going muon are determined as the position of the earliest inner hit-PMT with more than two neighboring inner hit-PMTs and the center position of inner hit-PMTs whose charges are saturated, respectively. Fig. 5.3 shows the OD-hit$_{ent/exit}$ distribution for the random trigger events. There are no events with OD-hit$_{ent/exit}$ larger than 9 hits. Therefore this criterion is safe for the fully-contained events.

A typical through-going muon event rejected by this cut is shown in Fig. 5.3.

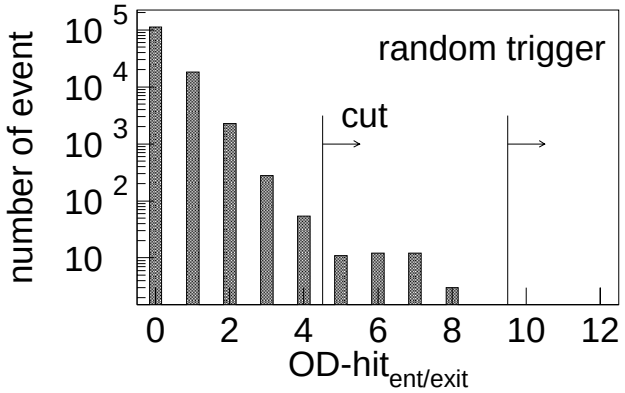

Figure 5.4: The OD-hit$_{ent/exit}$ distribution for the random trigger events.

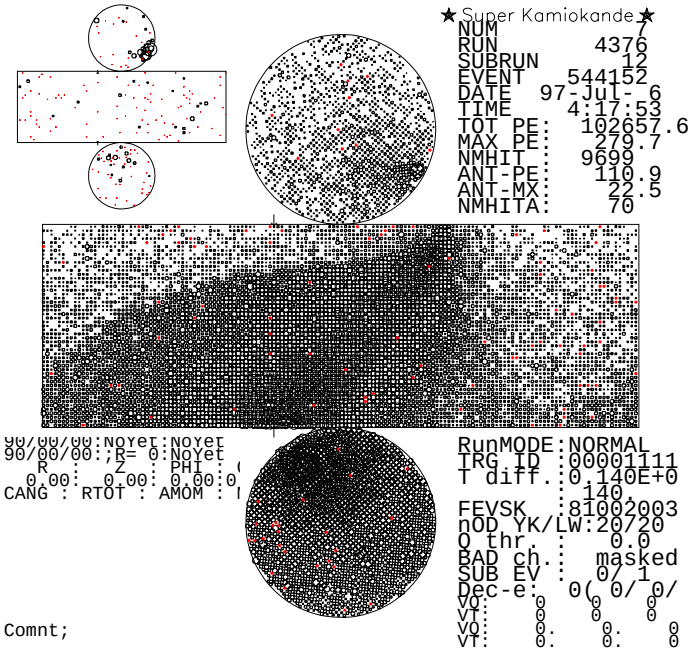

Figure 5.5: A typical through-going muon event rejected by the through-going muon cut. The small figure on the upper left side displays OD-hits. The maximum number of p.e. in a PMT is 279.7p.e. and the number of OD-cluster hits at the entrance is 17.

Stopping muon cut

The vertex of remaining events are reconstructed by the "stopping μ fitter", in which the vertex is determined by looking for the earliest hit PMT and the vertex must be on the detector wall. The direction of an event is adjusted by maximizing the total number of p.e. in the Cherenkov cone. An event which satisfies one of the following two conditions is rejected as a stopping muon event.

1. OD-hit$_{ent}$ is more than 9.

2. OD-hit$_{ent}$ is more than 4 and the *goodness* of the stopping μ fitter is more than 0.5. The definition of the *goodness* is the same as the TDC-fit (see Section 6.1).

By the second criterion, although the number of OD-cluster hits is not more than 9, the event is defined as a stopping muon if this event is fitted well by the stopping muon fitter. For the fully-contained atmospheric neutrino events we checked that the number of OD-cluster hits was at most 2. Since the number of events with OD-hit$_{ent/exit}$ larger than 4 hits are 38 in 10^5 events as shown in Fig. 5.3, this criterion safely rejected stopping-muon events.

A typical stopping muon event is shown in Fig. 5.6.

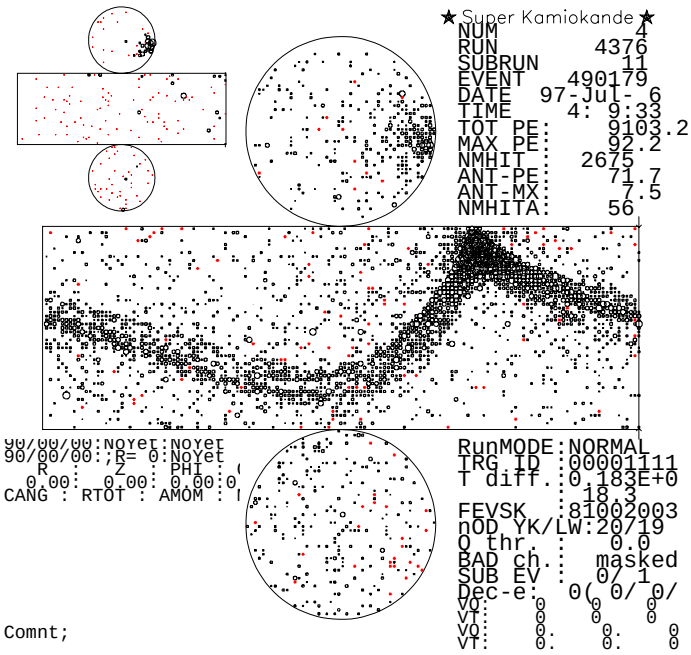

Figure 5.6: A typical stopping muon event rejected by the stopping muon cut. The number of OD-cluster hits at the entrance is 17 and the *goodness* is 0.71.

low-energy event cut

In order to reject the remaining low-energy events, we apply the low-energy fitter for all candidate events and calculate two parameters, "N_{50}" and "$goodness_{low}$". The low-energy fitter uses a grid search method to find the vertex which maximizes the $goodness_{low}$. The definition of the $goodness_{low}$ is the same as that of the point-fit(See Section 6.1).[1] N_{50} is calculated by sliding a 50nsec window through the time residual (time minus the flight time of Cherenkov photon). The maximum number of PMT hits in the 50nsec window is defined as N_{50}. For low-energy events N_{50} is a good energy indication, which is proportional to the particle energy. Five hits of N_{50} correspond to about 1MeV.

If an event satisfies one of the following two conditions, it is rejected as a low-energy event.

1. The number of ID-hits is less than 500 and N_{50} is less than 50($\sim$10MeV).
2. The number of ID-hits is less than 500 and the $goodness_{low}$ is less than 0.5. This criterion rejects events in which no Cherenkov ring is found.

The $goodness_{low}$ distribution for muon-decay electron events is shown in Fig. 5.7. Since there is only one event with $goodness_{low}$ less than 0.5 in 46000 events, this criterion is safe.

A typical low-energy event is shown in Fig. 5.8.

[1] For the low-energy fitter, the timing resolution, σ, is 5nsec and the $factor$ is 1.0 in Eq.6.2.

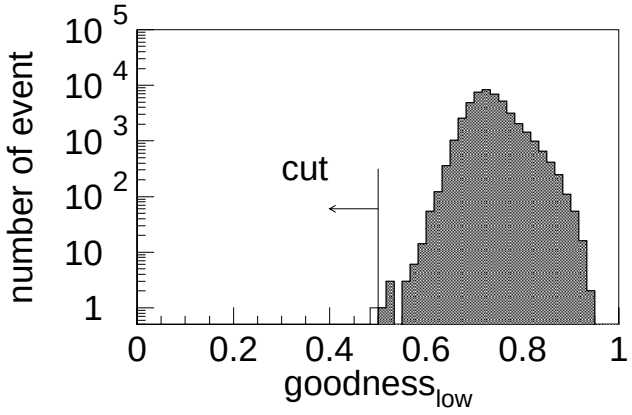

Figure 5.7: The $goodness_{low}$ distribution for muon-decay electron events.

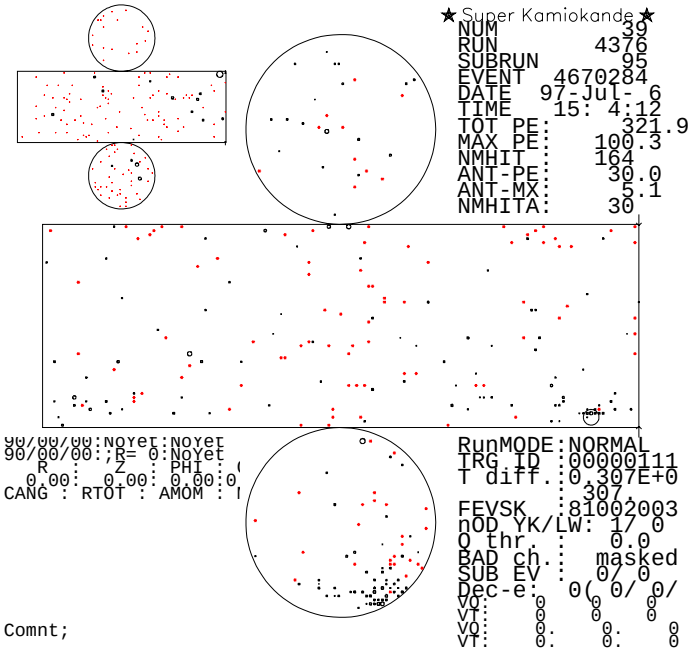

Figure 5.8: A typical low-energy event rejected by the low-energy event cut. The N_{50} of this event is 15 and $goodness_{low}$ is 0.52.

Flashing PMT cut

If a PMT has a mechanical problem in the dynode structure, the PMT emit light from internal corona discharge. These events are categorized as "flashing PMT" events. A feature of flashing PMT event is a broad time distribution as shown in Fig. 5.9. To remove such a flashing PMT event, we calculate the number of hits within a 100nsec time window. This window is slid from 1200nsec to 1800nsec (outside of the genuine signal region) and the minimum number of hits, N_{min}, is found. If an event satisfies one of the following two conditions, it is rejected as a flashing PMT event.

1. N_{min} is more than 14.

2. N_{min} is more than 9 and number of ID-hits is less than 800.

A typical flashing PMT event is shown in Fig. 5.10.

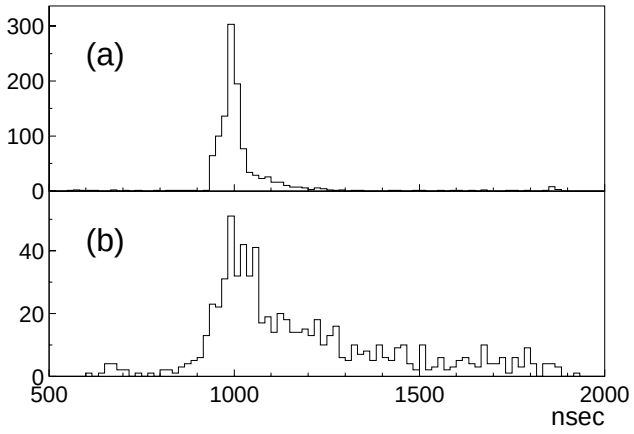

Figure 5.9: ID-time distributions for (a)a typical normal event and (b)a flashing PMT event. N_{min} of this flashing event is 21.

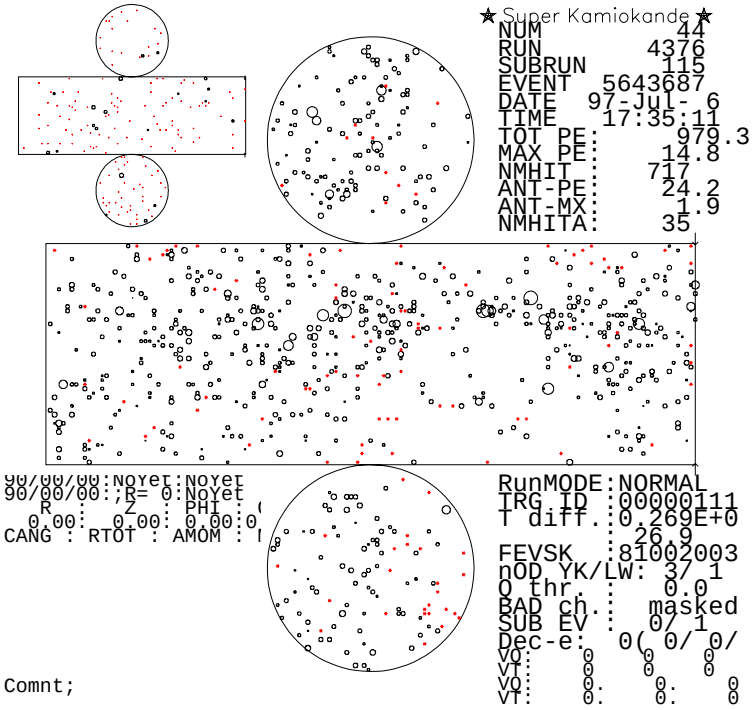

Figure 5.10: A typical flashing PMT event rejected by the flashing PMT cut.

Accidental hit cut

The accidental hit cut rejects an event which has more than two independent particles in an event accidentally. An event is rejected as accidental if both of the following two conditions are true.

1. The number of OD-hits with a time window between 1300nsec and 1800nsec is more than 19.

2. The total number of ID-p.e. with a time window between 1300nsec and 1800nsec is more than 5000p.e.

The OD-time distribution of a typical accidental hit event is shown in Fig. 5.11.

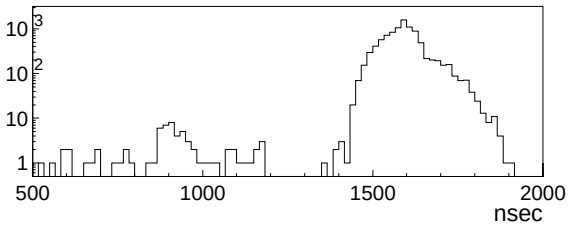

Figure 5.11: OD-time distribution of an accidental hit event rejected by the accidental hit cut. This event was triggered by a low-energy event and a cosmic-ray muon about 600nsec later.

Cable-hole muon cut

Cables from ID and OD PMTs are bundled in the upper OD-layer and are taken out of the tank through the 12 cable-holes. 4 of the 12 cable-holes are located away from the fringe of the tank, and the identification efficiency of the OD is low for muons passing near these 4 cable-holes. In order to compensate for the inefficiency of OD around the four cable-holes, we installed $2.0m \times 2.5m$ veto-scintillation counters on each of the four cable-holes in April, 1997. An event, in which one of the veto-scintillation counters is hit and a vertex is reconstructed within 4m from the cable-hole by the stopping μ fitter, is identified as a cosmic-ray muon and rejected even if there are few OD-hits. A typical muon event rejected by this cut is shown in Fig. 5.12.

5.4 Scanning

After the three software reduction steps, the candidate events are reduced to 13451 events, it is about 40 events/day. But there are still remaining cosmic-ray muon events and flashing PMT events. Therefore the candidate events are scanned twice by independent scanners to reject these remaining background events. At the same time the scanners check the data quality. When the detector performance is not good, for instance too many flashing events or some of the PMTs are not active, these runs(subruns) are regarded as bad-runs(bad-subruns) and are rejected. After the double scan, the final

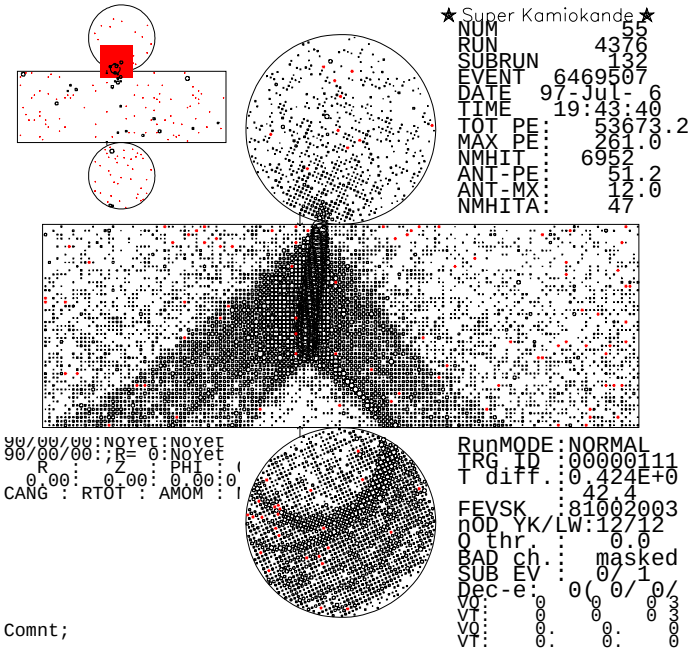

Figure 5.12: A cable-hole muon event rejected by the cable-hole muon cut. A square mark on the OD display shows a hit of the veto-scintillation counter.

scan is done to check the consistency of the double scan result and make the final fully-contained data sample. Finally, 5033 candidate events are selected as the final data sample.

We also did the double scan for a part of the event sample just after the second reduction in order to check performance of the third reduction and about 1000 fully-contained events were collected. Since all of these events were passed the third reduction. we estimate the probability that the event selection processes reject fully-contained events to be less than 0.1%. Contamination from flashing PMT and cosmic-ray muon events are also negligible in the sample of fully-contained events in the fiducial volume. These effects are estimated in section 7.2.

Livetime

After removing bad runs by the final scan, we calculate the total livetime. Livetime is defined as the time when the electronics are enabled for trigger. It does not include the pedestal data-taking time and the electronics dead time. From May 27, 1996 to June 25, 1997, the total data-taking time was 345.5 days. During this period total bad-run(subrun) time was 9.9 days and total electronics dead time was 9.8 days (it includes pedestal data-taking time.) The livetime is calculated to be 325.8 days.

Chapter 6

Analysis

After the event selection processes, events were reconstructed by the following four procedures.

TDC-fit

⇓

Ring counting

⇓

Particle identification (PID)

⇓

MS-fit

These procedures are fully automatic. Therefore there is no bias by a scanner or physicist in the event reconstruction steps.

At first, the vertex, direction, Cherenkov opening angle and momentum are reconstructed for the most energetic particle in an event using a routine called "TDC-fit", which uses timing information of hit PMTs. Once the vertex is determined, "Ring counting" process tries to find another Cherenkov ring and judges whether its event is single-ring or multi-ring. The particle identification process classifies a ring as "e-like" or "μ-like" by the hit-pattern and opening angle of the Cherenkov ring. Using information of the particle type, "MS-fit" further improves the vertex, direction, and momentum for single-ring events.

6.1 TDC-fit

The TDC-fit consists of the following three parts. (1)The "point-fit" finds a rough vertex by using the timing information of the PMTs which caught Cherenkov photons. (2)The

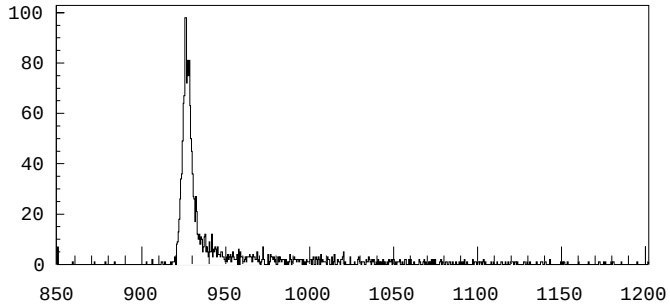

Figure 6.1: The timing residual, t_i(nsec.), distribution in a typical event.

edge of Cherenkov ring is determined by using the charge information from hit PMTs. (3)Determine the vertex again. Here, the particle track length and scatter photons are taken into account to obtain a better vertex resolution.

In following sub-sections, I will describe details of these 3 steps.

Point-fit

The principle of the vertex reconstruction is to find out the position where the timing residuals, t_i, of all hit PMTs are equal. The timing residual, t_i, of the i-th hit PMT is defined as;

$$t_i = t_i^0 - \frac{1}{v_c(q, l_c)} \times \sqrt{(x - x_i)^2 + (y - y_i)^2 + (z - z_i)^2} \tag{6.1}$$

where

$$\begin{aligned} t_i^0 &: \text{hit time of the i} - \text{th PMT} \\ c &: \text{light velocity} \\ (x_i, y_i, z_i) &: \text{position of the i} - \text{th PMT} \\ (x, y, z) &: \text{vertex position.} \\ v_c(q, l_c) &: \text{light velocity in water.} \end{aligned}$$

Since the refractive index of water, n, is a function of wave length, v_c depends on the charge detected by PMT, q, and flight length of Cherenkov photons, l_c.

If the point (x, y, z) gives the correct vertex position, the timing residuals should look like Fig. 6.1. On the other hand, if the point (x, y, z) is not correct, the width of the peak is broader. The finite width in Fig. 6.1 is due to the timing resolution of PMTs. A long tail in the histogram is due to scattered Cherenkov photons in water or photons reflected at the detector wall.

We use a *goodness*, G, to evaluate the accuracy of the vertex reconstruction. The *goodness* for the point-fit, G_P, is defined as:

$$G_P = \frac{1}{N_{hit}} \sum_i \exp\left(-\frac{(t_i - \langle t \rangle)^2}{2(\sigma \cdot factor)^2}\right) \tag{6.2}$$

$$\text{with } factor = 1.5,$$

where N_{hit} is the number of hit PMTs and σ is the typical timing resolution. In the point-fit program, σ is taken to be 2.5nsec. The contribution from the scattered light is made small with an effective cut-off of $\sim 3\sigma$ represented by the $factor = 1.5$. In this way, dark pulses from PMTs and scattered lights are largely removed from the vertex reconstruction process.

The point, where the G_P takes maximum is regarded as the vertex position.

Cherenkov edge search

To find out the edge of a Cherenkov ring, we define three parameters "PE(θ)", "θ_{edge}" and "Q". The PE(θ) is the effective total p.e. as a function of the opening angle which is an angle between particle direction and Cherenkov photon direction. PE(θ) is smoothed to reduce the statistical fluctuation, as shown in Fig. 6.2(a). Next, θ_{edge} is the opening angle spanning the Cherenkov edge, which is determined by the following two conditions: (1)θ_{edge} must be larger than the angle at the peak of PE(θ), θ_{peak}, and (2)θ_{edge} is the angle nearest to θ_{peak}, where the second derivative, $\frac{d^2\mathrm{PE}}{d\theta^2}$, is 0 (See Fig. 6.2(b)).

Under these conditions, θ_{edge} is obtained by optimizing the following evaluation function, "Q".

$$Q = \frac{\int_0^{\theta_{edge}} \mathrm{PE}(\theta) d\theta}{\sin\theta_{edge}} \times \exp\left(-\frac{(\theta_{edge} - \theta_C)^2}{\sigma^2}\right), \tag{6.3}$$

where θ_C and σ are the Cherenkov opening angle and its resolution, respectively.

The optimization is carried out by changing the particle direction. The particle direction and θ_{edge} where Q takes a maximum value are adopted as the final ones. The edge of the Cherenkov ring is then calculated by using these final direction and θ_{edge}.

TDC-fit

After the Cherenkov edge has been found, we determine the vertex more precisely by considering scattered Cherenkov photons and the particle track length.

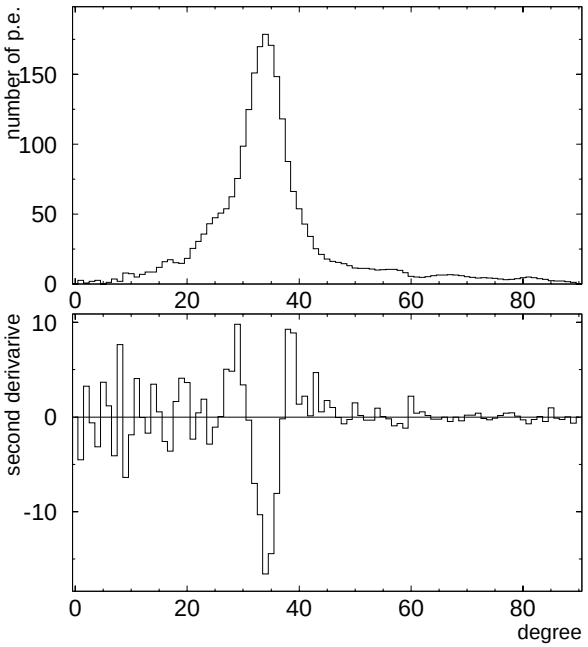

Figure 6.2: (a)A typical PE(θ) distribution for an e-like event and (b) $\frac{d^2\mathrm{PE}}{d\theta^2}$ distribution as a function of opening angle.

The *goodness* is redefined in the following way.
For the PMTs inside the Cherenkov cone, or the outer PMTs with $t_i \leq \langle t \rangle$ (mean of t_i)

$$G_I = \sum_i \frac{1}{\sigma_i^2} \exp\left(-\frac{(t_i - \langle t \rangle)^2}{2(\langle \sigma \rangle \cdot factor)^2}\right) \tag{6.4}$$

with $factor = 1.5$,

where σ_i is the timing resolution of the i-th PMT which is a function of its charge, $\langle \sigma \rangle$ is the average of σ_i.

On the other hand, PMTs outside the Cherenkov cone with $t_i > \langle t \rangle$ are regarded as scattered light. For PMTs outside the Cherenkov cone with $t_i > \langle t \rangle$,

$$G_O = \sum_i \frac{1}{\sigma_i^2} \max\left[\exp\left(-\frac{(t_i - \langle t \rangle)^2}{2(\langle \sigma \rangle \cdot factor)^2}\right),\ 0.8 \times \exp\left(-\frac{(t_i - \langle t \rangle)}{(20nsec)}\right)\right], \tag{6.5}$$

where 20nsec is the mean time from direct Cherenkov photons to the scattered photons estimated from the Monte Carlo simulation.

Finally, G is defined as;

$$G = [G_I + G_O] / \sum_i \frac{1}{\sigma_i^2}, \tag{6.6}$$

where $\sum_i \frac{1}{\sigma_i^2}$ normalizes the range of G from 0 to 1.

Next, we consider the finite track length of a particle and the corrected vertex is found by the following three procedures. (1) Estimate the total track length, L_t, from the total number of p.e. within a cone of 70° half opening angle. (2) Re-calculate the

residual time, t_i, which takes into account the particle velocity and position along the track where Cherenkov photon is emitted. (3) Calculate *goodness*, G, using modified t_i. Iterate these procedures and the final vertex position, direction, and momentum are adopted where the *goodness* takes the maximum value. The performance of the TDC-fit will be discussed in Sec. 6.4.

6.2 Ring counting

After the vertex, direction and Cherenkov opening angle of the most energetic Cherenkov ring have been reconstructed, we try to find the second Cherenkov ring and judge whether the event is a single- or multi-ring event. The algorithm, which counts the number of rings, consists of the following two steps: (1)search for the second Cherenkov ring candidates, (2)check whether the second Cherenkov ring candidates are true Cherenkov ring or not.

In the following sections a brief description of the two steps and their performance are presented. Further discussion is presented in Ref.[48].

Search for the second Cherenkov ring

The direction of the second Cherenkov ring is searched for by using the "charge map". The charge map is a 2-dimensional array with directions of 72 azimuth angle (θ) and 36 polar angle (ϕ), angles being measured from the vertex. Fig. 6.3 shows a basic concept of the ring counting algorithm. First, the expected number of p.e. from the first Cherenkov ring is subtracted from the number of p.e. of each hit PMT. For the i-th bin in the array (θ_i, ϕ_i), the total number of p.e. is filled which corresponds to the sum from all the PMTs that happen to lie on a circle of 42 deg. [1] from the direction (θ_i, ϕ_i). If the second Cherenkov ring really exists, the bin corresponding to the true direction of the second ring has the largest number of p.e. all of the other bins. An opening angle between the direction of the first and the second Cherenkov ring must be more than 15 degree in order to keep the ring-finding algorithm effective.

Number of ring determination

We use the maximum likelihood method to determine whether the second candidate ring is true or false. The likelihood for the single-ring of double-ring is calculated from

[1] the angle, 42 deg., is adjusted to get more suitable Cherenkov opening angle in the algorithm.

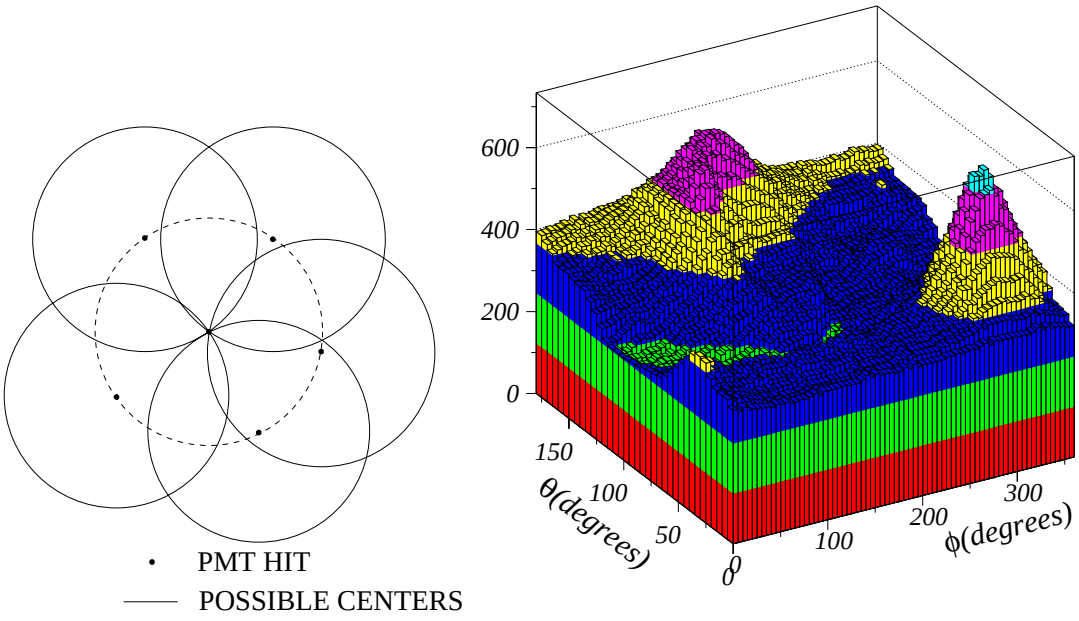

Figure 6.3: Left figure shows PMT hits and possible centers estimated by the direction of PMT hits. By accumulating all the possible centers for every PMT, we can find the most probable circle center as a focus of these circles. Right figure shows the charge map(θ, ϕ) for a typical two ring event. Two peaks correspond to the respective directions.

the expected number of p.e. from the corresponding number of rings. These likelihood functions are calculated with weights from the opening angle and overlap area between the two rings because it becomes incleasingly difficult to identify the second ring if the two rings are piled up. If the likelihood for the single ring is larger than the two-ring likelihood, this event is identified as a single ring.

If an event is identified as two rings, the third ring is searched for and is examined by the similar likelihood functions. In the same way, we can count the number of rings up to 5 rings.

Performance of Ring counting

We check the performance of the ring counting program with Monte Carlo charged current (CC) quasi-elastic (q.e.) events with visible energies less than 1.33GeV, since CC quasi-elastic interaction generates only one lepton and should be identified as a single-ring event. The efficiency is defined as (number of identified single-ring q.e. events) / (number of q.e. events). Fig. 6.4 shows the efficiency as a function of visible energy.

95% of q.e. events are correctly identified as single-ring event, and there is almost no energy dependence

Fig. 6.5 shows the efficiency as a function of the dwall, which is the distance between the vertex and the nearest detector wall. The efficiency of the single-ring selection does not have any strong vertex dependence.

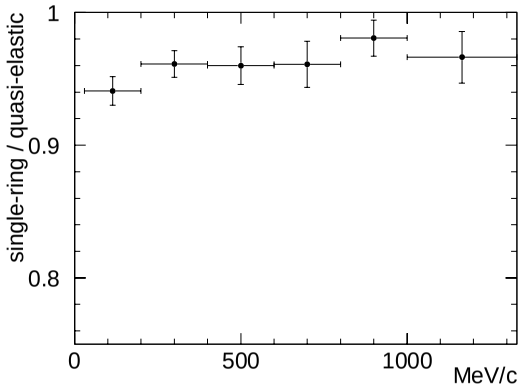

Figure 6.4: The (number of identified single-ring q.e. events) / (number of q.e. events) ratio as a function of momentum, estimated using the MC events generated in the fiducial volume (vertex 2m inside the inner detector wall).

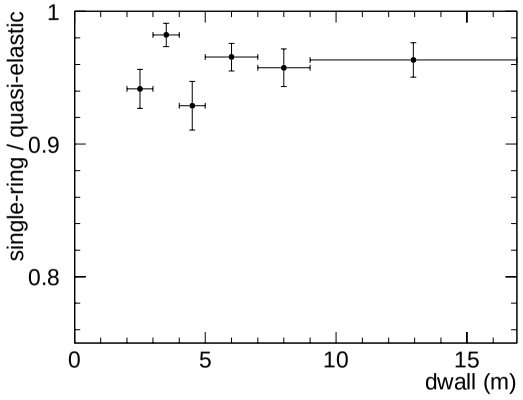

Figure 6.5: The (number of identified single-ring q.e. events) / (number of q.e. events) ratio as a function of dwall, estimated using the MC events generated in the fiducial volume.

6.3 Particle Identification

6.3.1 The Method of Particle Identification

The particle identification (PID) algorithm makes use of the pattern and opening angle of the Cherenkov ring. Electrons produce electromagnetic showers and low-energy electrons in particular exhibit many multiple scatterings and produce rather diffuse Cherenkov rings, while muons produce sharp Cherenkov edges. For low momentum particles, infor-

mation of the opening angle, θ_C, is important because the $\cos\theta_C$ is proportional to the $(n\beta)^{-1}$ (see Sec. 2.1).

The PID algorithm starts with expected p.e. calculation.

The Expected Direct p.e. for e-like Events.

Monte Carlo simulation with perfect water transparency is made in order to make a table, for electrons, of the average number of photoelectrons ,$N_{MC}(\theta, p_e)$, received in a circular area of 50cm diameter (equal to PMT photosensitive area) located on a sphere of 16.9m in radius. θ is an angle between the circular area and the particle direction, and p_e is the electron momentum. Since Cherenkov photons are emitted in a cone, we average the number of photoelectrons as a function of the opening angle, θ, and derive $N_{MC}(\theta, p_e)$. They are tabulated in a two-dimensional form $N_{MC}(\theta_j, p_{ej})$, where $\theta_j = 0°, 1°, 2°, \cdots, 90°$ and p_{ej} =100MeV/c, 300MeV/c, 1000MeV/c. If necessary, interpolation is performed to obtain $N_{MC}(\theta, p_e)$ for desired θ and p_e.

The expected number of p.e. in the i-th PMT produced by an electron is expressed as;

$$N_{i.exp}(direct) = \alpha_e \times N_{MC}(\theta_i, p_e) \times (\frac{16.9\mathrm{m}}{l_i})^{1.5} \times \exp(-\frac{l_i}{L}) \times f(\Theta), \qquad (6.7)$$

where α_e is the normalization factor, l_i is the distance from the particle position to the i-th PMT, θ_i is the angle of the i-th PMT from the particle direction, and L is the light attenuation length. $f(\Theta)$ is the effective photo-sensitive area of the PMT as shown in Fig. 3.2. The third term in the right-hand side of Eq. 6.7 shows the diffusion of light and its power index is estimated by the Monte Carlo simulation.

The Expected Direct p.e. for μ-like Events

The expected number of p.e. in the i-th PMT produced by a muon is expressed as;

$$N_{i,exp}(direct) = \{\alpha_\mu \times \frac{1}{l_i(\sin\theta_i + l_i \cdot (\frac{d\theta}{dx}))} \times \sin^2\theta_i + N_{i,knock}(\theta_i)\} \times \exp(-\frac{l_i}{L}) \times f(\Theta) \quad (6.8)$$

where α_μ is the normalization factor. The second term in the right-hand side originates from the ionization energy loss $\frac{dE}{dx}$ in water. As shown in Fig. 6.6, $dxsin\theta + ld\theta$ takes into account the change in the photon density which is caused by the change in θ, corresponding to the energy loss. $\sin^2\theta_i$ expresses the intensity variation of Cherenkov photons (see Eq. 2.3). $N_{i,knock}(\theta_i)$ shows the number of expected photons from knock-on electrons as a function of θ_i, which is estimated by a Monte Carlo simulation.

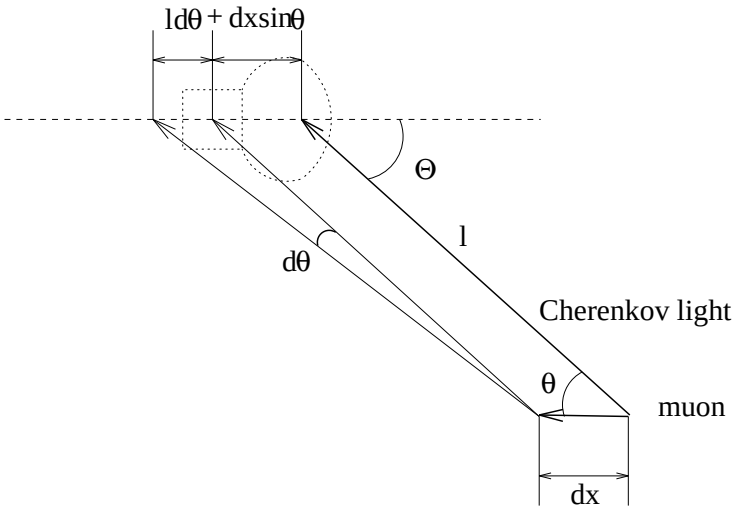

Figure 6.6: Relation between the PMT and Cherenkov photon.

Treatment of Scattered Lights

Scattered photons can be separated from the direct Cherenkov photons by checking the arrival time. We first pick up hit PMTs within a cone having an opening angle of $1.5 \times \theta_C$, where θ_C is the reconstructed Cherenkov opening angle. This aims to eliminate accidental hits which lie mostly outside the Cherenkov cone. Then a histogram of timing residuals, t_i, is made for all the selected PMTs. Scattered photons are selected with the following criterion;

$$\begin{aligned} t_{peak} - 30\text{nsec} < t_i \leq t_{peak} + 2\sigma(p.e._i) + 5\text{nsec} \quad &\longrightarrow \quad \text{direct photons}, \\ t_{peak} + 2\sigma(p.e._i) + 5\text{nsec} < t_i \quad &\longrightarrow \quad \text{scattered photons}, \end{aligned} \tag{6.9}$$

where t_{peak} is the peak in the timing histogram and $\sigma(p.e._i)$ is the timing resolution of the i-th PMT as a function of the detected number of p.e. The number of p.e. originating from the scattered photons, $N_{i.exp}(scatter)$ is calculated from Eq.6.9. Thus the expected number of p.e. for the i-th PMT is given by adding both contributions:

$$N_{i.exp} = N_{i.exp}(direct) + N_{i.exp}(scatter). \tag{6.10}$$

Estimator of Particle Identification

We now define the probability, $Prob(N_{exp}, N_{obs})$, suitable for the particle ID. It is the probability to observe the number of p.e., N_{obs}, for an expected mean number of p.e., N_{exp}. The N_{obs} actually deviates from the ideal Poisson distribution due to fluctuations in amplification processes of the PMTs. Therefore, if N_{exp} is less than 20p.e., the probability function is derived from the composition of single-photoelectron distribution. For

N_{exp} >20 p.e., the probability function is simply given by:

$$Prob = \frac{1}{\sqrt{2\pi}\sigma} \exp(-\frac{(N_{obs} - N_{exp})^2}{2\sigma^2}), \tag{6.11}$$

with $\sigma^2 = 1.2^2 \times N_{exp} + (0.1 \times N_{exp})^2$,
where the factor 1.2 in σ comes from the actual PMT charge resolution and the second factor in σ takes into account the gain uncertainty in the PMT.

The probability function for the i-th PMT $Prob_i$ is expressed in two different ways, according to whether the PMT is hit by a direct photon or a scattered photon:
For a direct photon,

$$Prob_i = Prob(N_{i,exp}, N_{i,data})$$

For a scattered photon,

$$Prob_i = Prob(N_{i,exp}(direct), 0) \times Prob(N_{i,exp}(scatt), N_{i,data})$$

Selecting the PMTs inside a cone with an opening angle of $1.5 \times \theta_C$ from the reconstructed particle direction, the following likelihood function is defined for e-like or μ-like events;

$$L_e = \prod_{\theta_i < (1.5 \times \theta_C)} Prob_i(e),$$

$$L_\mu = \prod_{\theta_i < (1.5 \times \theta_C)} Prob_i(\mu), \tag{6.12}$$

where $Prob_i(e)$ is calculated assuming the event is due to electron, and $Prob_i(\mu)$ due to muon.

In order to combine the information of the Cherenkov opening angle with the information of the ring pattern, L_e and L_μ are transformed into the χ^2 distributions:

$$\chi^2(e \text{ or } \mu) = \frac{1}{\log_{10} e} \times \{-\log_{10} L_{e(\mu)}\} - constant. \tag{6.13}$$

If the degree of freedom N_D exceeds 30, which is normally the case, the sigma of the χ^2 distribution, σ_{χ^2}, is approximated as:

$$\sigma_{\chi^2} = \sqrt{2N_D}.$$

In this case, the N_D is the number of PMTs within the $\theta_C \times 1.5$. Then the probabilities by using Cherenkov pattern can be described as:

$$P_{pattern}(e) = \exp\{-\frac{1}{2}(\frac{\chi^2(e) - \min[\chi^2(e), \chi^2(\mu)]}{\sigma_{\chi^2}})^2\}. \tag{6.14}$$

$$P_{pattern}(\mu) = \exp\{-\frac{1}{2}(\frac{\chi^2(\mu) - \min[\chi^2(e), \chi^2(\mu)]}{\sigma_{\chi^2}})^2\}.$$

Next, the Cherenkov angle will be considered. From the reconstructed momentum we can calculate the expected Cherenkov opening angle, θ_{exp}. If the reconstructed Cherenkov opening angle is given as $\theta_{obs} \pm \Delta\theta$, the probability is derived as:

$$P_{angle}(e) = constant \times \exp\{-\frac{1}{2}(\frac{\theta_{exp}(e) - \theta_{obs}}{\Delta\theta})^2\} \tag{6.15}$$

$$P_{angle}(\mu) = constant \times \exp\{-\frac{1}{2}(\frac{\theta_{exp}(\mu) - \theta_{obs}}{\Delta\theta})^2\}$$

Combining Eq.6.14 with 6.15, the probability P is finally:

$$P(e) = P_{pattern}(e) \times P_{angle}(e), \tag{6.16}$$

$$P(\mu) = P_{pattern}(\mu) \times P_{angle}(\mu).$$

A ring is more μ-like than e-like, if $P(\mu) > P(e)$, and vice versa.

6.3.2 PID Performance

The PID performance is checked by (i)Monte Carlo atmospheric neutrino events and (ii)Cosmic-ray stopping muon and muon-decay electron events.

(i)Atmospheric neutrino events

In order to demonstrate the performance of PID, we defined the PID parameter as:

$$\text{PIDparameter} = constant \times (\sqrt{-\log P(\mu)} - \sqrt{-\log P(e)}).$$

If the PID parameter is positive(negative), this event is identified as e-like(μ-like) events. Fig. 6.7 shows the PID parameter distribution for sub-GeV single-ring events for the data and the Monte Carlo events. ν_e events are clearly separated from ν_μ events and the shape of the Monte Carlo PID parameter distribution reproduces the real data well. The misidentification probability for CC ν_e-induced event is 0.5±0.1% and for ν_μ-induced event is 1.0±0.1%. Combining these two misidentification probabilities, the average misidentification probability for sub-GeV atmospheric neutrino events is estimated to be 0.8±0.1%.

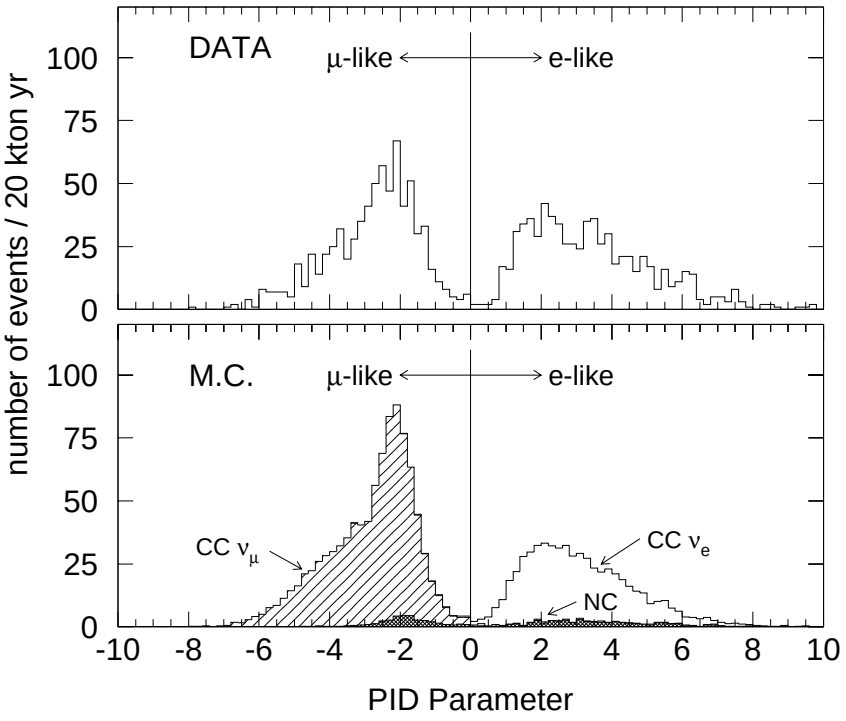

Figure 6.7: Distribution of the particle PID parameter for single-ring atmospheric neutrino events for both data and Monte Carlo samples. If the PID parameter of an event is positive(negative) the event is classified as e-like(μ-like).

(ii)Cosmic-ray stopping muon and muon-decay electron events

We check the stability of the PID performance by using cosmic-ray muons which stopped in the detector and also muon-decay electron events. Fig. 6.8 shows the result for these events together with the corresponding Monte Carlo estimation. The PID parameter distribution agrees well with the Monte Carlo estimation. The misidentification probabilities are $0.4 \pm 0.1\%$ and $1.8 \pm 0.5\%$ for muons and electrons, respectively. For the Monte Carlo events, misidentification probability of μ-like and e-like events are $0.1^{+0.3}_{-0.1}\%$ and 4.4±1.0%, respectively. Since the energy of muon-decay electrons is lower than electrons produced by the atmospheric neutrinos, the misidentification probability is a little worse. On the other hand, the misidentification probability for cosmic-ray muons is better than muons produced by the atmospheric neutrinos, because their energies are higher than sub-GeV atmospheric neutrino events. The PID performance has been continuously

checked and indeed found to be stable.

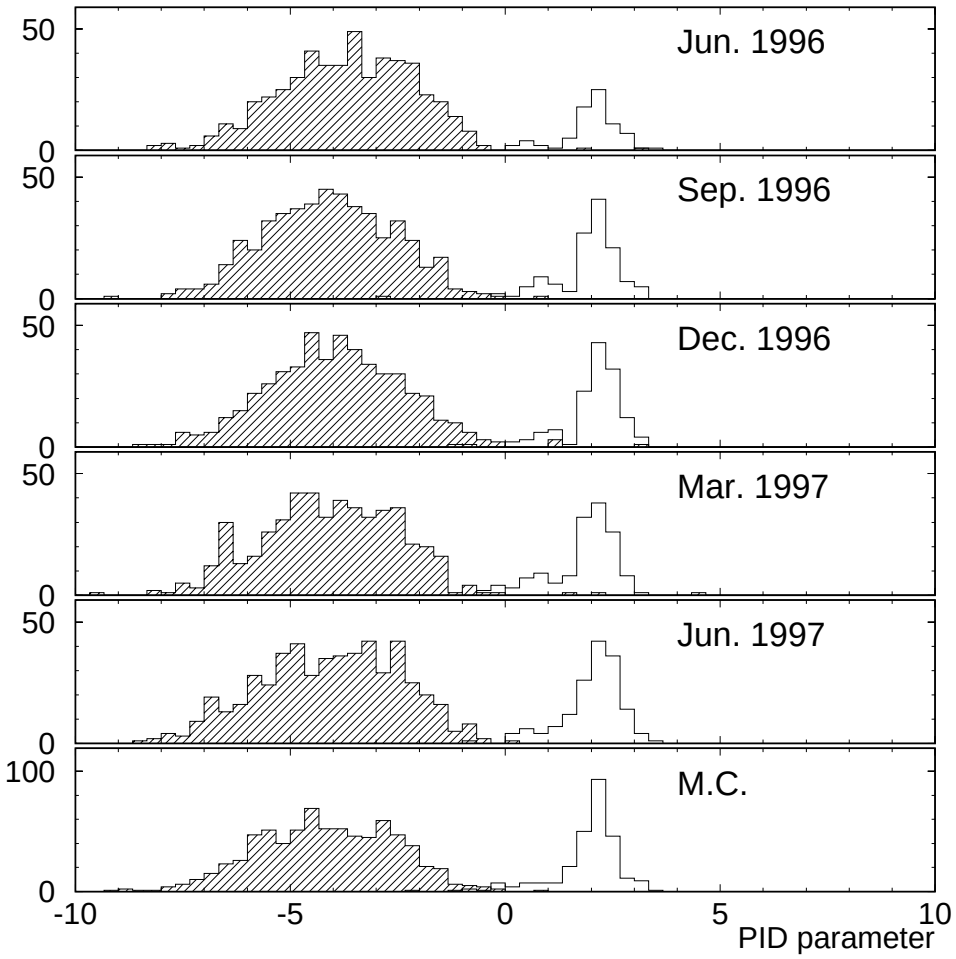

Figure 6.8: PID parameter for cosmic-ray muons (shaded histograms) and muon-decay electrons (open histograms). The lowest figure shows the Monte Carlo estimation.

6.4 MS-fit

The performance of the TDC-fit is good enough for the ring counting and particle identification, but the vertex resolution for the longitudinal direction has to be improved. It is because the TDC-fit uses mainly timing information of hit PMTs.

MS-fit is a vertex and direction reconstruction algorithm which uses the information of Cherenkov ring pattern like the PID method to improve the longitudinal vertex resolution.

6.4.1 Fitting method

The MS-fit finds the best vertex and direction by adjusting both the vertex position and direction from initial values given by TDC-fit. MS-fit uses the fixed Cherenkov opening angle, θ_C, which is calculated under the assumption of particle type. Then the expected photoelectron numbers for each PMT is estimated.

The algorithm of the MS-fit consists of three steps.

1. Iterate the vertex position perpendicular to the particle direction and find the position where the *goodness* takes the maximum value. Definition of the *goodness* is the same as used in the TDC-fit.

2. Iterate the vertex position parallel to the particle direction and find the position where the likelihood (L_e or L_μ) takes the maximum value. This likelihood is the same as used in the PID except the opening angle, θ_{obs}. The likelihood in the MS-fit uses θ_C instead of θ_{obs}.

3. Adjust the direction where the likelihood (L_e or L_μ) takes maximum.

The MS-fit iterates the above these three steps several times to get the best fit vertex position and direction.

6.4.2 Performance of MS-fit

The performance of the MS-fit is estimated by using the Monte Carlo sub-GeV single-ring events. Fig. 6.9 shows the Δpos distribution for the e-like and μ-like events, where the Δpos is the distance between the fitted vertex and original particle position. Defining the vertex position resolution as the distance where the 68% of events are found within Δpos, the resolution for the e-like events is 34cm and the resolution for the μ-like events is 25cm.

For the angular resolution, Fig. 6.10 shows the Δdir distribution. The Δdir is the angle between the fitted and true particle directions. The resolution (68% level) is estimated to be 3.2° for the e-like events and 1.9° for the μ-like events.

Next, we check the vertex position resolution along the particle direction. Fig. 6.11 shows the $\Delta pos_{//}$ distribution for the e-like and the μ-like events, compared with the result of the TDC-fit. $\Delta pos_{//}$ is defined as the projection of the Δpos along the particle direction. It is clear that the resolution of the MS-fit is significantly improved. Also the MS-fit has reduced systematic shift from $\Delta pos_{//} = 0$, though there still remains a small

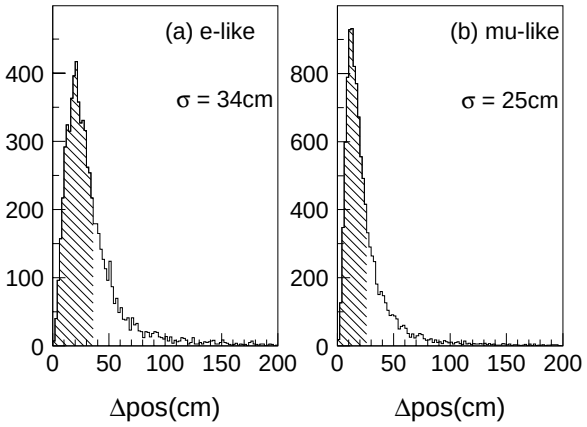

Figure 6.9: The Δpos distribution for (a)e-like and (b)μ-like sub-GeV single-ring events, estimated from MC events in the fiducial volume. Δpos is the distance between the vertex reconstructed by MS-fit and true vertex. The hatched area corresponds to 68% of the total events.

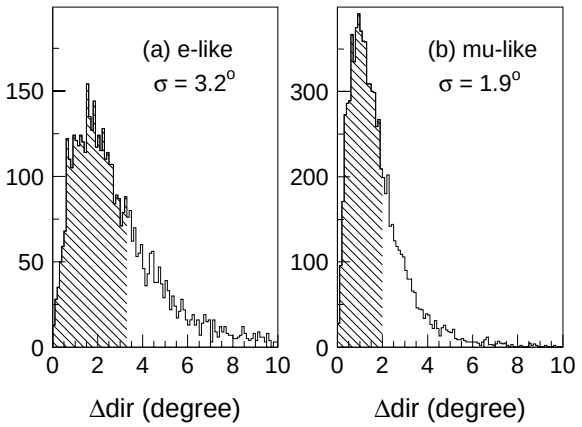

Figure 6.10: The Δdir distribution for (a)e-like and (b)μ-like sub-GeV single-ring events, estimated from MC events in the fiducial volume. Δpos is the opening angle between the reconstructed direction and true direction. The hatched area corresponds to 68% of the total events.

systematic shift for e-like events. This systematic shift is taken into account when we estimate the systematic uncertainty (see Sec.7.2).

6.5 Momentum determination

The momentum of a particle is calculated with the information of the vertex, direction and particle type. We calculate a total number of corrected photoelectron, R_{tot}, which is related to the momentum. To obtain only direct Cherenkov photons, hit PMTs within a 70° opening angle from the particle direction and within a -50 to +250nsec timing window from the peak of time residual are used. The detected photoelectrons are corrected for by the effective photo-sensitive area of the PMT, $f(\theta)$, the flight length of photons, and light attenuation and scattering in water. The relation between R_{tot} and momentum are determined by the Monte Carlo simulation. Fig. 6.12 shows the relation between the R_{tot}

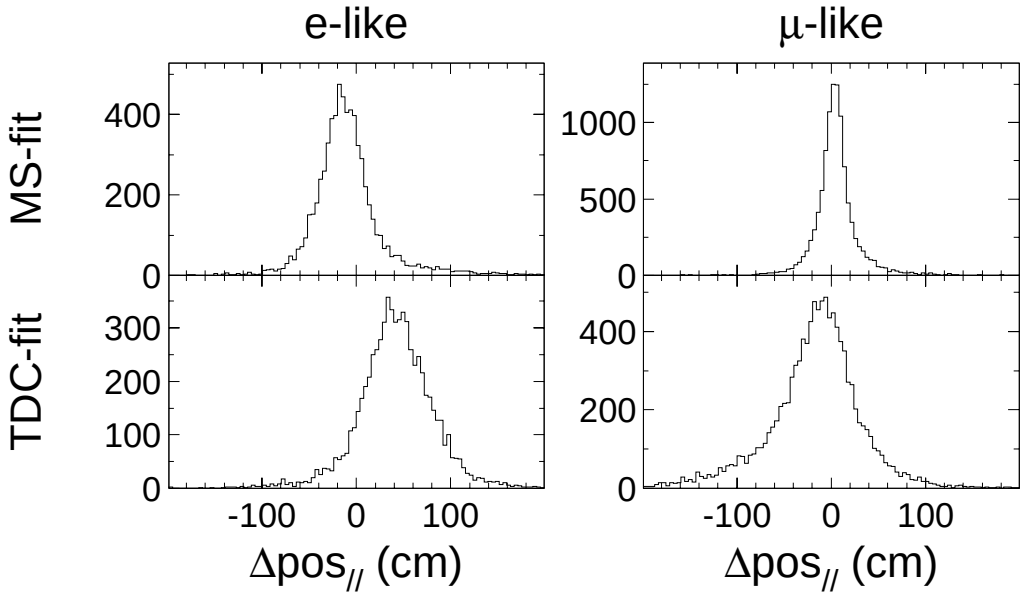

Figure 6.11: The $\Delta pos_{//}$ distribution for e-like(left) and μ-like(right) events, estimated from MC events in the fiducial volume. Upper figures show the result from the MS-fit and lower figures from the TDC-fit.

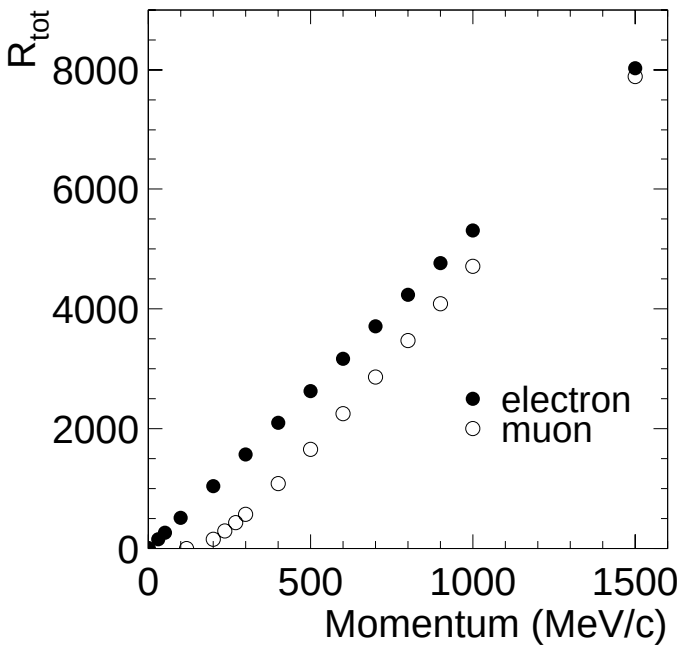

Figure 6.12: Relation between R_{tot} and momentum for the electron and muon, estimated from MC events in the fiducial volume.

and momentum. The momentum for electron and muon is determined from this figure. The systematic uncertainty of the absolute momentum scale is checked by using various sources, such as stopping muons, muon decay electrons, π^0, and so on. It is estimated to be $\pm 2.6\%$. Details of systematic uncertainty estimation are described in appendix A.

Fig. 6.13 shows the momentum resolution of each particle type as a function of momentum. At this time, the momentum resolution is defined as 1σ width of the Gaussian fit. The momentum resolution is estimated to be:
For electrons,

$$0.6 + \frac{2.6}{\sqrt{P_e(GeV/c)}}\%.$$

For muons,

$$1.7 + \frac{0.7}{\sqrt{P_\mu(GeV/c)}}\%,$$

where P_e and P_μ is the momentum of the electron and muon, respectively.

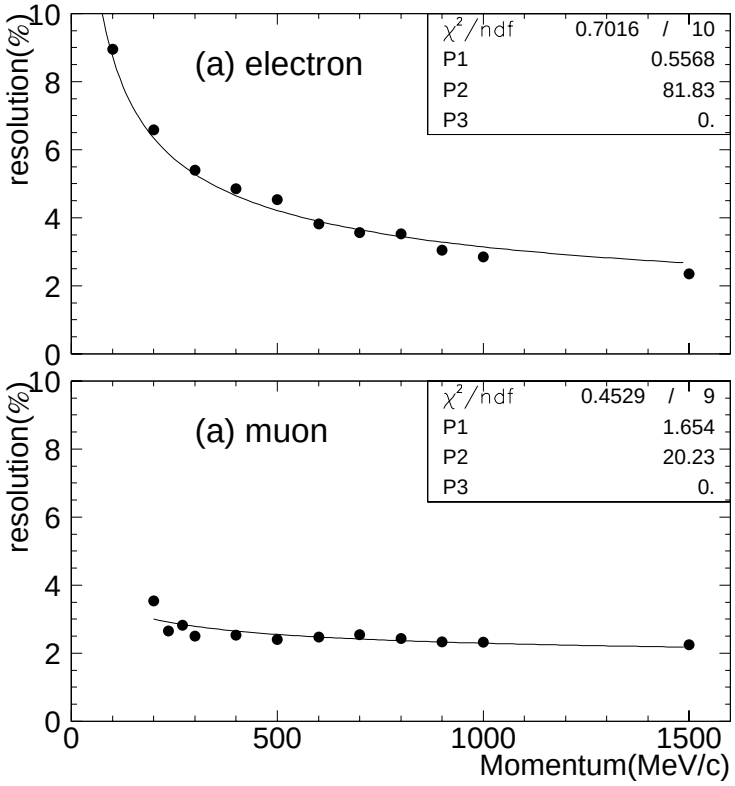

Figure 6.13: The momentum resolution for (a)elections and for (b)muons. The solid lines show the fitted result, estimated from MC events in the fiducial volume.

Chapter 7

Results and discussions

7.1 The atmospheric neutrino flux

In this thesis, we use the atmospheric neutrino data with an exposure of 20 kton-years and Monte Carlo data equivalent to 10 year detector exposure (224.6 kton-years). The number of Monte Carlo events is normalized to the detector exposure for comparison.

To select the sub-GeV event sample, fully-contained events are further subjected to the following sub-GeV criteria:

1. $E_{vis} < 1.33$GeV,
2. $D_{WALL} > 200$cm,
3. 100MeV/c $< P_e$ for an e-like event, and 200MeV/c $< P_\mu$ for a μ-like event,
4. Maximum p.e. in a PMT < 200p.e.,
5. Number of OD-cluster hits ≤ 9,

where D_{WALL} is the distance between the event vertex and the nearest inner detector wall. The second criterion is a fiducial volume cut which removes non-neutrino backgrounds and the third criterion removes low energy backgrounds such as decay electrons from low-energy muons which do not emit Cherenkov light. Fig. 7.1 shows the momentum distribution for e-like and μ-like events with Monte Carlo events. Hatched histograms show the sub-GeV momentum regions. Criteria (4) and (5), shown in Fig. 7.2 and Fig. 7.3, remove remaining partially contained events.

Table 7.1 shows a summary of the sub-GeV atmospheric neutrino sample compared with the Monte Carlo estimation. According to the Monte Carlo simulation, 35% of

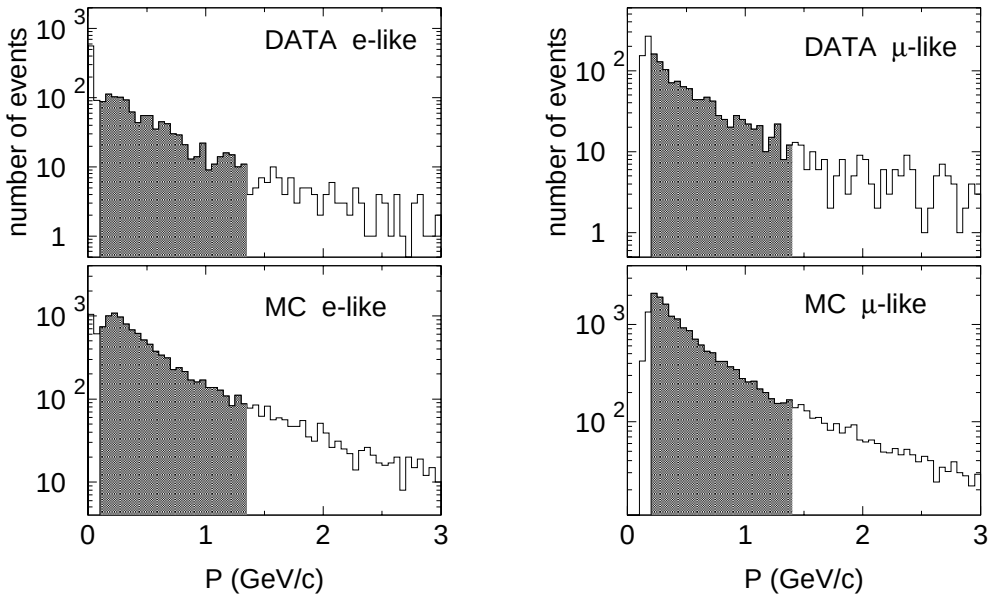

Figure 7.1: Momentum distributions of atmospheric neutrino fully-contained sample. Hatched histograms show the sub-GeV momentum regions.

multi-ring events are produced by neutral current (NC) interactions, which do not remember the flavor of the parent neutrinos. On the other hand, the rate of NC events is only 8% for single-ring events. Therefore we will discuss only the single-ring sample in order to reduce the NC contamination.

The $(\nu_\mu + \bar{\nu}_\mu)/(\nu_e + \bar{\nu}_e)$ ratio, R, is calculated to be:

$$R \equiv \frac{(\mu/e)_{DATA}}{(\mu/e)_{M.C.}} = 0.63 \pm 0.03(stat.) \pm 0.05(sys.).$$

The systematic error will be discussed later. R is significantly lower than 1. This result

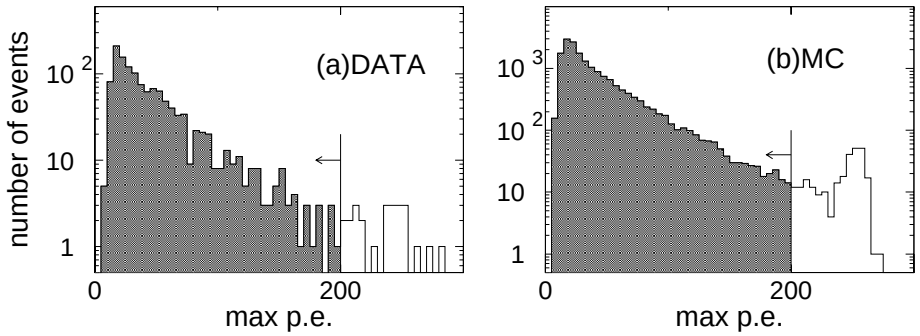

Figure 7.2: Distributions of maximum p.e. in a PMT for (a)DATA and (b)Monte Carlo events after momentum and D_{WALL} cut.

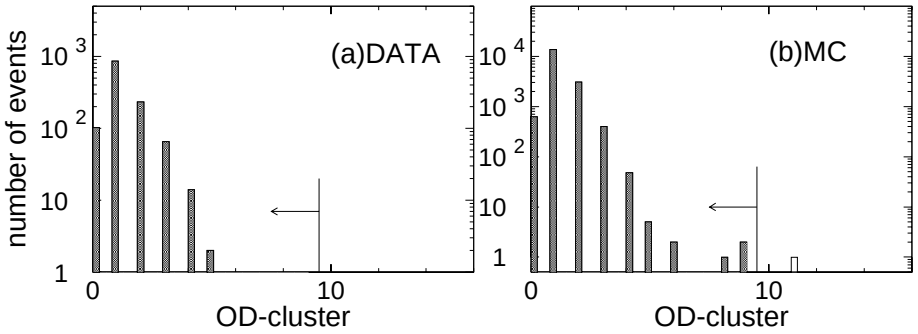

Figure 7.3: Distributions of number of OD-cluster hits for (a)DATA and (b)Monte Carlo events after momentum, D_{WALL} and max. p.e. cut.

is consistent with those of Kamiokande, IMB-3 and Soudan-2 experiments within the estimated error as shown in Fig. 1.2.

Now, we can independently obtain the information on particle type and hence confirm the anomalous μ/e ratio by using the μ-decay signal. The detection efficiency of μ-decay electrons was estimated to be 80$\pm$1.2% for μ^+ and 63$\pm$1.0% for μ^- by the Monte Carlo study. These efficiencies were also confirmed by real cosmic-ray stopping muons to within 1.5%. Table 7.2 shows the number of events which had μ-decay electrons. The fraction of events with μ-decay electrons agrees well with the Monte Carlo estimation. Thus, R calculated from the particle identification algorithm is independently confirmed.

In the next section, I will discuss possible sources of systematic uncertainties and conclude that this small R value is not caused by any detector artifacts.

7.2 Systematic uncertainty

Possible sources which might cause the atmospheric neutrino flux anomaly are summarized in Table 7.3 together with the associated systematic uncertainties.

In the following subsections, each of the possible sources is further discussed. The theoretical uncertainty in the $(\nu_\mu+\bar{\nu}_\mu)/(\nu_\mathrm{e}+\bar{\nu}_e)$ ratio is estimated to be $\sim$5% as already mentioned in Section 4.1.

Primary cosmic-ray flux

As mentioned in Section 4.1, the energy spectrum of primary cosmic-rays is roughly proportional to $E^{-\gamma}$, where γ is fitted to be 2.71$\pm$0.05. The neutrino energy spectrum

	Data	Monte Carlo			
		total	ν_e CC	ν_μ CC	NC
single ring	1453	1551.5	539.7	927.8	84.0
e-like	718	593.8	537.2	8.9	47.7
μ-like	735	957.7	2.5	918.9	36.3
multi ring	533	596.6	148.4	241.3	206.9
total	1986	2148.1	688.1	1169.1	290.9

Table 7.1: Summary of the sub-GeV atmospheric neutrino sample compared with the Monte Carlo estimation. Numbers of the Monte Carlo sample are normalized by livetime of data.

is proportional to $E^{-\gamma} f(E)$ where $f(E)$ takes into account the energy dependence of decay probabilities and meson production cross sections. Therefore, the uncertainty in the power index of the primary cosmic-ray flux is reflected also in the neutrino energy spectrum. In order to estimate the systematics, the spectrum has been changed by a factor of $(E/2\text{GeV})^{\pm 0.05}$ at the neutrino energy E. At this time, the absolute flux at 2GeV, which corresponds to the average atmospheric neutrino energy, is fixed.

Table 7.4 shows the result when the neutrino spectrum is changed. From this table, the effect on R is estimated to be 0.5%.

Particle misidentification

As mentioned in Chap.6, the misidentification probability was estimated to be 0.8±0.1% for the Monte Carlo sample of CC interactions. For CC ν_e (ν_μ)-induced events, the probability that an event be identified as μ-like (e-like) was 0.5±0.1% (1.0±0.1%). Thus, the systematic uncertainty for the μ/e ratio, caused by the particle misidentification, is estimated to be 2%.

Single-ring / multi-ring separation

The number of rings in an event is counted automatically by the ring counting program as described in Sec.6.2. Most of the events can be clearly separated into single- or multi-

	1 or more muon decay		2 or more muon decay	
	data	MC	data	MC
μ-like	$496/735 = 67.5 \pm 1.7\%$	$68.2 \pm 0.1 \pm 1.0\%$	$30/735 = 4.1 \pm 0.7\%$	$4.3 \pm 0.1 \pm 0.2\%$
e-like	$67/718 = 9.3 \pm 1.1\%$	$8.0 \pm 0.3 \pm 0.1\%$	$2/718 = 0.3 \pm 0.2\%$	$0.5 \pm 0.1 \pm 0.01\%$

Table 7.2: Fractions of events with μ-decay in single-ring events. The error of the data and the first error of the MC are statistical. The second error of the MC arises from the detection efficiency of muon decay.

rings. However, low-energy multiple scattering events and high-energy π^o events are difficult to treat reliably.

The systematic uncertainty of single-ring / multi-ring separation was estimated by comparing R between automatic ring counting and visual scanning. The difference between automatic ring counting and visual scanning was found to be 4%, which was taken as a systematic uncertainty.

Vertex position

In order to check a possible bias in the fiducial volume cut, we calculated R based on the TDC-fit, which uses the result of the TDC-fit as a final vertex instead of the MS-fit, and compared with the final R. The numbers of e-like and μ-like events changed as shown in Table 7.5. Since R changed by +0.6%, we estimated the uncertainty caused by vertex reconstruction to be 0.6%.

Energy calibration

The uncertainty caused by the energy determination was estimated by changing the energy scale in the Monte Carlo sample in the following: -2.1% for e-like events, +2.1% and -1.5% for high-energy and low-energy μ-like events, respectively. The details of the energy scale calibration are described in appendix A. Table 7.6 shows the effects. From this result, the systematic uncertainty caused by the energy determination is estimated to be 1.2%.

Source	Error(%)
data reduction	$<<1\%$
$(\nu_\mu+\bar{\nu}_\mu)/(\nu_e+\bar{\nu}_e)$	$<5\%$
$E^{-\gamma}$	0.5%
Particle Identification	2%
single-ring / multi-ring separation	4%
Vertex position	0.6%
Energy calibration	1.3%
Non-neutrino background	
flashing PMT	$<0.5\%$
cosmic-ray muon	$<0.1\%$
e-like background	$<0.1\%$
CC cross section	3.6%
NC cross section	2%
Hadron simulator	0.5%
FC / PC separation	$<0.1\%$
Total	8.1%

Table 7.3: Possible sources of the systematic uncertainties for the sub-GeV μ/e ratio.

Non-neutrino background

We considered three sources as possible non-neutrino backgrounds; flashing PMT events, remaining cosmic-ray muons, and e-like events produced by cosmic-ray neutron interaction in the detector.

For the flashing PMT events, in addition to the flashing PMT cut, we remove them by visual scanning. When we scanned the atmospheric neutrino sample again, the contamination of the flashing PMT events was found to be negligible, thus we estimated the contamination very conservatively to be <0.5%.

We generated 500 cosmic-ray muons by Monte Carlo and one event was reconstructed in the fiducial volume. Since the excess of μ-like events near the detector wall in the atmospheric neutrino sample is at most 40 events, the contamination from cosmic-ray muons is 0.08 ($=40\times\frac{1}{500}$) events. Thus, the muon background is estimated to be <0.1%.

About the neutron background, the contamination of e-like events in the fiducial volume is estimated by fitting the e-like D_{WALL} distribution with the exponential function,

$E^{-\gamma}$	e-like	μ-like	δR
$\gamma = 2.76$	+2.0%	+1.6%	+0.4%
$\gamma = 2.69$	-2.03%	-1.99%	-0.04%

Table 7.4: Effects for the number of e-like and μ-like events and δR when the energy spectrum of the MC atmospheric neutrino is changed.

TDC-fit	data	Monte Carlo
e-like	+2.8%	+3.0%
μ-like	-0.7%	-1.1%
δR		+0.6%

Table 7.5: The effect on the R when we use the result of TDC-fit as a final vertex.

$\exp(-\frac{D_{WALL}}{44cm})$, given by the neutron simulation as shown in Fig. 7.4. The e-like background event was estimated to be only 0.2 events. Since the number of e-like events is 718, the contamination of e-like backgrounds is estimated to be <0.1%.

Monte Carlo simulation

Now, we estimate the systematic uncertainties caused by the neutrino cross sections and nuclear effects. We discuss those in the CC quasi-elastic interaction, CC pion production, and NC interaction separately.

(i) CC quasi-elastic interaction

The axial vector mass, M_A, and the Fermi momentum, P_F, in the Fermi gas model were varied within the allowed ranges. The result is shown in Table 7.7. From this table, we estimated the systematic uncertainty to be 3.6% by assuming that the uncertainty of M_A, P_F, and the nuclear potential are independent.

	Monte Carlo
e-like ($97.9 < P_e$, E_{vis} <1302MeV)	-0.3%
μ-like ($197 < P_\mu$, E_{vis} <1358MeV)	+0.9%
δR	-1.2%

Table 7.6: Effects on the R from the energy-scale uncertainty.

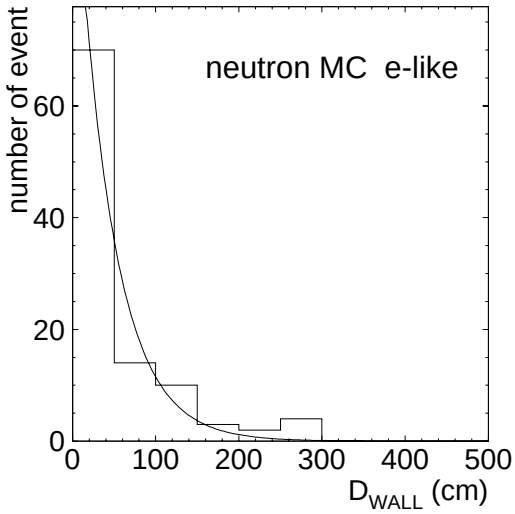

Figure 7.4: The predicted e-like events caused by neutron backgrounds as a function of D_{WALL}. The solid line shows the fitted result by a exponential function.

CC quasi-elastic		e-like	μ-like	δR
M_A :	1.01GeV $\rightarrow$ 1.11	+4.6%	+5.4%	+0.8%
M_A :	1.01GeV $\rightarrow$ 0.91	-4.7%	-5.5%	-0.9%
P_F :	250MeV $\rightarrow$ 180	+12.3%	+8.4%	-3.4%
nuclear potential on	(P_F is 217MeV)	-1.9%	-1.4%	+0.6%

Table 7.7: Effects on R when simulation parameters in the CC quasi-elastic interaction are changed. P_F is the Fermi momentum and M_A is the axial vector mass.

(ii) CC pion production

The uncertainty of the CC pion production cross section is estimated to be $\sim$30%. This comes from the comparison between the calculated value and the experimental data of the pion scattering and experiment uncertainties as shown in Section 4.2. When we change the cross section of the CC pion production interaction by $\pm$30%, R changes as shown in Table 7.8. The systematic uncertainty is estimated to be 0.2%.

CC pion production	e-like	μ-like	δR
change σ by +30%	+6.2%	+6.1%	-0.2%
change σ by -30%	-6.2%	-6.1%	+0.2%

Table 7.8: Effects on R when simulation parameters in the CC pion production interaction are changed.

(iii) NC interaction

The NC cross section was varied by ±50% which is very conservative. The result is given in Table 7.9. The systematic uncertainty is estimated to be 2.2%. In summary, the systematic uncertainties from CC and NC interactions are estimated to be 3.6% and 2.2%, respectively.

NC interaction	e-like	μ-like	δR
change σ by +50%	+4.0%	+1.9%	-2.0%
change σ by -50%	-4.0%	-1.9%	+2.2%

Table 7.9: Effects on the R when simulation parameters in the CC pion production interaction are changed.

We also changed the hadron simulator from CALOR to FLUKA[49] and checked their influence on R. The effect is estimated to be 0.5%.

FC / PC separation

As mentioned before, partially contained(PC) events were removed by the two criteria, (1)maximum p.e. in a PMT $<$ 200 p.e. and (2)number of OD-cluster hit $\leq$ 9. We changed these criteria and checked the effect on R. Table 7.10 shows the effects. The

			δR
maximum p.e.	$\rightarrow$	205 p.e.	-0.02%
maximum p.e.	$\rightarrow$	195 p.e.	+0.02%
OD-hit	$\rightarrow$	11	+0.02%
OD-hit	$\rightarrow$	7	-0.01%

Table 7.10: Effects for the R by changing criteria of maximum p.e. and OD-hit.

criterion of the maximum p.e. is varied by ±2.5% which corresponds to the uncertainty in the absolute energy scale. The number of OD-cluster hits is varied by ±2 which is also conservative. From this table, the uncertainty caused by the FC/PC separation is estimated to be <0.1%.

Adding all of these errors in quadrature, the total systematic error on the μ/e ratio for the sub-GeV data is estimated to be ±8.1%. In the systematic error of R, we also add 1.5% from the statistical uncertainty of the Monte Carlo sample.

7.3 Vertex and momentum distributions

Fig. 7.5 shows the vertex distributions projected to the Z direction for (a)e-like and (b)μ-like single-ring events compared with the Monte Carlo estimation. The excess at the top detector wall for μ-like events is due to cosmic-ray muons which entered cable-holes without firing the outer detector as mentioned in Sec. 5.5. If the shapes are assumed to be flat with the absolute normalization being free, $\chi^2/d.o.f.$ is 24.6/31 for e-like events and 44.5/31 ($\sim$5%) for μ-like events in the fiducial volume. R as a function of Z is shown in Fig. 7.6. The $\chi^2/d.o.f.$ of this distribution is calculated to be 32.0/31. Thus, the deviation from the flat distribution is not significant. Fig. 7.7 shows the vertex distributions projected to the X^2+Y^2 direction for (a)e-like and (b)μ-like events. The $\chi^2/d.o.f.$ assuming a flat distribution, are 14.6/27 and 29.43/27 for e-like and μ-like events, respectively. Shapes are consistent with the flat distribution both for e-like and μ-like events. Fig. 7.8 shows R $(=(\mu/e)_{DATA}/(\mu/e)_{MC})$ as a function of D_{WALL}. The distribution is consistent with a constant R ratio in the fiducial volume. The larger value of R near the detector wall is again due to cosmic-ray muons that went through the cable holes.

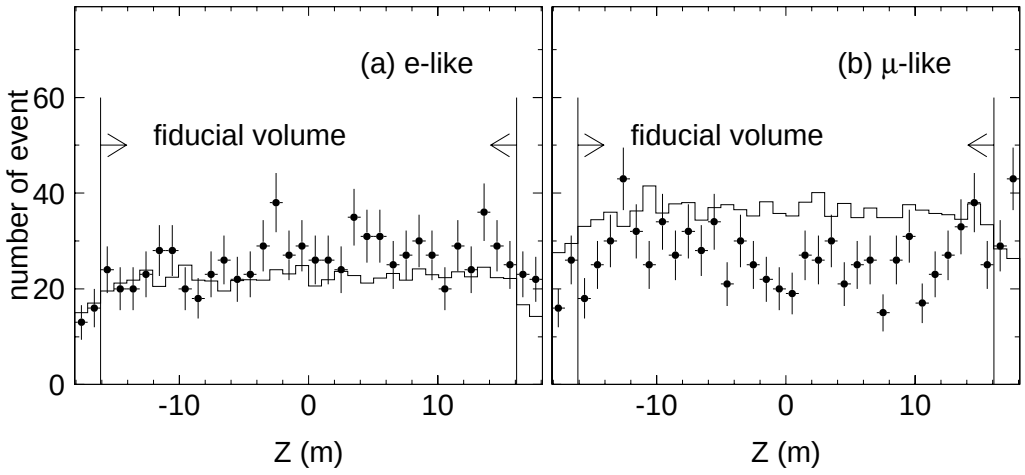

Figure 7.5: The sub-GeV single-ring vertex distributions projected to the Z direction (+18.1m and -18.1m show the top and bottom PMT surface, respectively). Error bars show the statistical error for the real data. Histograms show the Monte Carlo prediction. The high rate at the highest Z bin is due to cosmic-ray muons that went through the cable holes and hence did not give signals in the outer detector.

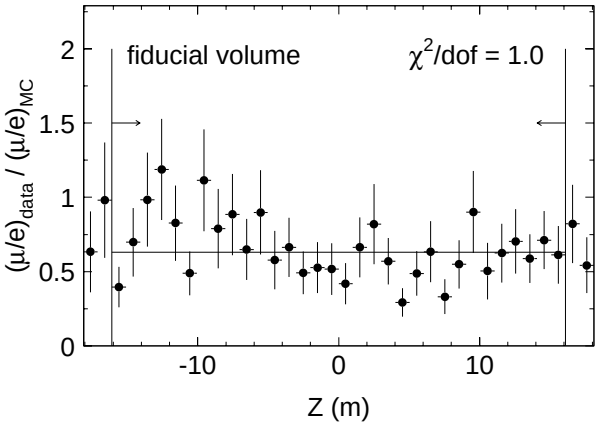

Figure 7.6: The $(\mu/e)_{DATA}/(\mu/e)_{M.C.}$ vs Z plot. Error bars include both the real and Monte Carlo statistical errors. Solid line and χ^2 are the fitted results assuming a flat line and free absolute normalization.

The momentum distributions are shown in Fig. 7.9 for (a)e-like and (b)μ-like events. It seems that there is a deficit for μ-like events and there is an excess for e-like events, but we cannot state a definite answer because the absolute normalization has a 20% uncertainty from the neutrino flux calculation and 15% from the neutrino interaction cross section, resulting in a total of 25%.

Fig. 7.10 shows R as a function of the momentum. It is consistent with a flat distribution within the statistical error ($\chi^2/d.o.f. = 1.1/4$) in this momentum range.

As mentioned in Section 1.3.2, the proton decay, $p \to e^+\nu\nu$, predicts an excess of e-like events, in the momentum range less than 500MeV/c. The data do not support the proton decay hypothesis to explain the small ν_μ/ν_e ratio.

7.4 The Zenith angle distribution

If the atmospheric neutrino anomaly is indeed caused by neutrino oscillations, an up-down asymmetry in the zenith angle distribution is expected. The higher the observed momenta, the better the direction of an observed event follows the original neutrino direction. Fig. 7.11 shows the Monte Carlo simulation of the angular correlation between reconstructed and parent-neutrino directions. Events with visible energies less than a few hundred MeV lose directionality, but above 500MeV, the correlation becomes better than 40^o for both e-like and μ-like events. Therefore even the sub-GeV sample has some directional sensitivity.

Fig. 7.12 shows the zenith angle ($\cos\Theta$) distributions for (a)e-like and (b)μ-like events together with the Monte Carlo predictions, where $\cos\Theta = 1$ means down-going. To check a possible momentum dependence, the $\cos\Theta$ distributions are further divided

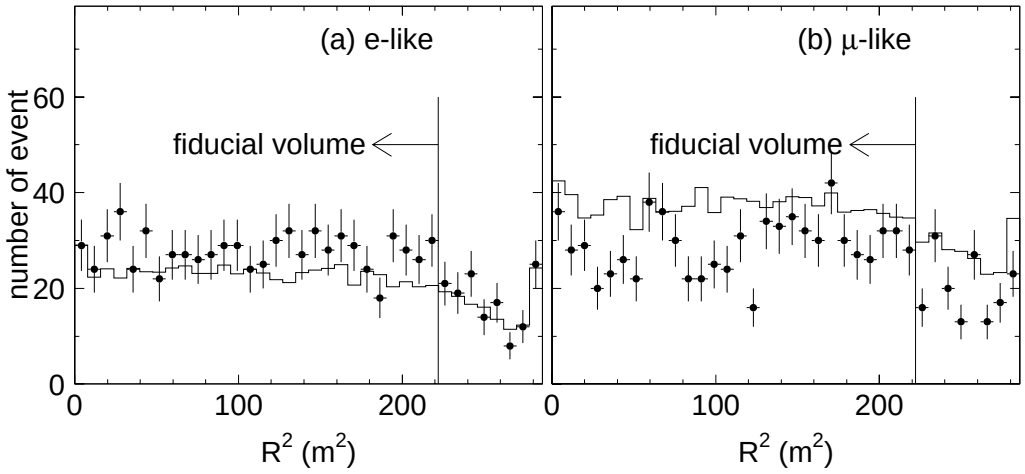

Figure 7.7: The sub-GeV single-ring vertex distribution projected to the X and Y plane. $R^2 = 0$ means the center of the detector. Error bars show the statistical error for the real data. Histograms show the Monte Carlo prediction.

into two momentum regions as shown in Fig. 7.13. For μ-like events with momenta above 400MeV/c, the data exhibit a small up-down asymmetry. But for μ-like events below 400MeV/c, the shape is consistent with flat. This is what one expects at low energies. On the other hand, for e-like events at high energies, the shape is consistent with a flat distribution. We will estimate the systematic up-down uncertainty in the μ/e ratio in the next subsection.

R as a function of $\cos\Theta$ is shown in Fig. 7.14. The χ^2 assuming a flat R is :χ^2/d.o.f. = 18.0/4. The up-down asymmetry is enhanced by an excess in the left most bin (-1 $< \cos\Theta <$ 0.6) in the lower e-like $\cos\Theta$ distribution as seen in Fig. 7.13(a). We believe the non flat e-like distribution was caused by a statistical fluctuation, since this effect is mostly coming from the momentum region of less than 400MeV/c where we expect no strong directionality. Again, the $\cos\Theta$ distributions are divided into two momentum regions as shown in Fig. 7.15. The up-down asymmetry of R is seen only in the high momentum region.

Systematic uncertainty of up-down asymmetry

We have already shown the zenith angle distributions in Figs. 7.12-7.14. In this subsection, we will estimate the systematic uncertainty for the zenith angle distributions.

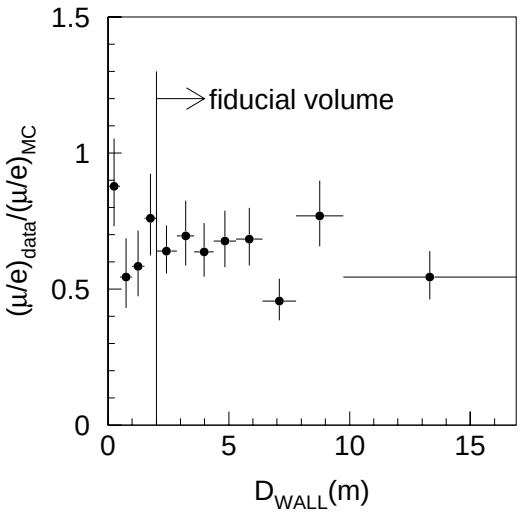

Figure 7.8: The $(\mu/e)_{DATA}/(\mu/e)_{M.C.}$ vs D_{WALL} plot. $D_{WALL} = 0$ means the PMT surface. Error bars include both the real and Monte Carlo statistical errors.

Since the mean neutrino energy for the present sample is about 0.8GeV, and the geomagnetic field causes about 30% up-down asymmetry at this energy range, this effect could induce some systematic up-down asymmetry in the μ/e ratio. In order to estimate this uncertainty, we used two independently calculated fluxes[1][50] and compared the $(\mu/e)_{MC}$ ratio using these two calculations, from which we conclude that the possible up-down systematic asymmetry is less than $\pm 1\%$. The other source which could produce up-down asymmetry is a possible gain asymmetry of the PMTs. We used μ-decay electrons to estimate the up-down gain asymmetry. To avoid the muon polarization effect for the electron energy spectrum, we selected electrons which direction of with almost right angles to the directions of the parent muons. Fig. 7.16 shows the average of the corrected total number of p.e., R_{tot}, for decay electrons as a function of the zenith angle ($\cos\Theta$). Note that the R_{tot} is proportional to the electron momentum as shown in Fig. 6.12. By this figure, we estimate that the detector gain is uniform within $\pm 1.5\%$ between down-going and up-going particles which may be due to the relative gain variation. This gain asymmetry could cause only $\pm 0.4\%$ up-down asymmetry in R, because it largely cancels when we take the μ/e ratio. The contamination of non-neutrino background, less than 0.5%, could have directional correlation and could add a maximum of $\pm 1\%$ to the up-down systematic error. Adding these three in quadrature, the possible systematic error in the up-down asymmetry of R is 1.5%. This systematic error is negligibly small compared with the statistical errors in Fig. 7.12.

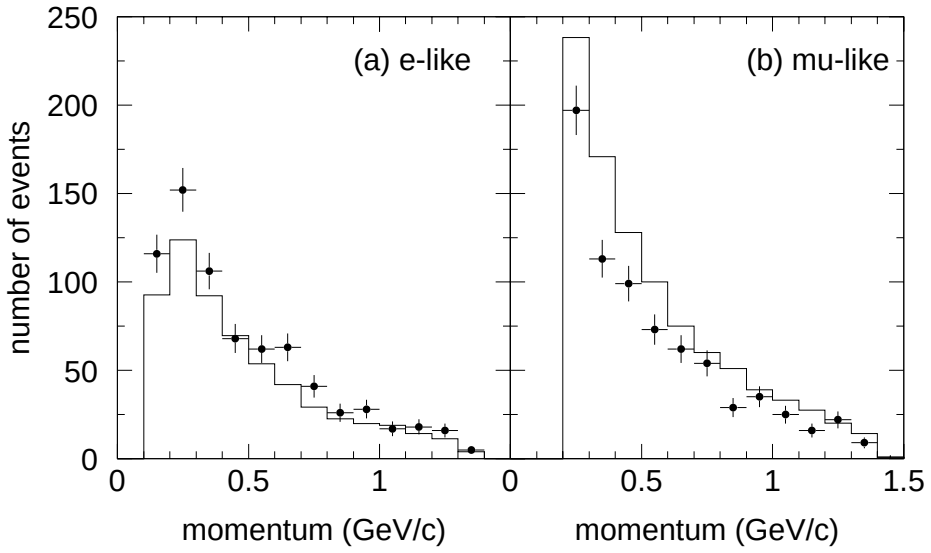

Figure 7.9: Momentum distribution for (a)e-like and (b)μ-like events. Error bars are the statistical errors of the real data. Histograms show the Monte Carlo prediction.

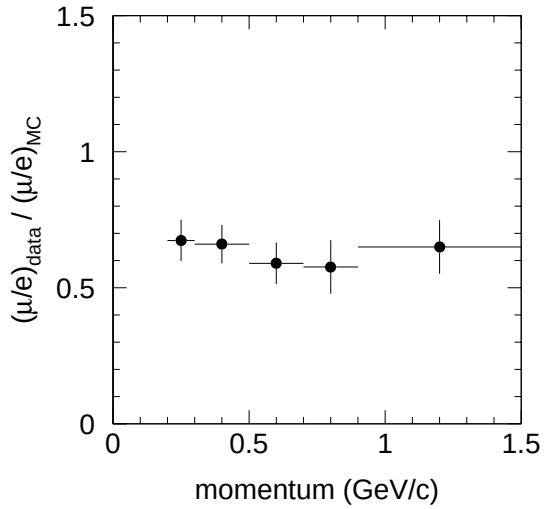

Figure 7.10: The R $(=(\mu/e)_{DATA}/(\mu/e)_{M.C.})$ vs momentum. Error bars include the statistical errors for the data and Monte Carlo.

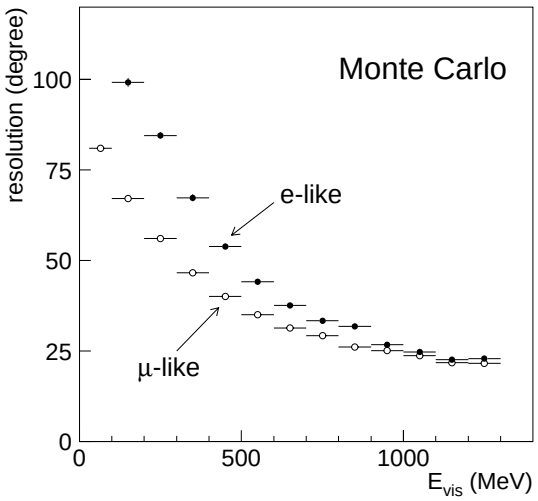

Figure 7.11: The average angle between reconstructed and parent-neutrino directions as a function of visible energy of the detected particles, estimated by the Monte Carlo simulation. Filled and open circles show the resolutions for e-like and μ-like events, respectively.

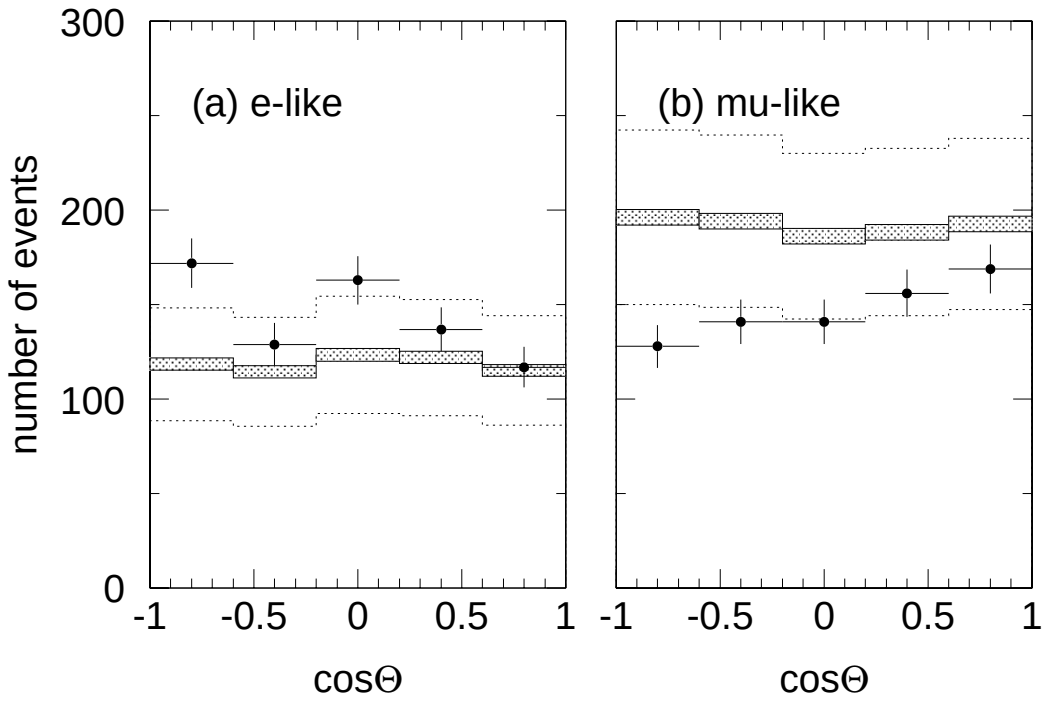

Figure 7.12: The zenith angle distribution for (a)e-like and (b)μ-like events. The errors are statistical only. The systematic errors are negligible compared to the statistical ones. (See the text for details) Hatched histograms show the Monte Carlo prediction and the width of these regions represents the statistical uncertainties. Dotted histograms show the systematic uncertainty on the absolute normalization of the Monte Carlo events.

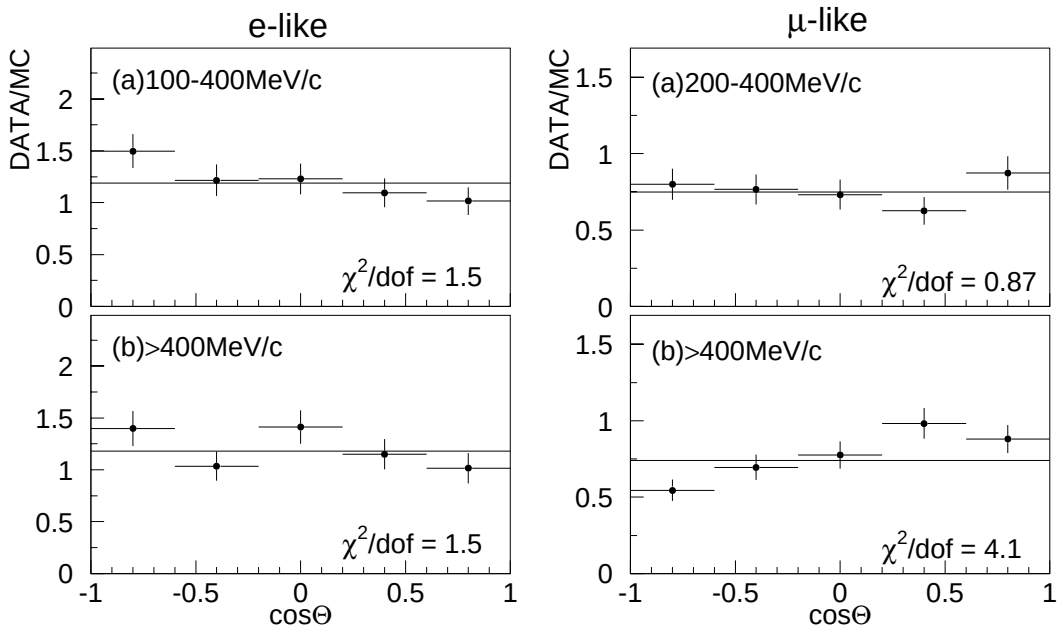

Figure 7.13: The ($\cos\Theta$) distribution for e-like and μ-like events divided into two momentum regions, (a)200-400MeV/c and (b)>400MeV/c. Solid lines and χ^2s are the fitted results assuming a flat line and free absolute normalization.

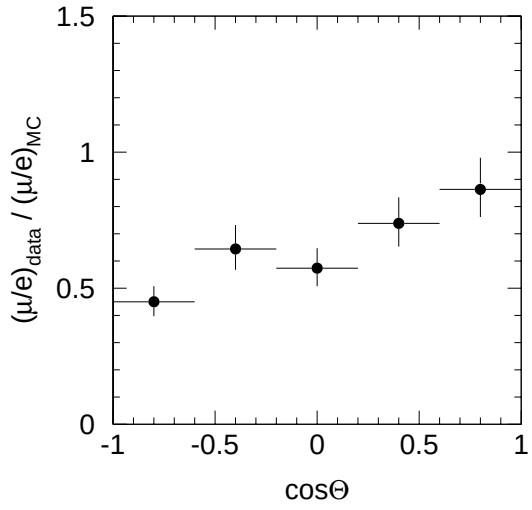

Figure 7.14: The R ($=(\mu/e)_{DATA}/(\mu/e)_{M.C.}$) as a function of $\cos\Theta$. Error bars are statistical only.

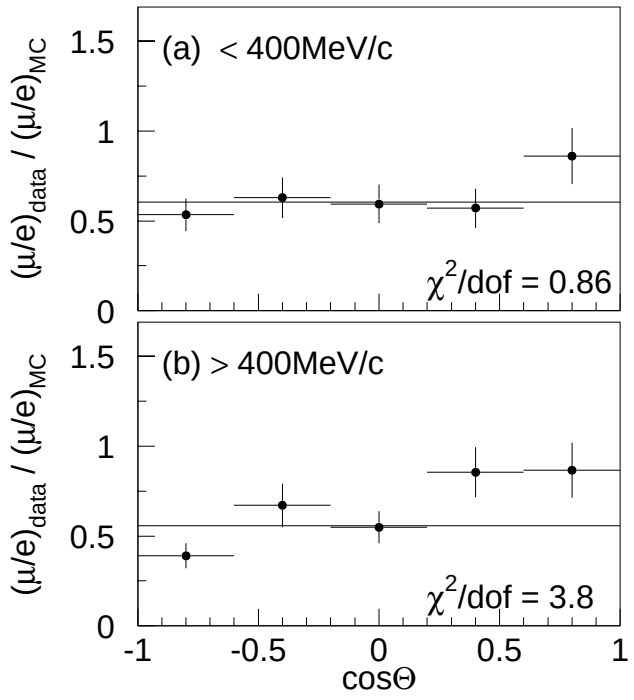

Figure 7.15: The R $(=(\mu/e)_{DATA}/(\mu/e)_{M.C.})$ as a function of $\cos\Theta$ divided into two momentum regions, (a)<400MeV/c and (b)>400MeV/c. Error bars are statistical only.

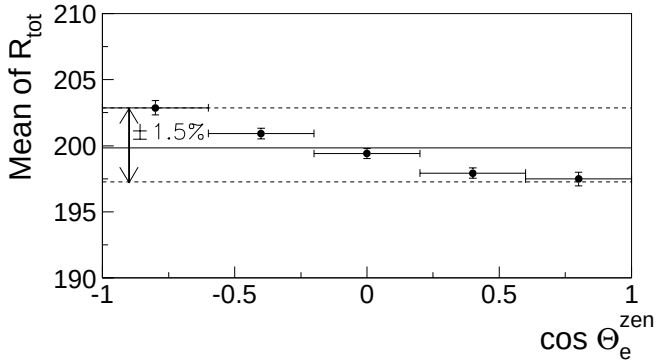

Figure 7.16: The mean of the R_{tot} for μ-decay electrons as a function of the zenith angle ($\cos\Theta$.)

Chapter 8

Conclusion

The atmospheric neutrino flux has been measured using 20.0 kton-years exposure of the Super-Kamiokande detector. 735 single-ring μ-like and 718 e-like events were detected with momentum $p_e > 100$ MeV/c, $p_\mu > 200$ MeV/c and with visible energy less than 1.33 GeV in the fiducial volume (22.5kton). Using the Monte Carlo prediction, based on the calculations of the atmospheric neutrino fluxes provided by Honda et al[1], the double ratio R $(=(\mu/e)_{DATA}/(\mu/e)_{M.C.})$ is;

$$R = 0.63 \pm 0.03(stat.) \pm 0.05(sys.).$$

R is significantly lower than unity and this result confirms the previous results from Kamiokande, IMB-3, and Soudan-2 experiments. No evidence for the momentum and vertex position dependence of R was observed.

We find that R depends on the zenith angle. The up-down asymmetry in the zenith angle distribution may shed light on a possible source of the small value of R.

Appendix A

Absolute energy scale and the stability of the detector

In this chapter the ambiguity of the absolute energy scale is estimated using five calibration sources. Since the systematic uncertainty in the absolute energy scale affects the atmospheric neutrino flux measurement directly, we must understand how precise the Monte Carlo simulation reproduces the absolute energy scale.

Decay electrons

We have a large number of low energy electrons produced by the decay of cosmic-ray muons. The absolute energy scale is checked by comparing the the Michél electron spectrum between the data and the Monte Carlo. Decay electrons are selected with the following criteria:

1. electrons are detected from 1.5μsec to 8μsec after the trigger of a parent muon.
2. number of ID-hits is less than 1000.
3. $goodness_{low}$ is more than 0.5.
4. the vertex position is reconstructed in the fiducial volume.

MC events are generated uniformly in the fiducial volume and randomly for the direction. Fig. A.1 shows the momentum spectrum for electrons in fiducial volume compared with MC events. The spectrum of MC takes into account an effect of the nucleon Coulomb field caused by atomic capture of a parent muon[51]. The spectrum of the data agrees well with the MC. The mean value of the MC is 2.0% lower than that of the data.

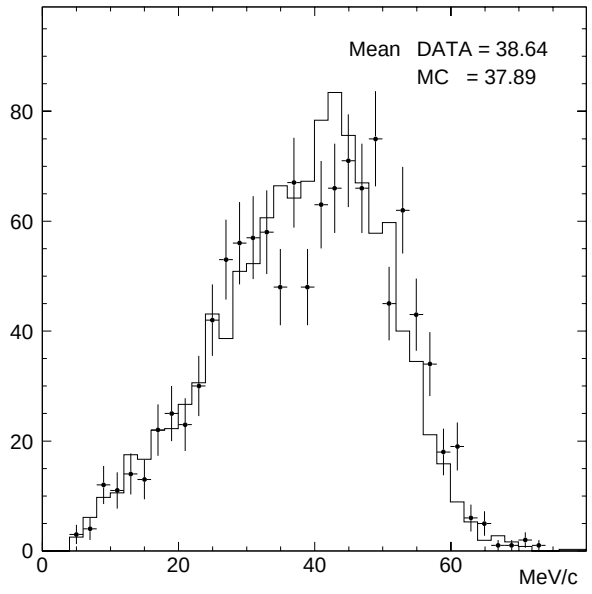

Figure A.1: Momentum spectrum of muon decay electrons in the fiducial volume. Points with error bars show the data and histogram shows the MC.

LINAC

In Super-Kamiokande, an electron linear accelerator(LINAC) is used to understand precisely the performance of the detector for low energy event[52]. The energy of electrons can be adjusted from 5 to 16MeV and energy spread at the end of beam pipe is less than 0.3%. We use electrons with the energy of 16MeV. The injected position is 6m from the top PMT surface and the direction is downward. LINAC electron events are selected according to the following criteria:

1. number of ID-hits is between 100 and 210.
2. $goodness_{low}$ is more than 0.5.
3. the distance between the injected position and the reconstructed position is less than 2m.

Fig. A.2 shows the momentum distribution for LINAC electrons compared with MC events. The agreement of the momentum distributions between the data and the MC is satisfactory. The mean value of the MC is 2.4% higher than that of the data.

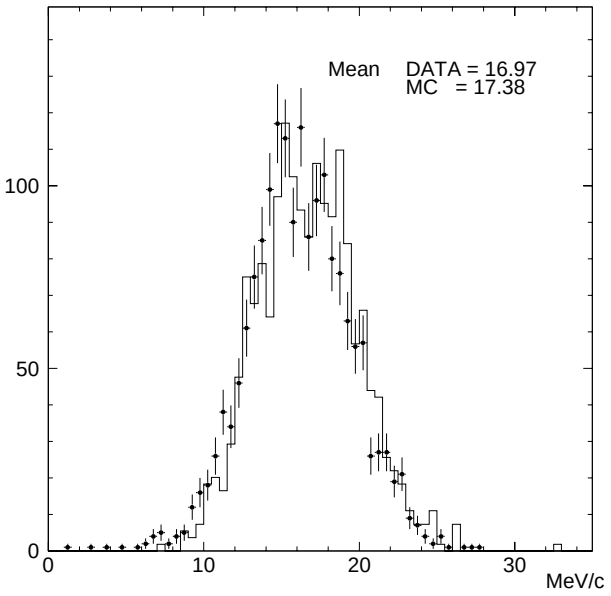

Figure A.2: Momentum spectrum of LINAC electrons. Points with error bars show the data and histogram shows the MC.

π^0 mass

Single π^0 events are produced by the atmospheric neutrino interaction. If the momentum of a π^0 is less than about 400MeV/c, in many cases, we can detect two clear Cherenkov rings produced by two γ's from the π^0 decay. The π^0 mass, m_{π^0}, is given by the next equation:

$$m_{\pi^0}^2 = 2P_{\gamma 1} \cdot P_{\gamma 2}(1 - \cos\theta),$$

where $P_{\gamma 1}$ and $P_{\gamma 2}$ are the momentum of two gamma-rays and θ is the opening angle between two gamma-rays. The single π^0 events are selected from the atmospheric neutrino fully-contained event sample with the following criteria:

1. total momentum of a event is less than 400MeV/c.

2. 2-rings and both of them are identified as e-like.

3. vertex is reconstructed in the fiducial volume.

Fig. A.3 shows m_{π^0} distribution for the data and the MC events, which are fitted by the Gaussian distribution. The agreement of fitted shapes between the data and the MC is satisfactory. The fitted peak of the MC distribution is 2.5% lower than that of the data.

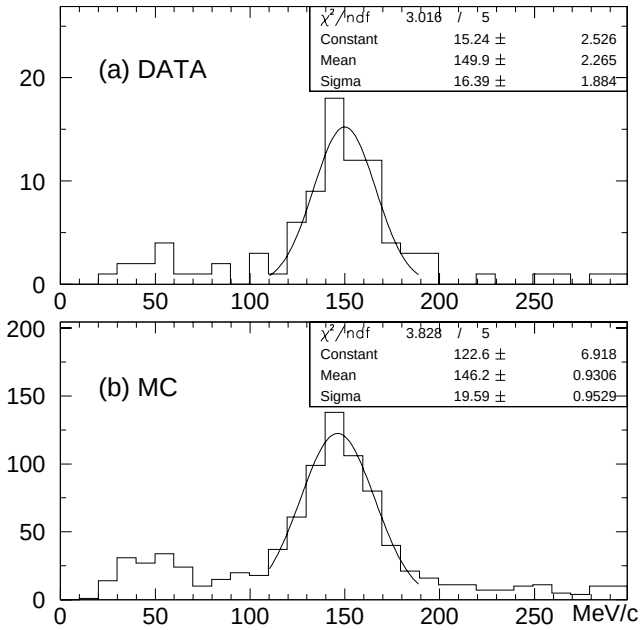

Figure A.3: The distribution of the reconstructed invariant mass for the data and the MC. The solid line shows the result of a Gaussian fit.

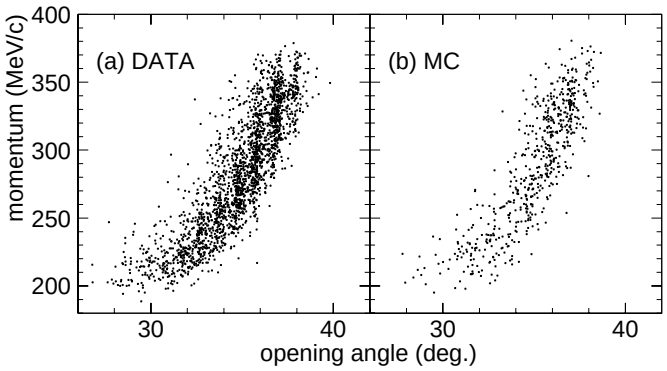

Figure A.4: Opening angle vs momentum plots for (a)data and (b)MC stopping muon events.

Low energy Stopping muons

Using the opening angle of the Cherenkov ring for low-energy muons, we can estimate the momentum independently to check the systematic uncertainty of the momentum reconstruction. The relation between the momentum and the opening angle is given in Eq.2.2. We used stopping muons which enter from the top wall and have one decay electron events. Fig. A.4 shows the reconstructed momentum as a function of the opening angle for the low energy stopping muon events. We calculated a ratio, $R_{data\,\mathrm{or}\,MC}$, which is defined as (momentum) / (momentum estimated by the opening angle). To estimate the momentum dependence, data sets are divided into 5 momentum bins. Fig. A.5 shows the $\langle R_{MC}\rangle/\langle R_{data}\rangle$ plots as a function of momentum. ($\langle R\rangle$ means the average of R.) This figure represents the systematic uncertainty of the momentum determination between the data and the Monte Carlo. The deviation from 1 is less than $\pm 2.5\%$.

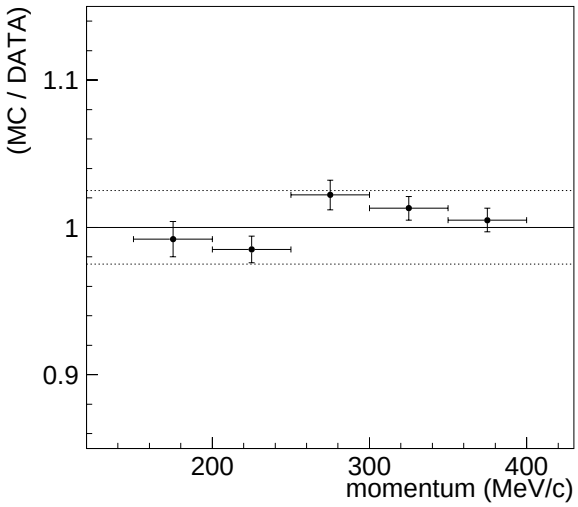

Figure A.5: The $\langle R_{MC} \rangle / \langle R_{data} \rangle$ plots as a function of momentum. Dotted lines show $\pm 2.5\%$.

High energy Stopping muons

In the high energy region, the range of stopping muons is used to check the absolute energy scale. Because a range of stopping muons is proportional to the momentum and it is easy to calculate the end point of the muon by finding the vertex position of the muon-decay electron. The range is defined as the distance from the vertex position of the stopping muon to the vertex position of its decay electron. Fig. A.6 shows the ratio of momentum and range, (mom./range) distribution as a function of range. The energy deposit per 1cm is about 2.5MeV. Since the ambiguity of the vertex determination affects the range when the range is short, events with a range larger than 7m are used. Events are divided into 6 bins by the range. The average of (mom./range) for the data and the MC is calculated and the ratio is taken. The ratio, $\langle \text{mom./range} \rangle_{data}$ and $\langle \text{mom./range} \rangle_{MC}$ are shown in Fig. A.7. The MC is higher than the data at most 2.6%. In the sub-GeV range the systematic difference between the data and the MC is 2.1%.

Summary of the absolute energy scale

Fig. A.8 shows the summary of the studies for the absolute energy scale. Events with the momentum from 16MeV to about 10GeV are examined and the energy scale for Monte Carlo events agree with that for the data within +2.6% and -2.5%.

Stability of the detector

We have been checking the stability of the absolute energy scale using high-energy stopping muons. Fig. A.9 shows the $\langle \text{mom./range} \rangle_{data}$ plots as a function of time. In

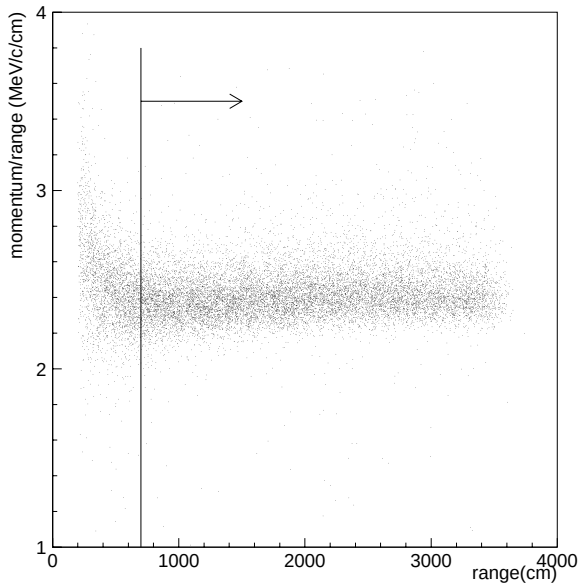

Figure A.6: The mom./range vs range plot for stopping muon events. Events with a range more than 7m are used for the analysis.

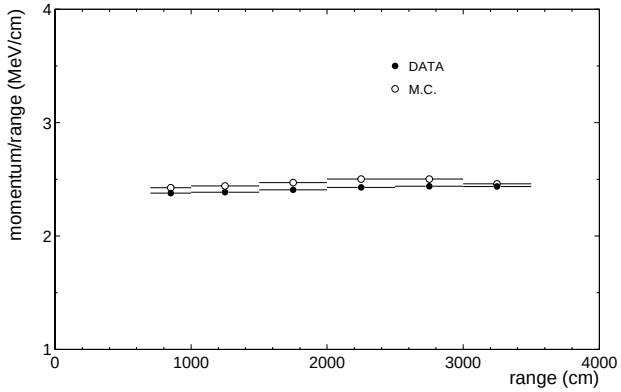

Figure A.7: $\langle \text{mom./range} \rangle_{data}$ and $\langle \text{mom./range} \rangle_{MC}$ plots as a function of range.

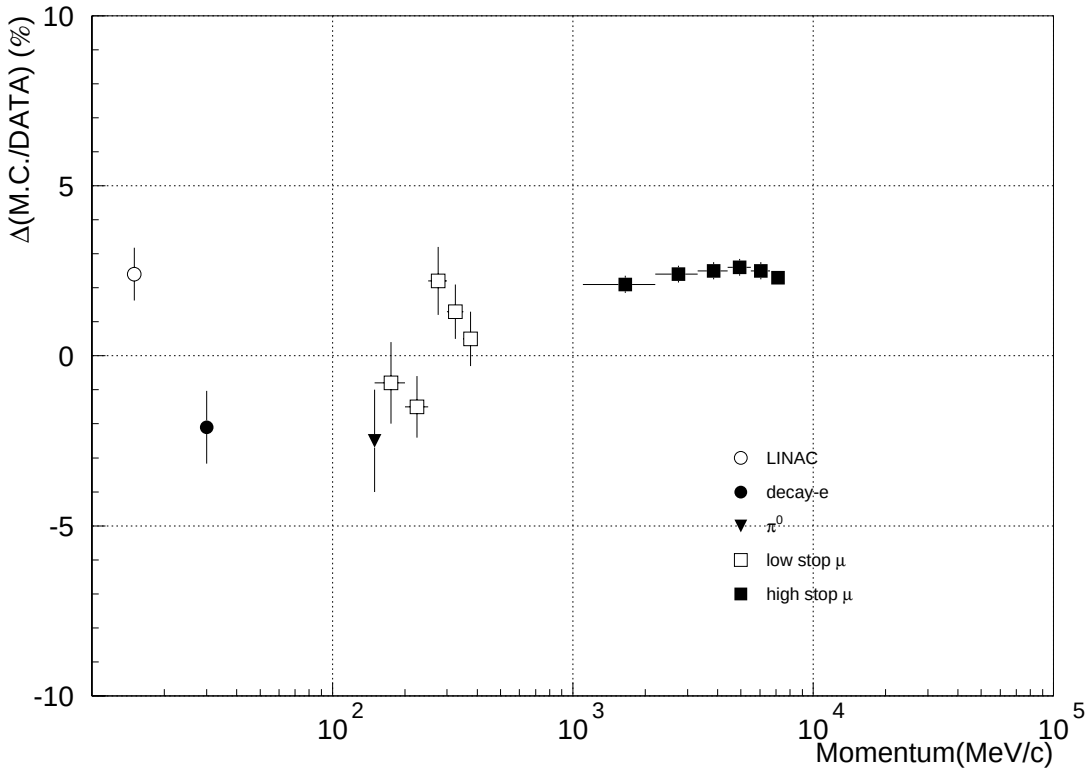

Figure A.8: Summary of the absolute energy scale.

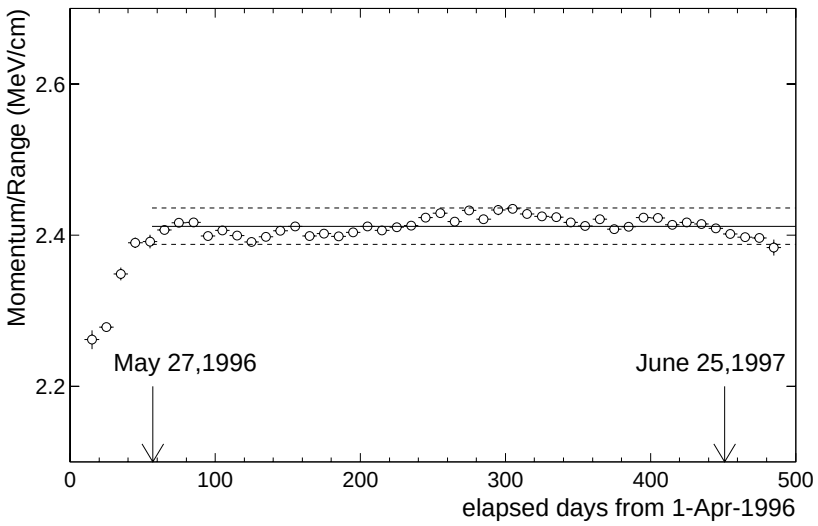

Figure A.9: The time variation of the ⟨mom./range⟩. The x-axis show the day from Apr. 1,1996. Dotted lines show the ±1% from the solid line.

calculating the momentum, the attenuation length of the water is corrected. But the energy scale still correlates with the water attenuation length(see Fig. 3.12). However the effect of the water transparency to the momentum is reduced within 1% after end of May 1996.

We also uses muon-decay electrons to check the detector stability. Fig. A.10 shows the time variation of the mean electron energy. The reconstructed energies of electrons are stable within 1% after end of May 1996.

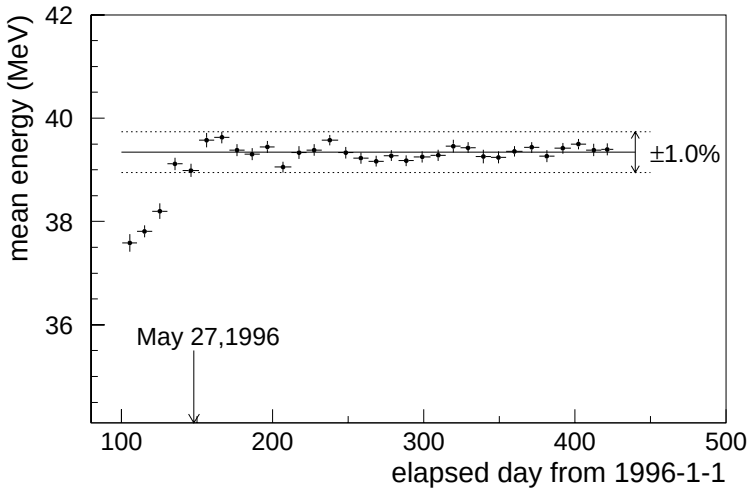

Figure A.10: The time variation of the mean energy of the muon-decay electrons. Dotted lines show the $\pm 1\%$ from the solid line.

Bibliography

[1] M. Honda *et al.*, Phys. Rev.**D52**(1995)4985;
M. Honda *et al.*, Phys. Lett.**B248**(1990)193.

[2] K.S. Hirata *et al.*, Phys.Rev.Lett.,65(1990)1297.

[3] K.S. Hirata *et al.*, Phys.Rev.Lett.**58**(1987)1490;
K.S. Hirata *et al.*, Phys.Rev.**D38**(1988)448.

[4] S.Kasuga *et al.*, Phys. Lett.**B374**(1996)238.

[5] R. Becker-Szendy *et al.*, Phys. Rev.**D46**(1992)3720;
D. Casper *et al.*, Phys. Rev. Lett.**66**(1991)2561.

[6] W.W.M Allison *et al.*. Phys. Lett.**B391**(1997)491.

[7] Ch.Berger *et al.*, Phys.Lett.**B245**(1990)305.

[8] M.Aglietta *et al.*, Europhys.Lett.**8**(1989)611.

[9] Y.Fukuda *et al.*, Phys.Lett.**B388**(1996)397.

[10] N.Hata and P.Langacker, hep-ph/9705339, May.1997.

[11] K.Gabathuler *et al.*, Phys.Lett.**B138**(1984)449.

[12] B.Achkar *et al.*, Nucl. Phys.**B434**(1995)503.

[13] M.Apollonio *et al.*, hep-ex/9711992 Nov.1997.

[14] F.Dydak *et al.*, Phys.Lett.**B134**(1984)281.

[15] R.Becker-Szendy, *et al.*, Phys.Rev.Lett.**69**(1992)1010.

[16] A.Suzuki *et al.*, Nucl.Instr.Meth.Phys.Res.**A329**(1993)299.

[17] T. Tanimori *et al.*, IEEE Trans. Nucl. Sci.**36**(1989) 497.

[18] G.Barr, T.K.Gaisser, and T.Stanev, Phys. Rev.**D 39**(1989)3532.

[19] E.V.Bugaev and V.A.Naumov, Phys. Lett.**B232**(1989)391.

[20] H.Lee and Y.Koh, Nuovo Cimento**B105**(1990)884.

[21] M.Nakahata *et al.*, J. Phys. Soc. Jpn.**55**(1986)3786.

[22] K.L.Miller *et al.*, Phys. Rev.**D26**(1982)537.

[23] S.Hiramatsu *et al.*, Proceefings of the Int.Conf. on Nuclear Structure Studies Using Electron Scattering and Photoreaction, Sendai, 1972, P.429.

[24] S.J.Barish *et al.*, Phys. Rev.**D16**(1977)3103.

[25] S.Bonetti *et al.*, Nuovo Cimento**A38**(1977)260.

[26] S.V.Belikov *et al.*, Z.Phys.**A320** 625.

[27] N.Armenise *et al.*, Nucl. Phys.**B152**(1979)365.

[28] K.Abe *et al.*, Phys. Rev. Lett.**56**(1986)1107.

[29] C.H.Albright *et al.*, Phys.Rev.**D14**(1976)1780.

[30] D.Rein and L.M.Sehgal, Ann. of Phys.**133**(1981)79;
D.Rein, Z.Phys.**C35**(1987)43.

[31] S.J.Barigh *et al.*, Phys. Rev.**D17**(1978)1.

[32] H.Sarikko, Neutrino '79(1979)507.

[33] Paul Musset and Jean-Pierre Vialle, Phys. Rep.**C39**(1978)1.

[34] J.E.KIM et al., Rev.Mod.Phys. 53(1981)211.

[35] D.REIN and L.M.Sehgal, Nucl. Phys.**B223**(1983)29.

[36] L.L.Salcedo *et al.*, Nucl. Phys.**A484**(1988)557.

[37] G.Rowe *et al.*, Phys. Rev.**C18**(1978)584.

[38] D.Ashery *et al.*, Phys. Rev.**C23**(1981)2173.

[39] C.H.Q.Ingram *et al.*, Phys. Rev.**C27**(1983)1578.

[40] "GEANT Detector Description and Simulation Tool", CERN Program Library W5013(1994).

[41] T. A. Gabriel *et al.*, IEEE Trans. Nucl. Sci 36,1(1989)14.

[42] K.Fujita M.Thesis, Tohoku Univ.(1995).

[43] A.S.Carrol *et al.*, Phys. Rev.**C14**(1976)635.

[44] E.Bracci *et al.*, CERN/HERA 72-1(1972).

[45] E.Eichler, JADE-Note 65(1980).

[46] T.Fujii *et al.*, Nucl. Phys.**B120**(1977)395.

[47] K.Baba *et al.*, Nucl. Phys.**A306**(1978)292.

[48] Kanaya M.Thesis, Tokyo Institute of Technology(1998).

[49] P.A.Aarnio et al. Fluka user's guide. Technical Report TIS-RP-190,CERN,1987,1990 A.Fassò A.Ferrari J.Ranft P.R.Sala G.R.Stevenson and J.M.Zazula. FLUKA92. In Proceedings of the Workshop on Simulating Accelerator Radiation Environments, Santa Fe, USA, 11-15 January 1993.

[50] G. Barr *et al.*, Phys. Rev.**D39**(1989) 3532;
V. Agrawal *et al.*, Phys. Rev.**D53**(1996) 1314,
and T.K.Gaisser, private communication(1996).

[51] P.Hänggi, R.D.Viollier, U.Raff and K.Alder, Phys. Lett. **51B**(1974)119.

[52] Y.Koshio, Ph.D.Thesis, Univ. of Tokyo(1998).